UNIVERSITY OF LIVERPOOL

Study of Two Perovskite Materials as Potential Candidates for Intermediate Temperature Solid Oxide Fuel Cells (IT-SOFCs)

Thesis submitted in accordance with the requirements of the University of Liverpool for the degree of Master of Philosophy

Wen XU

Jan 2016

Supervised by

Professor M. J. Rosseinsky

Dr J. B. Claridge

Abstract

The work presented in this thesis focuses on the effect on structure and properties of the cubic perovskite system, $Ba_{0.5}Sr_{0.5}Co_{0.8}Fe_{0.2}O_{3-\delta}$ (BSCF), when $Ba_3CoNb_2O_9$ (BCN) and La_2CoTiO_6 (LCT) were added into the system. BSCF is a candidate cathode material for intermediate temperature (500-750°C) solid oxide fuel cells (IT-SOFCs), showing promising electrochemical activity for the oxygen reduction reaction (ORR). Doping of the parent material BSCF with BCN and LCT targeted the retention of the cathodic performance whilst improving the reported structural thermal instability and incompatibility issues with commonly used electrolytes.

A range of BCN-BSCF and LCT-BSCF compositions were synthesised and characterisation was carried out by a combination of diffraction techniques. It was found that the introduction of small amount (5%) of BCN and LCT favoured the formation of solid solution that is isostructural to the parent material BSCF. Materials with medium doping level (10% and 50%) of BCN and LCT afford two cubic perovskites structure.

A series of tests were carried out to investigate the stability of the doped BSCF-based materials. In general, doping BCN and LCT into BSCF perovskite largely improved thermal stability, CO_2 stability and chemical compatibility with state-of-the-art electrolytes, SDC.

Doping of 5%LCT into BSCF generated a material with much improved electronic conductivity which could be caused by the relative high amount of lattice oxygen released at elevated temperature, as evidenced by TGA results. However, other BCN- and LCT- doped compositions only exhibited much lower electronic conductivity than the parent BSCF material. Despite the relatively low conductivity, good area specific resistance (ASR) was observed with materials containing low doping level of BCN and LCT (5% and 10% doped). The ASR of these four materials were lower than $0.15\Omega.cm^2$ at 600°C, indicating the good cathodic performance of them. Long-term measurement of ASR of these four materials were also performed at 650°C for 72 hours and the material 0.1BCN-0.9BSCF displayed the lowest changing rate during the time period tested, even lower than that of the commercial BSCF, with the ASR measured at the end of the stability test at 650°C still below $0.15\Omega.cm^2$. The good stability of this particular material was also supported by the post-impedance PXRD which showed no obvious formation of extra phases.

Acknowledgement

I would like to express my deep appreciation to all those who - directly or indirectly - contributed to the work presented in this thesis. First and foremost I would like to thank my primary supervisor Prof. Matt Rosseinsky for giving me the opportunity to work in his group and cooperate with excellent scientists, his continued guidance and his inspiring scientific attitude. I would also like to thank especially my secondary supervisor Dr. John Claridge for his invaluable advice and always being there for questions.

With working in such a large research group, I have worked with many people and have enjoyed a lot of useful and inspiring discussions.

I am very grateful to Dr. Darren Hodgman for helping me at my first synthetic attempts and kept showing me the ropes in terms of synthesis, powder diffraction and solid state chemistry. Special thanks go to Dr. Maria Tsiamtsouri, Dr Ruth Sayers and Dr Hripsime Gasparyan who taught me enormous knowledge and experience in cathodes and electrochemical measurements. I was also lucky enough to work with Dr. Phil Chater, Dr Alex Corkett, who have been on hand on X-ray refinement discussion. I would also like to thank Dr. Hongjun Niu for all the technical support and Dr. Marco Zanella for the SEM images. Additionally my thanks goes to Dr Felix Shin for a lot of helpful discussion and guidance. It would be a serious omission if I didn't thank Dr. Mike Pitcher and Dr Matthew Dyer who have spent a lot of their time helping me planning for this thesis, reading my chapters and providing valuable advices.

Last but not least, I would like to thank all my families who have given me enormous help and support during my study.

Contents

Chapter 1 Introductions

1.1. Energy Concerns

The generation of energy by clean, efficient and environmental-friendly means is now one of the major challenges for engineers and scientists. It is now well established that global warming is taking place due to effluent gas emission, mainly CO_2, using traditional power generation based on oil, coal and natural gas.[1] During the past century, global surface temperatures have increased at a rate near 0.6°C/century.[2] These problems also caused severe environmental concerns such as air pollution, acid precipitation, ozone depletion, forest destruction, and emission of radioactive substances. World population keeps increasing at 1.2–2% per year, so that it is expected to reach 12 billion in 2050.[3] Therefore, economic development will almost certainly continue to grow. Global demand for energy services is expected to increase by as much as an order of magnitude by 2050, while primary-energy demands are expected to increase by 1.5 to 3 times. As worldwide oil supplies dwindle,[4] the development of new power generation technologies will become increasingly important. Simultaneously, interest will likely increase regarding energy-related environmental concerns. Indeed, energy is one of the main factors that must be considered in discussions of sustainable development. In response to the critical need for a cleaner energy technology, some potential solutions have evolved, including energy conservation through improved energy efficiency, reduction in the consumption of fossil fuels, and an increase in the supply of environmental-friendly energy, such as renewable sources and fuel cells.

Fuel cells convert chemical energy of a fuel gas directly into electrical work, and are efficient and environmentally clean, since no combustion is required. Moreover, fuel cells have the potential for development to a sufficient size for applications for commercial electricity generation.[1] Fuel cells come in many varieties, for example, there are proton exchange membrane fuel cells (PEMFCs), molten carbonate fuel cells (MCFCs) and solid oxide fuel cells (SOFCs). SOFC is the topic of this thesis and the principle of it is described in Section 1.2.

1.2. Operation of Solid Oxide Fuel Cells (SOFCs)

The solid oxide fuel cell (SOFC) is an all ceramic electrochemical power generation device.[5] The typical SOFC single cell consists of three main components: an anode, electrolyte and cathode. Each individual cell will provide power of the order of 1 W cm^{-2} and these cells can then be combined to form fuel cell stacks.[5] Figure 1.1 is a diagram showing the main components of the SOFC.

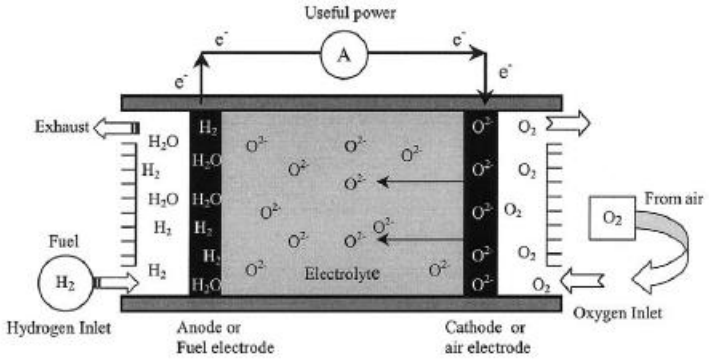

Fig 1.1. Concept diagram of SOFC based on oxygen-ion conductors. [1]

The cathode is typically an oxide that catalyses the oxygen reduction reaction, generating oxide ions:[6]

$$\frac{1}{2}O_2(g) + 2e^- \rightarrow O^=(s) \qquad \text{Equation 1.1}$$

The anode catalyses the oxidation of fuel, either hydrogen or reformed hydrocarbons:[6]

$$H_2(g) + O^= \rightarrow H_2O + 2e^- \qquad \text{Equation 1.2}$$

The dense electrolyte membrane separates the air and fuel compartments and is a pure oxygen ion conductor.[6] The ionic species pass from the cathode through the electrolyte to the anode where the fuel is oxidised and the chemical energy of the fuel is converted into electrical power resulting in water being produced as waste.

Typical SOFCs are based on yttria-stabilised zirconia (YSZ) electrolyte and operated at ≈1000ºC.[7] Such a high operating temperature is beneficial for improving the electrode reaction kinetics and reducing the electrolyte ohmic drop. However, it also introduces several serious drawbacks, such as a high possibility of interfacial reaction between the electrode and electrolyte to form insulating phase(s). The high operation temperature also limits the choice of the SOFC materials and can cause problems in arrangement for the seals that are necessary

in SOFC stacks.[7, 8]

Reducing the operating temperature of the SOFCs to an intermediate range, 500°C-800°C, would have advantages such as offering the possibility for more rapid start-up and shut-down procedures, simplifying the design and material requirements of the device and hence reducing its cost. However, it also leads to a significant increase in electrochemical resistance of key cell components. One way to reduce ohmic drop of the cell is to adopt a thin-film electrolyte. Different materials processing technologies, such as tape casting and spray pyrolysis, are used to decrease the thickness of the electrolyte whilst maintaining the required high density.[5,7] The anode is typically very catalytically active towards the hydrogen and hydrocarbon oxidation reaction but suffers stability issues at high temperature and reducing atmosphere. Among all three key components, the cathode is subject to large activation polarisation due to the sluggish reaction of the oxygen on its surface, producing a high overpotential.[5]

1.3. Cell Efficiency

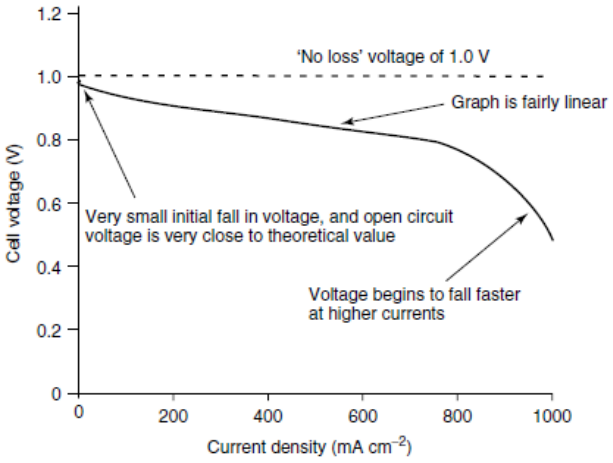

Figure 1.2. Graph showing the voltage of a typical air pressure fuel cell operating at about 800°C.[9]

The efficiency of reversible work converted to electrical work of a SOFC depends on the internal losses in the fuel cell, in which the ohmic loss from the electrolyte and the resistance caused by cathodic polarisation were very important parts.[5,7] Figure 1.2 shows the situation for a typical solid oxide fuel cell operating at about 800°C which shows that when a fuel cell is put to use, the voltage is less than the theoretical open circuit voltage.[9] This characteristic shape of the voltage/current density of fuel cell results mainly from the following four types of polarisation:[5] charge transfer (or activation) polarisation (η_a, typically associated with the

electrodes), diffusion or concentration polarisation (η_m, associated with mass transport), reaction polarisation (η_R, similar to concentration polarisation and generally small at high temperatures) and resistance or ohmic polarisation ($\eta_{\Omega=}jR$, associated with ionic and electronic conduction and contact between cell components).[5, 9]

These losses can be expressed by Equation 1.3, where the actual voltage output (V) under load is:

$$V = E_0 - \eta_a - \eta_m - \eta_R - jR \qquad \text{Equation 1.3}$$

where *Eo* is the theoretical cell voltage under open circuit and *jR* is equal to the ohmic polarisation loses and *R* represents the total cell resistance.[5, 9, 10] Therefore an important way of achieving increased efficiency is by lowering of the cell polarisation losses named before.

The resistances associated with each of the SOFC components can be normalised to the component area to give an area specific resistance (ASR, in $\Omega.cm^2$). Power densities of up to 1 $W.cm^{-2}$ have been achieved in the laboratory; however, practical power outputs are in the region of 0.5 $W.cm^{-2}$ at 80-90% fuel utilisation. Brandon et al.[10] gave the following example: for a fuel cell operating around 0.7 V, a power output of 0.5 $W.cm^{-2}$ requires a current density of at least 0.7 $A.cm^{-2}$. If the OCV is 1 V, then the allowed voltage loss (0.3V) can be achieved only if the ASR value does not exceed ~$0.45\Omega.cm^{-2}$. For a single cell assembly this implies target ASR value of $0.15\Omega.cm^{-2}$ for the individual cathode, anode and electrolyte components. Achieving a low ASR is a key requirement for an SOFC cathode.

1.4. Cathode for SOFC

The SOFC cathode functions as the site for the electrochemical reduction of oxygen. The elementary reactions in the overall electrode reaction are usually considered as follows:[11] (1) the reduction of O_2 molecules involving adsorption, dissociation, reduction, and incorporation of the oxygen anion into the lattice of the cathode materials; (2) ionic transport through the porous cathode toward the electrolyte; and (3) the ion jumping into the electrolyte lattice.

The triple phase boundary (TPB) is a key feature and is defined as the confluence of sites where the oxygen ion conductor, electronic conductor, and the gas phase come in contact.[11] Electrons are transported to the TPB in order to reduce O_2 to $2O^{2-}$. A TPB point in an SOFC

is shown in Figure 1.2(a) for a pure electronic conducting material which shows that a TPB only exists where the electrode, electrolyte and gas phase meet. Mixed ionic-electronic conducting (MIEC) electrode materials are of recent interest as in theory the active area is extended to the entire cathode surface area; the reaction steps at a MIEC cathode are illustrated in Figure 1.2(b).

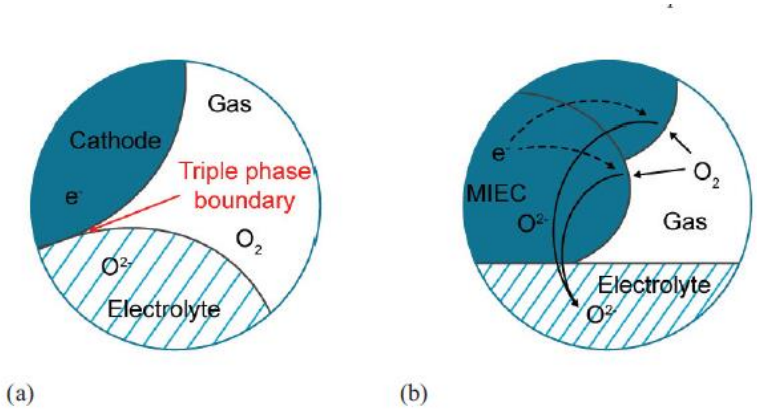

Figure 1.3: Schematic representation of (a) triple phase boundaries in electrodes and (b) reaction steps at TPBs for mixed ionic-electronic conductors.

Apart from the high electronic and ionic conductivity, the SOFC cathode material must meet other requirements such as: (1) a matched thermal expansion coefficient (TEC) and chemical compatibility with the electrolyte and interconnect materials; (2) adequate porosity to allow gaseous oxygen to readily diffuse through the cathode to the cathode/electrolyte interface; (3) stability under an oxidizing atmosphere during fabrication and operation; (4) high catalytic activity for the oxygen reduction reaction.[11]

1.5. Materials Review for Perovskite Structure Cathode

There are a lot of oxide structure types that have been studied as cathode materials, for example, perovskite, K_2NiF_4[6] and ordered perovskite and perovskite-related systems, and pyrochlore materials.[12] Perovskite materials and their structure will be introduced in more detail in this section because (1) most of the traditionally used cathodes have the perovskite structure, e.g., doped $LaMnO_3$ and $LaCoO_3$[7] and (2) the materials studied in this project have the perovskite structure.

The heterovalent atoms at the B-site of the perovskites showing more than one stable oxidation state compatible with the octahedral geometry (for example, $Mn^{3+/4+}$, $Fe^{3+/4+}$, and $Co^{2+/3+/4+}$)

provide the electronic conductivity. Also, the perovskite structure can host anion defects providing high concentration of mobile oxygen ion vacancies and thus ionic conductivity.

1.5.1. ABO3 Perovskite Oxides

The typical chemical formula of the perovskite structure is ABO_3, where A and B denote two different cations.[13] The typical structure consists of large-sized 12-coordinated cations at the A site and small-sized 6-coordinated cations at the B site.[13] The ideal structure of perovskite, as shown in Figure 1.3, is a cubic lattice. Although few compounds have this ideal cubic structure, many oxides have slightly distorted variants with lower symmetry. Goldschmidt introduced a tolerance factor (**t**) to evaluate the deviation from the ideal situation, which is defined by the following equation:

$$t = \frac{(r_A + r_O)}{\sqrt{2}(r_B + r_O)} \qquad \text{Equation 1.4}$$

where r_A is the radius of the A-cation, r_B is the radius of the B-cation, and r_0 is the radius of the anion (usually oxygen).

The value of ***t*** is applicable at room temperature to the empirical ionic radii. Although for an ideal perovskite, ***t*** is unity, this structure is also found for lower ***t***-values ($0.75 < \boldsymbol{t} < 1.0$). The ideal cubic perovskite structure appears in a few cases for ***t***-values very close to 1 and at high temperatures. In most cases, different distortions of the perovskite structure appear. For example, both $BaTiO_3$ and $SrTiO_3$ are cubic perovskites, while $CaTiO_3$ affords an orthorhombic structure as A ion is too small to fit into B ion interstices, which causes octahedral distortion.

Therefore, the structure family of perovskite is a large family of compounds with many possible cation combinations. The flexibility of this structure to accommodate almost all of the elements in the periodic system makes it an ideal structure family to search for new SOFC cathodes.[14]

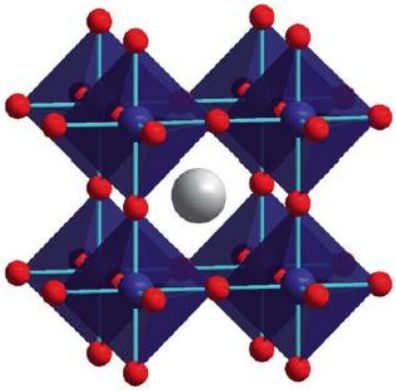

Figure 1.4: The ABO_3 cubic perovskite structure. Biggest grey sphere represents the A-site cations, blue spheres represent the B-site cations, and smallest red spheres are the O^{2-} ions.[15]

1.5.2. Layered Double Perovskites

When the ideal formula ABO_3 is changed to introduce different types of A and B cations on the octahedral site of the primitive unit cell, cationic ordering can lead to complex perovskites.[2] Cation ordering can have profound effects on the properties.[9] While cation ordering can be realised with either A- or B- site cations there are important differences in the way they order. In the vast majority of $A_2BB'X_6$ perovskites the B and B' cations take on an ordered pattern that is analogous to cation and anion positions in the rock salt structure (Figure 1.4). As a general rule when the oxidation states of B and B' differ by less than two a disordered arrangement is observed whereas, a difference greater than two nearly always produces an ordered arrangement. When the difference in oxidation states is exactly two, disordered, partially ordered, or fully ordered arrangements can result, depending on differences in size and/ or bonding preference of the B and B' cations.[9, 16, 17]

As shown on Figure 1.4,[15] there are three simple patterns of ordering that can be envisioned for either the A- or B-site cations. The most symmetric is called rock salt ordering because the pattern of B and B' (or A and A') cations is equivalent to the anion and cation positions in the rock salt structure. In addition to the rock salt ordering, cations can order into columns, or layers.

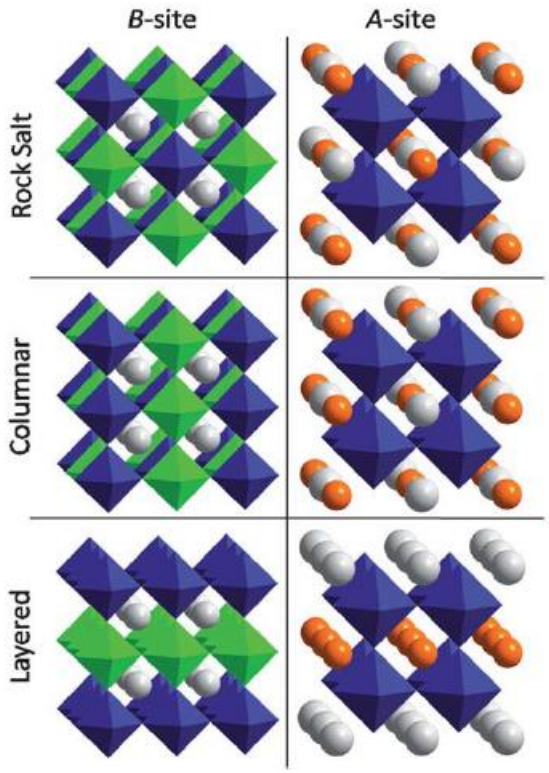

Figure 1.5: Cation ordering schemes in perovskites. From top to bottom 0D (rock salt), 1D (columnar ordering) and 2D (layered ordering) are shown for B-site ordering in $A_2BB'X_6$ perovskites (left) and for A-site ordering in $AA'B_2X_6$ (right) perovskites.[15]

1.5.3. BSCF Perovskite SOFC Cathode

The state-of-the-art perovskite cathode materials are (La,Sr)$MnO_{3-\delta}$ (LSM) and $La_{0.6}Sr_{0.4}Co_{0.2}Fe_{0.8}O_{3-\delta}$ (LSCF) and they have been intensively studied during the last two decades.[8] LSM displays good performance at higher operating temperatures (~900°C) due to its high electrical conductivity, high electrochemical activity for the O_2 reduction reaction, high thermal stability, and compatibility with YSZ, GDC, and LSGM at operating conditions.[6] The electronic conductivity of LSM increases approximately linearly with increasing Sr concentration, as the Mn^{4+} fraction increases, up to a maximum around 50 mol%; with conductivity of 320 $S.cm^{-1}$ at 800°C for the $La_{0.6}Sr_{0.4}MnO_{3-\delta}$ composition.[18, 19] The main drawback of LSM is the poor ionic conductivity: (10^{-7} $S.cm^{-1}$ at 900ºC). LSCF is a mixed ionic and electronic conductor (MIEC) and it shows similar electronic conductivity as LSM but much improved oxygen ionic conductivity (in the order of 10^{-3} $S.cm^{-1}$ at 750°C) than LSM at high temperature.

Driven by the requirement of lowering SOFC operation temperature, many new compositions

have been proposed and tested, and (Ba,Sr)(Co,Fe)$O_{3-\delta}$ (BSCF) is one of the most attractive candidates with respect to high oxygen diffusivity and fast oxygen reduction kinetics.[20] It was reported to give very low area specific resistances (ASR) of 0.055-0.071 ohms.cm^2 at 600^{o}C, and 0.51-0.60 ohms.cm^2 at 500^{o}C in a $Sm_{0.2}Ce_{0.8}O_{1.9}$ (SDC) electrolyte-based fuel cell for the specific composition $Ba_{0.5}Sr_{0.5}Co_{0.8}Fe_{0.2}O_{3-\delta}$.[20] There might be some intrinsic shortcomings of this material that prevent it from being an ideal SOFC cathode material, such as the formation of carbonate in the presence of CO_2 and limited compatibility with the electrolyte. BSCF also has a much larger thermal expansion coefficient (TEC) than most of the electrolytes. Owing to this mismatch, in some cases, the high TEC even resulted in the BSCF cathode being peeled off from the electrolyte.[21] In general, increasing Fe content in BSCF materials improves the stability towards CO_2 and also the TEC, but also increases the ASR of the material.

However, the results have generated much interest and the system has been studied by several groups. Li et al. reported that by doping a rare earth metal into A sites of BSCF with the formation of $(Ba_{0.5}Sr_{0.5})_{1-\mathbf{x}}Sm_{\mathbf{x}}Co_{0.8}Fe_{0.2}O_{3-\boldsymbol{\delta}}$ (BSSCF; **x** = 0.05–0.15), the conductivity was improved, 21.2% improvement as compared to pristine BSCF at 500^{o}C for the **x** = 0.15 compound.[22, 23] Electrochemical impedance spectra at intermediate temperatures also revealed a better electrochemical performance of BSSCF than BSCF; e.g., the total resistance values of BSSCF electrode is nearly 50% lower than that of BSCF. However, the TEC of these doped compounds is 19.1–20.3×10^{-6} K^{-1} from 30°C to 800^{o}C, which is even higher than the values of BSCF. The doping of La or Nd had a similar effect on the cathode performance.[24, 25]

The substitution of cobalt by more chemically stable ions, such as Ti, is expected to decrease the TEC of the compounds.[26] $Ba_{0.6}Sr_{0.4}Co_{1-y}Ti_yO_{3-\delta}$ (BSCT) oxides showed a TEC of about 14×10^{-6} K^{-1} at y = 0.2, which results in a good physical compatibility of BSCT with GDC electrolyte. BSCT also shows excellent thermal cyclic stability of electrical conductivity and good chemical stability with GDC. These properties make BSCT a promising cathode candidate for intermediate temperature solid-oxide fuel cells (IT-SOFCs). Ovenstone et al. used in situ X-ray diffraction to investigate the phase stability of $Ba_{0.5}Sr_{0.5}Co_yFe_{1-y}O_{3-\delta}$ (y = 0–1). The thermal decomposition processes both in low partial pressures of oxygen (0.21 to 10^{-5} atm pO_2) and in reducing conditions has been studied in detail. BSCF manifested excellent stability down to 10^{-5} atm pO_2; however, it decomposed through a complex series of oxides under more reducing conditions. Increasing the cobalt content resulted in a decrease

in the temperature range of stability of the material under 4% H_2 in N_2, with the initial decomposition taking place at 375, 425, 550, 600, 650, and 675ºC, for y = 1, 0.8, 0.6, 0.4, 0.2, and 0, respectively.

Generally, cobalt-based perovskite oxides exhibit large TEC values, which is attributable to the electronic spin state transitions associated with the Co^{3+}.[27] Co^{3+} ions will transform from the low-spin state to high-spin state with increasing temperature, and the ionic radius is larger for high-spin state compared to the low-spin state. On the other hand, Ti^{4+} ions are more stable at high temperatures, while the Co^{4+} ions are apt to be reduced to Co^{3+} ions with the generation of corresponding amount of oxide ion vacancies. Both the formation of Co^{3+} with larger size than Co^{4+} and the generation of oxygen vacancy will lead to the lattice expansion. As a result, the substitution of Ti for Co in BSCT can apparently decrease the electronic spin state transition temperature of Co^{3+} ions and reduce the Co^{3+} and oxygen vacancy concentrations, thus consequently resulting in the lower thermal expansion coefficient.

Mo-containing compounds such as Ba_2CoMoO_6 and $Ba_2CoMo_{0.5}Nb_{0.5}O_{6-\delta}$ are reported to be highly stable compounds. Moreover, molybdenum compounds are well known catalysts with high activity for selective oxidation of hydrocarbons.[28, 29] Ba_2CoMoO_6 as shown in Figure 1.6 is a double perovskite with space-group of *Fm-3m*. It crystallise with FCC arrangement of Co and B ions in rock-salt order.[30] Doping of Mo^{6+} in the B-site has been investigated[31] in order to enhance the performance of BSCF as a SOFC cathode (BSCFMo). By introduction of Mo, a mixture of single perovskite (SP) and double perovskite (DP) was detected (for 0.2 < Mo < 0.4, for Co/Fe = 4). The compound with nominal composition $Ba_{0.5}Sr_{0.5}Co_{0.5}Fe_{0.125}Mo_{0.375}O_{3-\delta}$ showed the best electrochemical performance among the compositions studied, with ASR values of 0.055 and 0.351 ohms.cm^2 at 700ºC and 600ºC, respectively. This specific material possesses a coherent endotaxial intergrowth of a cation-ordered, anion vacancy-free Mo-rich DP phase, which is thought to be a pure electronic conductor and a Fe-rich SP phase, serves as the mixed ionic and electronic conductivity (MIEC) part, with vacancies for oxide transport and ORR active at all interfaces with air (Fig 1.7) . This interesting structure increases the stability of the cubic perovskite with respect to competing structures over that of the single-phase parent material. The SP/DP composite performs well as an SOFC cathode, exceeding expectations based on the local compositions of the constituent phases (one of which is not capable of anion transport).

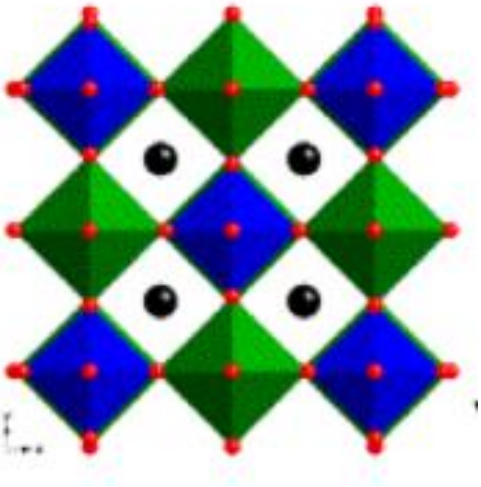

Fig 1.6. Schematic crystal structures of double perovskite Ba_2CoMoO_6 in space group of Fm-3m. Black and red spheres represent the Ba^{2+} and O^{2-} ions, blue and green octahedral shows the corner sharing CoO_6 and MoO_6 respectively. [30]

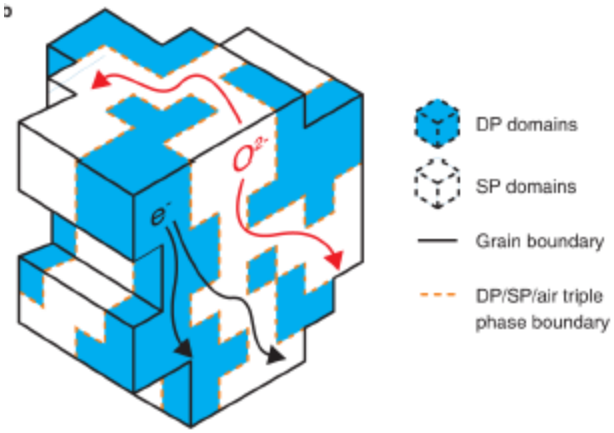

Fig 1.7., Schematic representation of oxygen ion (red) and electron (black) transport pathways available in a two-phase endotaxial composite grain. The SP/DP/air triple phase boundary is highlighted as an orange dotted line.[31]

1.6. Aim of This Work

1.6.1. $Ba_3CoNb_2O_9$ (BCN) and La_2CoTiO_6 (LCT)

$Ba_3CoNb_2O_9$ (BCN) is an ordered perovskite that crystallises in a hexagonal structure with the space group *P-3m1*. An illustration showing the structure of the material is shown in Figure 1.8(a) and (b), which shows that neighboring NbO_6 octahedra linked sharing their corners. This material has attracted interest due to its good microwave dielectric constant, the Q-value and the temperature coefficient of resonance.[32]

A B-site order-disorder phase transition at ~1425°C has been reported to occur and shown to have a strongly deleterious effect upon the microwave dielectric loss property.[32, 33]

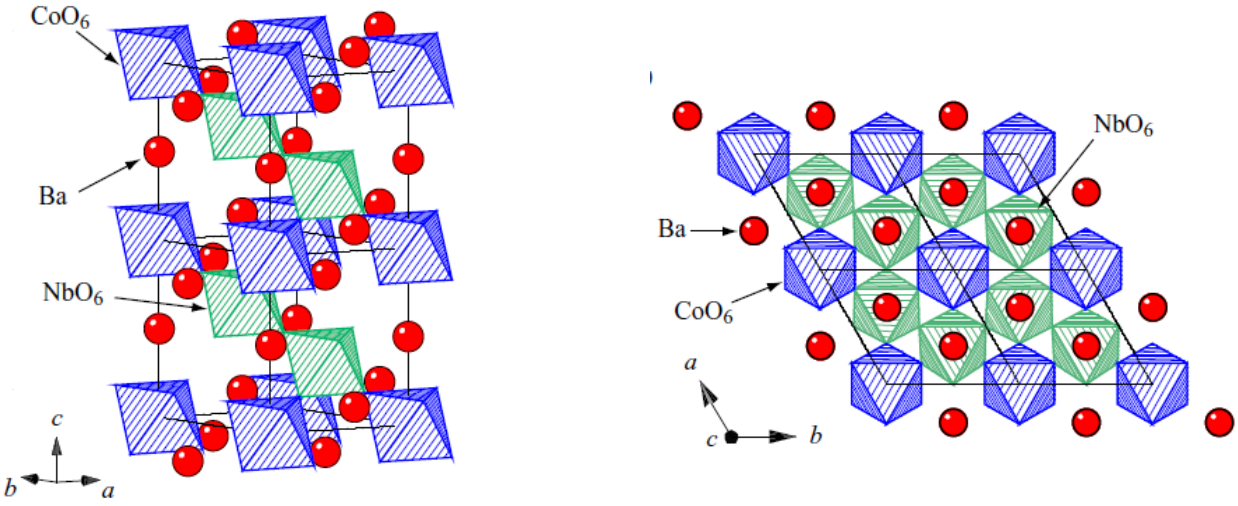

Fig 1.8(a). Schematic crystal structures of $Ba_3CoNb_2O_9$. (b). Arrangement of CoO_6 and NbO_6 octahedra in $Ba_3CoNb_2O_9$ viewed along the c axis. The solid lines show the chemical unit cell. (pictures are copied and modified from[34]).

La_2CoTiO_6 (LCT) is a double perovskite with symmetry $P2_1/n$. $LaCo_{1-x}Ti_xO_3$ system was studied by many researchers in order to change the properties of $LaCoO_3$, where Ti^{4+} is substituted for Co^{3+}. It is found that for every Co^{3+} substituted by the smaller Ti^{4+}, one Co^{3+} is reduced to a larger Co^{2+} to keep charge neutrality. When the amount of Ti^{4+} is high enough (x = 0.4, 0.5), the Ti and Co atoms start to order and forms the double perovskite structure as illustrated in Figure 1.9. The lattice expansion is thus explained by an increasing amount of Co^{2+} ions with large ionic radius than those of Co^{3+} and Ti^{4+}.[35] Parkash et al[36] have studied the effect of the substitution and Co by Ti upon the electronic properties and adding more Ti

increase the resistance of the material. This is probably caused by a decrease in the electron mobility resulting from the trapping of electrons in Ti^{4+}-Co^{2+} clusters.

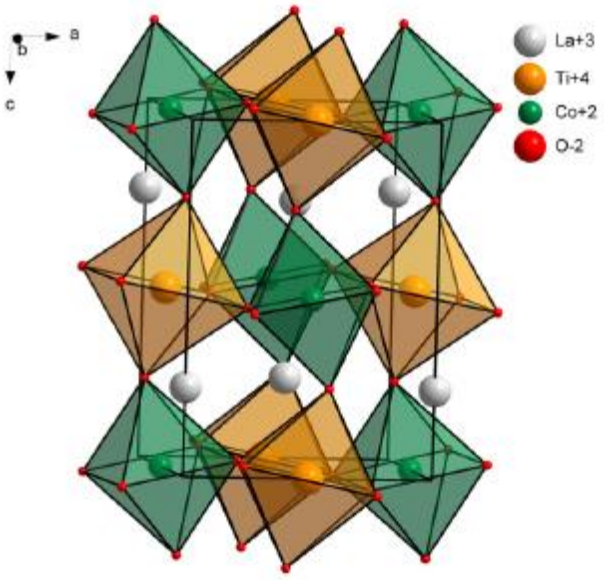

Fig 1.9, Illustration of the double perovskite P21/n structure of La_2CoTiO_6 with alternating Co^{2+} and Ti^{4+} octahedral. (picture copied from [37])

1.6.2. Aim of This Work

The co-existence of SP/DP phase in the BSCFMo material showed improved thermal stability and compatibility while kept low ASR value. In this work, we aim to chemically combine the parent single perovskite (SP) material BSCF with double perovskite (DP)- La_2CoTiO_6, or even triple perovskite-$Ba_3CoNb_2O_9$, and to investigate the effect of chemically combining these different phase on the structure, properties and the performance of the materials and their potential to be used as cathode material for intermediate SOFC (IT-SOFC). The research on the new materials presented in this thesis can be broadly grouped into three areas: (1) the structure-whether they form a solid solution or an endotaxial phase separation, (2) the thermal and chemical structure stability, and (3), the electrochemical performance with typical IT-SOFC electrolytes.

Chapter 2 Experiment Methods

2.1. Synthesis

Conventional solid state synthesis was the method used in this thesis for the preparation of target phases. There are generally several steps involved in the solid state synthesis, starting with weighing out the appropriate starting materials, usually oxides and carbonates, in stoichiometric proportion. Multicomponent starting materials are mixed by either hand-grinding or ball-milling to reduce particle size and increase homogeneity within the sample. Hand-grinding is often done by using agate mortar and pestle assisted by the use of organic solvent. [38, 39]

Comminuted powders are then pelletised and placed in appropriately chosen sample container for the subsequent annealing/synthesis. Sample containers can be ceramic refractories (such as Al_2O_3 and ZrO_2), precious metals (such as Pt and Au) or sealed tubes. Sample containers chosen for the reaction must be able to withstand high temperatures and be sufficiently inert to the reactants. The purpose of palletising powders is to enhance intimate contact of reactants and to minimise contact with the crucible.[38, 39]

The pelletised powder is then annealing in the furnace (box furnace or tube furnace) for a wide range of timescales, from hours to weeks depending on requirements. The annealing process sometimes consists of an initial heating cycle to lower temperature followed by a high temperature step. The initial lower temperature heating cycle can help to prevent spillage and volatilisation. High temperatures are required, often exceeding 1400°C, in order to enable ion diffusion to overcome kinetic barriers, along with long timescales due to the slow rate of diffusion in many cases. The material after annealing is then ground and analysed, normally by x-ray powder diffraction and if reaction is incomplete, the annealing/firing maybe repeated several time with intermediate grinding stage to ensure that the reaction is completed. [38]

2.2. Powder Diffraction Techniques

2.2.1. Crystal Symmetry

All phases prepared in this thesis are crystalline in nature, which has allowed the extensive use of powder diffraction for characterizing their crystal structure. The periodic structure of an ideal crystal is most easily described by a lattice. In a lattice, all elementary parallelepipeds,

that is, unit cells are equal in their shape and content. Most importantly, if the distribution of atoms in one unit cell is known, the structure of the whole crystal, regardless of its physical size, can be reconstructed by simply propagating (translating or shifting) this unit cell along one, two, or three directions independently. [40]

To fully describe a three-dimensional lattice or its building block – the unit cell – a total of three noncoplanar vectors are required. These vectors (*a*,*b*,*c*) coincide with the three independent edges of the elementary parallelepiped, as shown schematically in Fig. 2.1. The unit cell can be completely described by specifying a total of six scalar quantities, which are called the unit cell dimensions or lattice parameters. These are (see also Fig. 2.1):

$$a, b, c, \alpha, \beta, \gamma$$

The first three parameters (*a*, *b* and *c*) represent the lengths of the unit cell edges, and the last three (*α*,*β* and *γ*) represent the angles between them. By convention, *α* is the angle between *b* and *c*, *β* is the angle between *a* and *c*, and *γ* is the angle between *a* and *b*. Unit cell parameters are usually quoted in angstroms (Å, where 1Å $=10^{-10}$ m$=10^{-8}$ cm), nanometers (nm,1 nm$=10^{-9}$ m), or picometers (pm,1pm $= 10^{-12}$ m) for the lengths of the unit cell edges, and in degrees (°) for the angles between basis vectors.[40]

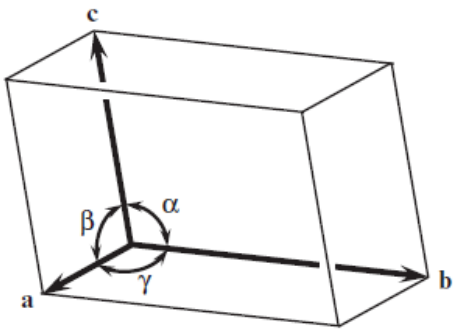

Fig 2.1. Unit cell in three dimensions.[40]

Crystal lattices can be classified to seven crystal/lattice systems, according to the relation between the edges of the unit cell of length (*a*, *b*, *c*) and the relation between the angles (*α*, *β*, *γ*) between them (*Table 2.1*).

Table 2.1. The seven crystal systems together with their characteristic unit cell parameters.

Crystal system	Unit cell edges	Unit cell angles
Triclinic	a≠b≠c	α≠β≠γ
Monoclinic	a≠b≠c	α=γ= 90°, β≠90°
Orthorhombic	a≠b≠c	α=β=γ= 90°
Tetragonal	a=b≠c	α=β=γ= 90°
Hexagonal	a=b≠c	α=β= 90°, γ= 120°
Trigonal	a=b=c	α=β=γ≠ 90°
Cubic	a=b=c	α=β=γ= 90°

A family of crystallographic planes is defined as a set of planes that intersect all lattice points. All planes in the same family are necessarily: (1) parallel to each other, and (2) equally spaced. The distance between the neighbouring planes is called the interplanar distance or *d*-spacing. The crystallographic plane is a geometrical concept introduced to illustrate the phenomenon of diffraction from ideal crystal lattices, since algebraic equations that govern diffraction process are difficult to visualise.[40]

2.2.2. X-ray and Fundamentals of Diffraction

It is well-known that when a wave interacts with and is scattered by a point object, the outcome of this interaction is a new wave, which spreads in all directions. When two or more points are involved, they all produce spherical waves with the same wavelength (λ), which interfere with each other. If the two scattered waves with parallel-propagation vectors are completely in-phase, the resulting wave has its amplitude doubled, which is called constructive interference. Constructive interference, which occurs on periodic arrays of points, increases the resultant wave amplitude by many orders of magnitude and this phenomenon is one of the cornerstones in the theory of diffraction. Diffraction can be observed only when the wavelength is of the same order of magnitude as the repetitive distance between the scattering objects. Thus, for

crystals, the wavelength should be in the same range as the shortest interatomic distances, that is, somewhere between ~0.5 and ~2.5 Å.[40]

Due to the periodic nature of a crystalline material, structural characterisation by diffraction is a powerful tool. X-rays, neutrons and electrons can all be used in diffraction experiments due to their appropriate wavelength, which is in the order of magnitude of atomic radii and inter atomic spacing.

One of the most useful rules to describe the relationships between the directions of the incident and diffracted beams, is the law formulated by W.H.Bragg and W.L.Bragg, It establishes certain relationships among the diffraction angle (Bragg angle, θ), wavelength (λ), and interplanar spacing (*d*-spacing).

The principle of Bragg's Law is illustrated in Figure 2.2, which considers the path difference between the waves scattered by atoms from adjacent (*hkl*) lattice planes.

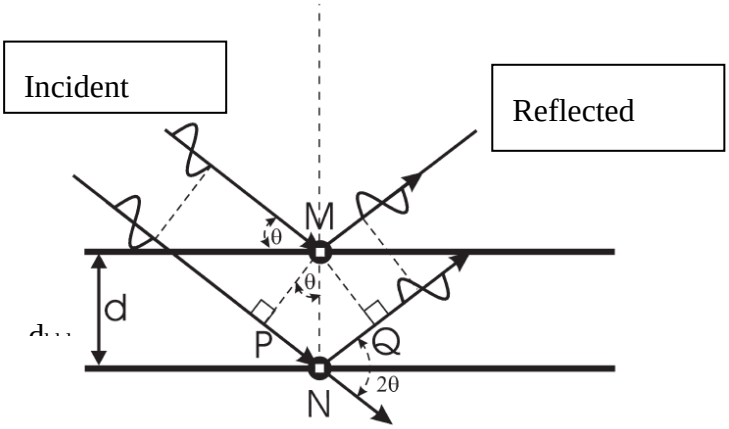

Figure 2.2: Illustration of the geometry used for the Bragg's Law[4].

From Figure 2.2 it can be seen that the path difference between the reflected beams can be expressed in terms of the distance between planes of atoms (d_{hkl}) and the X-ray angle of incidence (θ), given in Equation 2.1.

$$(PN + NQ) = 2d_{hkl} \sin\theta \qquad \text{Equation 2.1.}$$

For constructive interference, the path difference can be written as Equation 2.2.

$$n\lambda = 2d_{hkl} \sin\theta \qquad \text{Equation 2.2.}$$

where *n* is an integer for the order of reflection (or diffraction) and λ is the wavelength of the incident X-rays.

Information on the position of lattice planes can then be determined from the intensity and angle of the reflected x-rays. The resultant XRD pattern of a crystalline material can be

analysed based on the peak positions (i.e. angles) which correspond to specific lattice spacings and the relative intensity of the peaks.

2.2.3. X-ray Diffraction (XRD)

X-rays are electromagnetic radiation of wavelength ~1 Å.[41] They can be generated either by laboratory or synchrotron sources through different processes, but in both cases resulting in monochromatic X-rays required for XRD.[42] In XRD experiments, the intensity of the diffracted beam is measured as a function of 2θ, which is the angle between the diffracted and undiffracted beams.

In laboratory based powder X-ray diffractometers,[41, 42] electrons are produced by heating a metal filament, usually tungsten, and then accelerated through a voltage of 40 kV to bombard a metal target. The bombardment of high energy electrons cause ionisation of the core K-shell (n = 1) electrons of the target anode. Electrons from outer orbitals fill the holes created in the core shell by the ionisation of ions; by this X-rays are emitted with energy corresponding to the energy gap between the two electronic states and hence have different wavelength than the radiation for diffraction. Electrons originating from the L shell (n = 2) give rise to Kα radiation, and electrons from the M shell (n = 3) give rise to Kβ radiation; both comprise of two components: Kα1 and Kα2, and Kβ1 and Kβ2, respectively, because the transition has a slightly different energy for the two possible spin states of an electron. The Kα radiation is more intense than Kβ, as it occurs more often, and it is the one used in diffraction experiments. Since a monochromatic X-ray beam is desired for the XRD experiments, the Kβ radiation has to be removed; Kβ1 is absorbed by appropriate filters depending on the target material (Fe filter for Co target) and Kβ2 can be removed with the use of an appropriate monochromator.

2.2.4. Neutron Sources and Neutron Diffraction

Accelerated particles, such as neutrons, possess wave-like characteristics as described by the de Broglie relationship (Equation 2.3). The neutrons that are used for diffraction have wavelengths of the order 0.5 to 3Å. [41, 43]

$$\lambda = \frac{h}{p} \qquad \text{Equation 2.3.}$$

where p is momentum and h the Plank constant.

For neutron diffraction (ND),[44, 45] neutrons are scattered by the nuclei of the atoms. The cross-section (σ) is equivalent to the effective area presented by the nucleus to the passing neutron. The scattering power of a nucleus is expressed by the neutron coherent scattering length (b_{coh}), as if b_{coh} is the half of the radius of the nucleus as seen by a neutron (Equation 2.4) and the incoherent scattering results in general background noise in the data.

$$\sigma = \pi r r^2 = \pi(2b_{coh})^2 = 4\pi {b_{coh}}^2 \qquad \text{Equation 2.4.}$$

The scattering power of an atom is thus determined by the interaction of neutrons with atoms in a manner that does not correlate to the atomic number (Z) as in the case of XRD. This makes ND complementary to XRD, giving structural information for isoelectronic atoms and light atoms in the presence of heavier one.[41]

The neutron diffraction (ND) experiments for this thesis were carried out at the HRPD (High Resolution Powder Diffractometer) station in ISIS.[46] HRPD is the highest resolution neutron powder diffractometer of its type in the world; this is due to its being situated 100m away from the target, as resolution increases with distance from the target. HRPD has three fixed detector banks at 30°, at 90° and the highest-resolution back-scattering detector at 168°.

2.2.5. Synchrotron Diffraction

In a synchrotron,[47, 48] the electrons are produced in an electron gun where the cathode is under high voltage and heated in a vacuum. The electrons are accelerated to near light-speed by a sequence of particle accelerators and finely tuned bending magnets, producing an extremely intense synchrotron radiation in large storage rings. The synchrotron radiation consists of wavelengths from infra-red to X-rays; a specific X-ray wavelength can be selected by using appropriate monochromators.

High resolution synchrotron diffraction data were collected at the beamline station I11.[49] Samples were loaded in capillaries made by borosilicate of 0.3mm. The wavelength of the X-ray beam was λ = 0.825988Å. Scans were collected over a 2θ range of 2 to 150° and a step size of 0.005°, at room temperature.

2.2.6. Structure Solution and Pawley Method

Pawley fitting is a process in which observed peaks in a powder pattern are fitted without a structural model but at 2θ values constrained by the size and symmetry of the unit cell.[50] It is a useful precursor to Rietveld fitting and gives an indication of the "best fit possible" from an eventual structural refinement. It is also important before structure solution to either extract intensities for e.g. direct methods or to determine e.g. cell parameters and peak shapes for simulated annealing structure solutions.[50]

In order to solve a structure from powder diffraction data it is necessary to extract as many *hkl* and intensity values as possible from the data set.[50] According to Pawley method, angle-dispersive powder diffraction profiles could be fitted with only the following parameters:

- *I(hkl)* – Intensity of each reflection with indices *hkl*;
- *A, B, C, D, E, F* – Unit-cell metric tensor parameters;
- 2θ zero – Instrumental zero error;
- *U, V, W* – Peak-width parameters;
- H, etc – other peak-shape parameters.

Many of the parameters are the identical to those used in a Rietveld refinement program, but the significant difference is that *every* reflection is assumed to have (i) a peak position determined by *A*, *B*, *C*, *D*, *E*, *F*, and the 2θ zero error, (ii) a peak width determined by the resolution function parameters *U*, *V*, and *W*, and (ii) a peak intensity *I*(*hkl*). This can be contrasted to the Rietveld method, in which the intensity of the peaks is calculated from the structure factors, *F*(*hkl*), which are themselves calculated from the parameters of the model structure.[50]

2.2.7. Structure Refinement and Rietveld Refinement

The Rietveld structural refinement is an indirect method to obtain structural information from diffraction data and is based on the comparison between a theoretical pattern obtained from a structural model and the experimental pattern.[51] The refinements in this thesis were carried out by the software TOPAS Academic.[52]

The Rietveld method relies on a reasonable accurate starting theoretical model and a close resemble to the actual crystal structure is achieved by refining this model to fit the observed

data. The difference between the experimental diffraction pattern and the theoretical pattern is expressed by the residual function (S_y) for an (i) number of steps:

$$S_y = \sum_i W_i (y_i^{obs} - y_i^{calc})^2 \qquad \text{Equation 2.5}$$

And $$W_i = {}^{1}/_{\sigma^2(y_i^{obs})} \qquad \text{Equation 2.6}$$

where $\boldsymbol{y_i^{obs}}$ and $\boldsymbol{y_i^{calc}}$ are the observed and calculated intensities at the *i*th step, W_i the weight of the squared difference in intensities at the *i*th step and σ the uncertainty estimate[53, 54] (or estimated standard deviation) of $\boldsymbol{y_i^{obs}}$.

In a Rietveld refinement, firstly all non-structurally related parameters should be considered, such as zero shift, background and profile function, as well as lattice parameters. These parameters can be difficult to fit however, if the starting structural model is far from the actual structure, giving a poor fit. One way of temporarily ignoring the structural model is by fitting the data by Le Bail[55] or Pawley[56] procedures, with the latter used in this thesis.

After each iteration, the quality of the fit should be scrutinised, with care being taken regarding the physical meaning of refined values for the structural model. The quality of the refinement can be evaluated through statistical outputs known as *R*-factors. The profile factor, R_P, is defined as:

$$R_p = \frac{\sum_i \left| y_i^{obs} - y_i^{calc} \right|}{\sum_i y_i^{obs}} \qquad \text{Equation 2.7}$$

The weighted profile *R*-factor, R_{wp}, is the most straightforward statistical parameter that comes directly from the residual function seen in Equation 2.5:

$$R_{wp} = \sqrt{\frac{\sum_i w_i (y_i^{obs} - y_i^{calc})^2}{\sum_i w_i {y_i^{obs}}^2}} = \sqrt{\frac{S_y}{\sum_i W_i y_i^{obs}}} \qquad \text{Equation 2.8}$$

The best possible R_{wp} for a specific data set that can be obtained is called the expected *R*-factor, R_{exp}, which is given in the following equation:

$$R_{exp} = \sqrt{\frac{N_{obs} - N_{var}}{\sum_i w_i (y_i^{obs})^2}} \qquad \text{Equation 2.9}$$

Where N_{obs} is the number of observations and N_{var} is the number of refined parameters. In typical powder diffraction experiments, we expect N_{obs} to be much greater than N_{var} . If a refined model gave a perfect fit, with only difference occurring due to statistical variation, the

R_{exp} would represent the R_{wp}. The parameter for goodness of fit, χ, can be defined in terms of R_{exp} and R_{wp}:

$$\chi^2 = (\frac{R_{wp}}{R_{exp}})^2 \qquad \text{Equation 3.0}$$

Since the R_{exp} should not be greater than R_{wp}, the χ^2 should always be ≥ 1. Under certain conditions however, the χ^2 can be misleadingly low, such as when too many variables are being used. When a sufficient number of data points have been collected and counting time has been carried out so that the data is not dominated by a high background intensity, y_i^b, a $\chi^2 < 2$ should be obtained for a good structural model.

2.3. Thermogravimetric Analysis (TGA)

Thermogravimetric analysis (TGA) measures weight changes as a function of temperature and/or time. While heating, a material can lose mass due to dehydration, or the loss of compounds such as CO_2. For dry oxide materials, TGA is useful in monitoring weight changes related to changes in oxygen content and therefore oxidation states of the constituent elements. Oxidation of a specimen can lead to weight gain, whilst reduction results in weight loss. In addition, weight loss can indicate decomposition and formation of volatile products.

2.4. Electrical Characterisation

The electrical properties of the cathode materials presented in this thesis were measured by two methods: (a) conductivity measurements by the four-probe direct current (DC) method (b) impedance measurements by alternating current (AC) two-probe impedance spectroscopy; the methods principles are discussed below in *Sections 2.4.1* and *2.4.2* respectively.

2.4.1. Electrical Conductivity Measurements

Electrical conductivity (σ) is defined as the inverse of electrical resistivity (ρ, units: Ω.m), which is the property of a material to oppose the flow of an electric current. The electrical resistivity is dependent on the geometry of a specimen, as expressed by the following equation:

$$\rho = \frac{RA}{l} \qquad \text{Equation 3.1}$$

And $$\sigma = \frac{1}{\rho}$$ Equation 3.2.

where A is the cross-sectional area (units: m^2) , l is the length (units: m) and R is the electrical resistance (units: Ω) of the specimen. The electrical resistance (R) is defined as the ratio of the voltage (V) experienced by an electric current (I) that flows through it, according to Ohm's law:

$$R = \frac{V}{I}$$ Equation 3.3.

The four-probe DC method uses a simple apparatus to measure the voltage generated by a passing current to a specimen. The electrical resistivity and conductivity of the material can be then calculated by *Equation 3.1* and *Equation 3.2*.

The four probe DC method requires only quite a simple set-up, with voltage measured as a current is passed through the sample. From the observed R, the conductivity can be easily calculated using Equation 3.1 to 3.3. The four probe set up, consists of two inner probes to measure V and two outer I probes. Separation of the I and V electrodes eliminates contribution from wiring and contact resistances.[57]

2.4.2. AC Electrochemical Impedance Spectroscopy (EIS)

In DC theory (a special case of AC theory where the frequency equals 0 Hz), resistance is defined by Ohm's Law:[58]

$$V = IR$$ Equation 3.4.

Using the above Ohm's law, you can apply a DC potential V to a circuit, measure the resulting current (I), and compute the resistance (R). Potential values are measured in volts (V), current in amperes or amps (A), and resistance in ohms (Ω). A resistor is the only element that impedes the flow of electrons in a DC circuit.

In as theory, where the frequency is non-zero, the analogous equation is:

$$V = IZ$$ Equation 3.5

As in Equation 3.4, V and I are here defined as potential and current, respectively. Z is defined as impedance, the ac equivalent to resistance. Impedance values are also measured in ohms (Ω).

Like resistance, impedance also denotes the ability of a material to resist the current that passes through a material. In addition to resistors, in AC circuits, two other elements, capacitors and

inductors impede the flow of electrons, as it takes into account different processes that can affect the passing current in a real electrochemical system.

Electrochemical impedance [59] is usually measured by applying a single frequency sinusoidal AC voltage (*Equation 3.6*) to an electrochemical cell and measuring the current through the cell (*Equation 3.7*).

$$V(t) = V_0 \sin(\omega t) \qquad \text{Equation 3.6.}$$

$$I(t) = I_0 \sin(\omega t + \theta) \qquad \text{Equation 3.7.}$$

Where $\mathrm{V}(t)$ and $I(t)$ are the signals of voltage and current respectively at time t, V_0 and I_0 their magnitude, θ the phase difference between them, and ω the radial frequency (rad/sec), which is related to the frequency (f, Hz) by: $\omega = 2\pi f$.

An expression analogous to Ohm's law allows us to calculate the impedance of the system as:

$$Z(\omega) = \frac{V(t)}{I(t)} = \frac{V_0 \sin(\omega t)}{I_0 \sin(\omega t + \theta)} = Z_0 \frac{\sin(\omega t)}{\sin(\omega t + \theta)} \qquad \text{Equation 3.8.}$$

The impedance is therefore expressed in terms of a magnitude, Z_0, and the phase shift, θ.

EIS techniques use very small excitation amplitudes, often in the range of 5 to 10 mV peak-to-peak. Excitation waveforms of this amplitude cause only minimal perturbation of the electrochemical test system, reducing errors caused by the measurement technique.

Frequency dependant impedance, *Z(ω)* can also be expressed as a complex number with real (*Z'*) and imaginary (*Z''*) parts:

$$Z(\omega) = \frac{V}{I} = Z_0 \exp(j\theta) = Z_0(\cos\theta + j\sin\theta) = Z' + jZ'' \qquad \text{Equation 3.9.}$$

The expression for *Z* is composed of a real (*Z'*) and an imaginary (*Z''*) part. If the real part is plotted on the x-axis and the imaginary part is plotted on the y-axis of a chart, we get a "Nyquist Plot") (see Fig 2.4.1.2). Each point on the Nyquist plot is the impedance at one frequency.

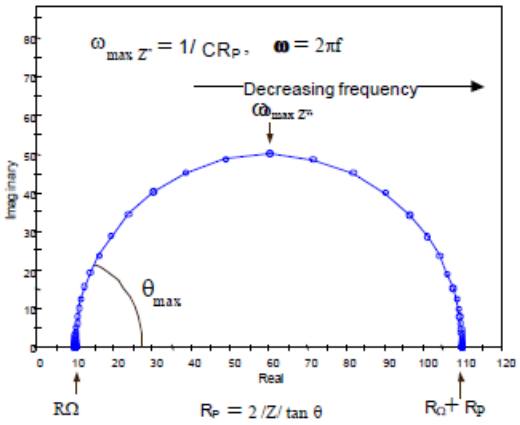

Fig 2.3. Nyquist Plot for a simple electrochemical system

The measured resistance for the cathode was converted to area specific resistance (ASR) by normalising and dividing by two to take into account the symmetry of the cell.

$$Area\ Specific\ Resistance\ (ASR) = RA/2$$

Where the resistance (R) is normalised for the cathodes surface area (A) and divided by 2 to take into account the cell symmetry. The ASR accounts for electronic conductivity, ionic conductivity, transfer of electrons and ions at interfaces and electrochemical activity per area of the cathode, and can therefore be scaled and directly compared to measured cells of different sizes.[60]

Chapter 3 Synthesis and Characterisation of Two BSCF-based Solid Solutions

3.1. Synthesis strategy

In order to investigate the effect of adding $Ba_3CoNb_2O_9$ (BCN) and La_2CoTiO_6 (LCT) into BSCF of the perovskite structure (ABO_3), a range of BSCF-based materials was synthesised with their compositions listed in Table 3.1 and 3.2 below. The reference name of each composition used hereafter in this thesis is also listed.

Table 3.1. Summary of the information of the BCN-BSCF compositions studied and represented.

Doping percentage of BCN	Composition reference used	Materials Compositions				
		Ba	Sr	Co	Fe	Nb
5%	0.05BCN-0.95BSCF	0.568	0.432	0.736	0.173	0.091
10%	0.1BCN-0.9BSCF	0.625	0.375	0.683	0.15	0.167
50%	0. 5BCN-0. 5BSCF	0.875	0.125	0.45	0.05	0.5
90%	0.9BCN-0.1BSCF	0.98	0.02	0.35	0.01	0.64

Table 3.2. Summary of the information of the BCN-BSCF compositions studied and represented.

Doping percentage of LCT	Composition reference used	Materials Compositions					
		Ba	Sr	La	Co	Fe	Ti
5%	0.05LCT-0.95BSCF	0.452	0.452	0.096	0.771	0.181	0.0048
10%	0.1LCT-0.9BSCF	0.409	0.409	0.182	0.745	0.164	0.091
50%	0. 5LCT-0. 5BSCF	0.167	0.167	0.666	0.6	0.067	0.333
90%	0.9LCT-0.1BSCF	0.026	0.026	0.947	0.516	0.011	0.474

3.2. Powder Synthesis, Materials Preparation and Characterisation

3.2.1. Powder Synthesis and Crystal Phase Characterisation

BCN-BSCF and LCT-BSCF samples were prepared by solid state reaction using high purity $BaCO_3$ (99.997), $SrCO_3$ (99.994%), Co_3O_4 (99.9985%), Fe_2O_3 (99.998%), Nb_2O_5 (99.9985%), La_2O_3 (99.99%), and TiO_2 (99.9%). Stoichiometric mixture of these powders were mixed and ball-milled (350 rpm for overnight, Fritsch Pulverisette 7 Planetary Mill) in 2-propanol with ZrO_2 balls, and then heated to 800 °C for 8h before ball-milling again. The resulting powders were then pressed as pellets (1.3 cm diameter) and sintered at various synthesis temperatures for 12hours depending on the doping level of $Ba_3CoNb_2O_9$ (BCN) and La_2CoTiO_6 (LCT). After this, the powders were crushed and hand-ground in acetone, before re-pelletised and re-fired for another 12hours. Heating and cooling rate of 5°C/min were used throughout the process. The so-made cathode materials are called "as made cathode powder". A schematic figure showing the synthesis steps is shown in Figure 3.1 and different firing temperatures of different compositions are listed in Table 3.3. The "as made cathode powders" were again ball-milled at 350rpm for overnight in 2-propanol with ZrO_2 balls. These are called "milled cathode powder".

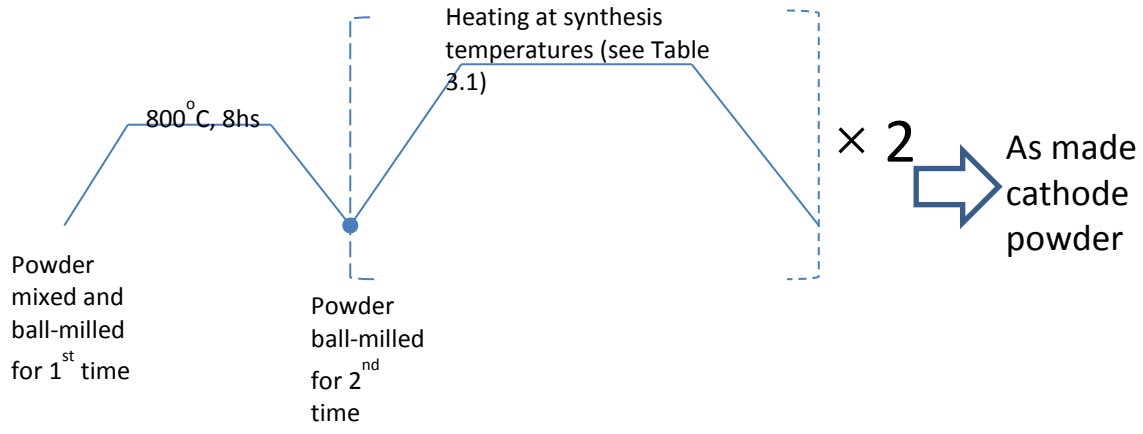

Fig 3.1. Schematic illustration of steps for the synthesis of the BCN-BSCF and LCT-BSCF powders.

Table 3.3. Different synthesis temperatures of different doped BCN-BSCF and LCT-BSCF

Materials reference	**0.05-0.1BCN-BSCF**	**0.5BCN-0.5BSCF**	**0.9BCN-0.1BSCF**	**0.05-0.1LCT-BSCF**	**0.5LCT-0.5BSCF**	**0.9LCT-0.1BSCF**
Firing temperature	1100^{o}C	1150^{o}C	1200^{o}C	1100^{o}C	1200^{o}C	1250^{o}C

In this study, phase purity was determined using X-ray powder diffraction (Panalytical X-pert Pro Bragg-Brentano geometry laboratory X-ray diffractometer with Co $K\alpha_1$ radiation = 1.78901Å).

3.2.2. Materials Preparation and Characterisation

3.2.2.1. Long Term Stability and Compatibility Experiments

Three sets of stability test for cathode materials were carried out in this study, these being thermal stability test, electrolyte compatibility test and CO_2 tolerance test. These tests were carried out in order to determine how the phase changes under these conditions and were performed on "milled cathode powder" as prepared in Section 3.2.1.

Thermal stability tests were carried out by putting the "milled cathode powder" annealing at 750^{o}C for 5 days in static air to simulate IT-SOFC operating temperatures.

The CO_2 stability tests can indicate if a phase is likely to react with CO_2 in the atmosphere and decompose over long timescales. "Milled cathode powder" were annealed in a tube furnace at 750^{o}C under atmosphere of 1%CO_2/99%Ar.

Chemical compatibility between a cathode and an electrolyte material is important for SOFCs as these components are in contact in the device. Reactivity between the two components under operating conditions must be determined as reaction could lead to phase decomposition or new phase formation that may be detrimental to performance. In this thesis, chemical compatibility tests were carried out between the "milled cathode materials" and state-of-art electrolytes $Ce_{0.8}Sm_{0.2}O_{1.9}$ (SDC, Fuel Cell Materials) powder. Cathode and electrolyte powders were mixed in a weight ratio 1:1 by hand grinding, and annealed at 950^{o}C for 3 hours to simulate

temperatures required to get a cathode ink to adhere to an electrolyte substrate as required for measurement of the electrochemical properties (see Section 3.2.2.5).

After these stability tests, post annealed samples were hand ground and analysed by laboratory PXRD in order to determine if decomposition/reaction had occurred, or to evaluate if lattice parameters varied significantly, indicating the level of stability as a potential cathode material.

3.2.2.2. Preparation of Dense Pellet

To obtain dense pellets for electrical characterisation, "milled cathode materials" were first pressed in a uniaxial steel die and then isostatically pressed (Autoclave Engineers Cold Isostatic Press) at 200 MPa, followed by sintering at 1200-1400^{o}C for 12 hours depending on the composition. All as-prepared pellets have high relative density (> 95%) as measured by the Archimedes method and compared to that expected from the theoretical X-ray density. The sintering temperatures of each component to obtain the dense pellet are listed in Table 3.4.

Table 3.4. Different sintering temperatures of different doped BCN-BSCF and LCT-BSCF in order to obtain the dense pellet.

Materials reference	**0.05-0.1BCN-BSCF**	**0.5BCN-0.5BSCF**	**0.9BCN-0.1BSCF**	**0.05-0.1LCT-BSCF**	**0.5LCT-0.5BSCF**	**0.9LCT-0.1BSCF**
Firing temperature	1200^{o}C	1300^{o}C	1400^{o}C	1200^{o}C	1300^{o}C	1400^{o}C

3.2.2.3. Four Probe DC Conductivity Measurements

The electrical conductivity was measured with a standard dc four-probe method at the temperature range 500^{o}C-700^{o}C in 50° steps in air. The samples have a rectangular geometry and gold wire was attached to it with gold paste to make the I-V probes with four-in-a-line contact geometry. As discussed in Section 3.2.2.2, a dense pellet was first prepared and then cut into rectangular bars. The dense pellets had diameter of 13mm, determining the maximum length of the bar, and thickness approximately 1mm, which controls the cross-section area of the bar. The dimensions of the bars were measured with a calliper and recorded. The current

was provided by a Keithley 220 current source and the voltage was measured by a Keithley 2182 nanovoltmeter. An illustration of the arrangement of the sample is shown in Figure 3.2.

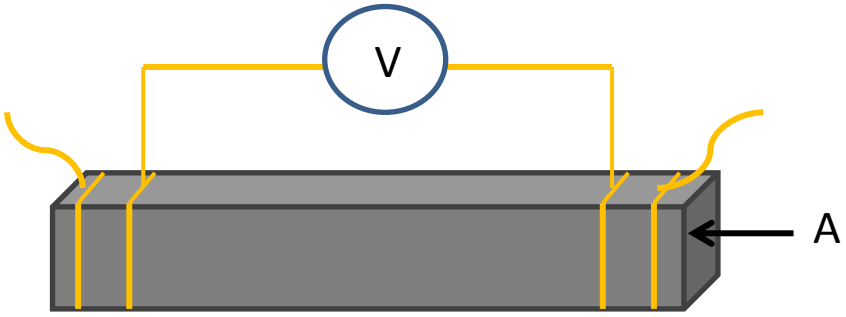

Fig 3.2. Schematic illustration of the arrangement of a 4-probe DC measuring sample.

3.2.2.4. Thermogravimetric Analysis (TGA)

In this work, the weight change of BCN-BSCF and LCT-BSCF as a function of temperature was examined in order to obtain information regarding the oxygen content of the material. The experiments were carried out using a TA Instruments SDT-Q600 Thermo Gravimetric Analyser (TGA) under following air (flow rate: 50 mL/min) from room temperature to 750^{o}C with a heating and cooling rate of 5 $^{\circ}$C/min. The process was repeated for 3 times with a dwell at the maximum temperature and minimum temperatures of 30 minutes on each cycle.

3.2.2.5. Electrochemical Measurements

AC impedance measurements were performed on samples in the "symmetric cell" configuration, which consists of porous cathode coating on both sides of a dense electrolyte substrate, as illustrated in Fig 3.3.

The state-of-art electrolyte material used for both BCN-BSCF and LCT-BSCF was commercially available $Ce_{0.8}Sm_{0.2}O_{1.9}$ (SDC) powder purchased from Fuel Cell Materials. Electrolyte substrate were prepared by pressing approximately 0.8g SDC powders in a uniaxial press of 10mm, followed by sintering at 1400^{o}C for 12hs, resulting in greater than 95% theoretical density as measured by Archimedean balance.

For the preparation of the porous cathode coating, the "milled cathode materials" as prepared in Section 3.2.1 were further ball-milling with the pore-former, V-006 (Heraeus Electronic Materials) for 3hours with mass ratio between cathode materials and the pore-former, 1:0.7.

The suspension was then screen printed onto SDC substrate on both sides using an AccuCoat Screen Printer (model 3230) from Aremco, and dried in an oven at 100°C between each coating; this was repeated 6 times for each side. The cell was then fired to 950 °C for 3h (heating rate 1°C/min), and then coated with Au paste, followed by heating to 600 °C for 1 hour to ensure bonding to the cathode surface. ASR measurements were then performed in static air by AC impedance spectroscopy (Metrohm Autolab AUT84515) in the frequency range from 0.1 to 10^5 Hz with perturbation of 10 mV. The impedance data were analysed using *ZView* software.[61]

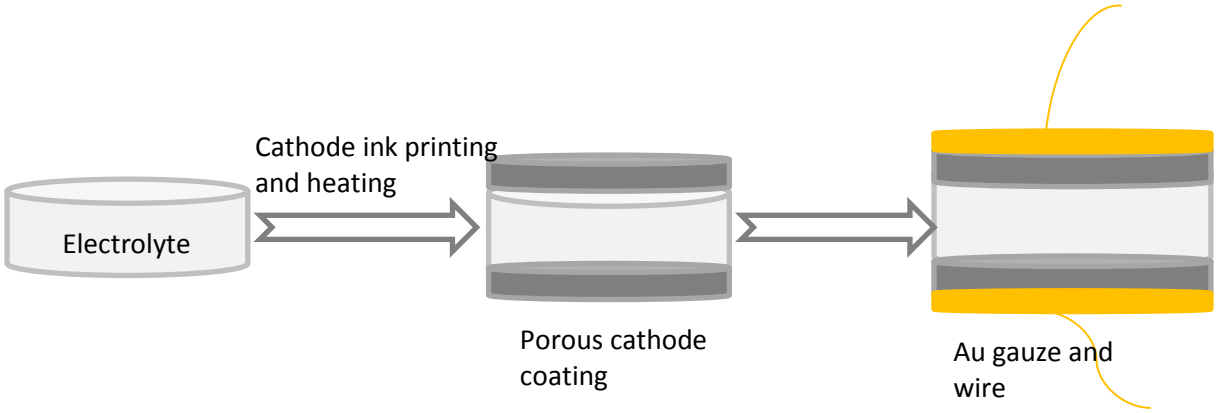

Fig 3.3. Schematic illustration of the preparation of BCN-BSCF and LCT-BSCF specimens in the symmetric cell configuration for AC impedance measurements

3.3. Crystal Structure Characterisation

3.3.1. BCN-BSCF

The parent un-doped BSCF material was confirmed as phase pure from Pawley fit against XRD data collected at room temperature (Fig 3.4), crystallising in *Pm-3m* with lattice parameter 3.98076(10)Å, which is in good agreement with previous report for BSCF (3.9830Å). [62]

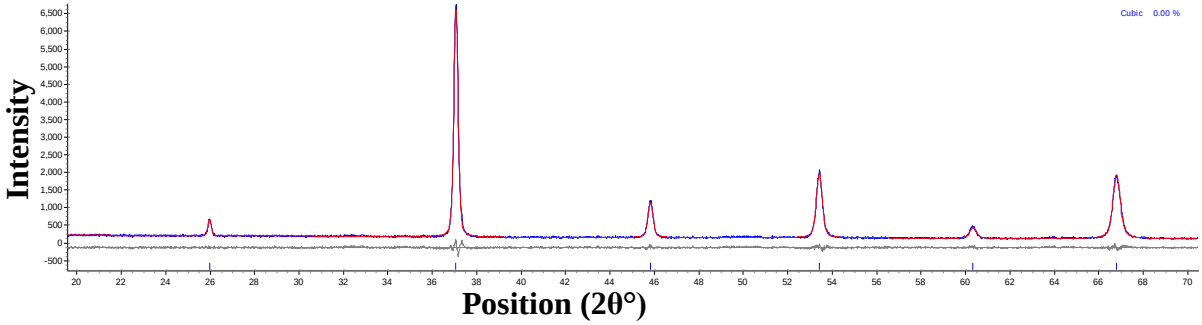

Fig 3.4. Pawley refinement (red line) of XRD data (2θ=20°-70°) for BSCF powders (blue line) sintered using cubic perovskite structure model (Pm-3m). Grey line represents the difference between calculated and measured data, with the black tick marks showing the allowed reflections.

The effect on the PXRD patterns of $Ba_3CoNb_2O_9$ (BCN) doping in the perovskite structure of BSCF is displayed in Figure 3.5. Pawley fitting of these materials are also shown in Figures 3.6-3.9. X'pert Highscore was used in this thesis to help identify the structure formed in the materials, using the Search/match function.

No extra reflections of the 0.05BCN-0.95BSCF doped composition was observed throughout the 2θ angle scanned indicating that the small amount of BCN doping into BSCF favours the formation of an isostructural compound with the un-doped single perovskite (SP) material. However, it is clear that there is a shift in reflection positions to lower 2θ angles by carefully examining Figure 3.5. This indicates an increase in lattice parameters and Pawley fitting of the XRD data of this sample (*Figure 3.6*) confirming that 0.05BCN-0.95BSCF crystallises in the same space group as the parent undoped material, with lattice parameters of 4.01899(4) Å (*Table 3.3*).

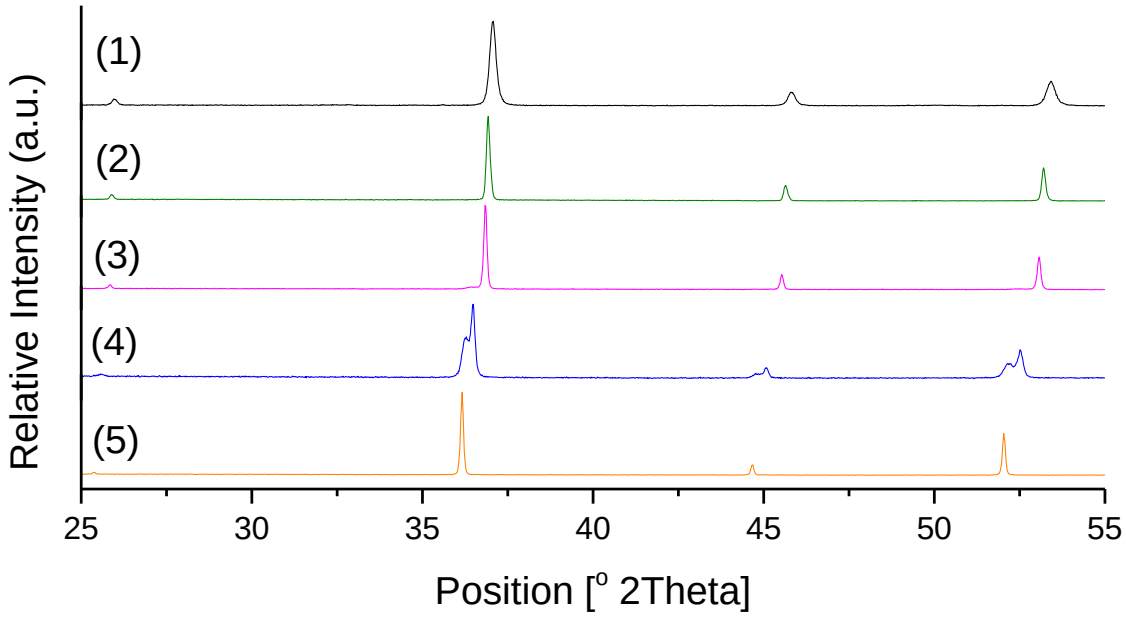

Fig 3.5. Laboratory PXRD patterns showing (1), BSCF; (2), 0.05BCN-0.95BSCF; (3), 0.1BCN-0.9BSCF; (4), 0.5BCN-0.5BSCF and (5), 0.9BCN-0.1BSCF doped compositions. To examine the main peak more clearly, only 2θ=25°-55° are shown here.

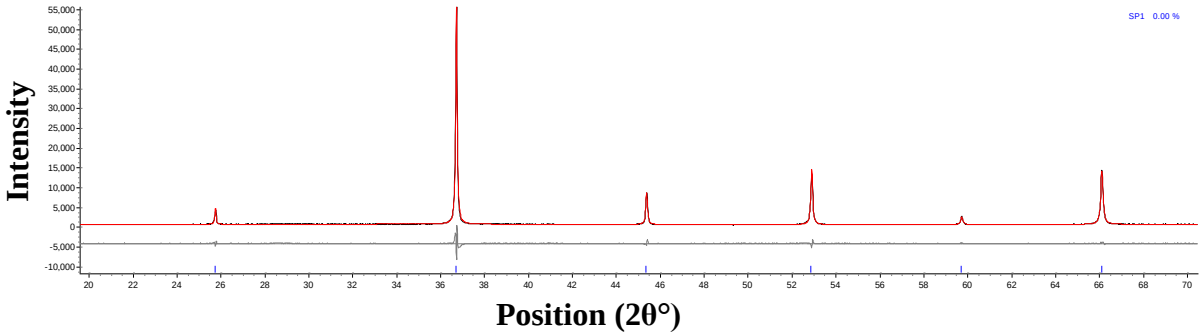

Fig 3.6. Pawley refinement (red line) of XRD data (2θ=20°-70°) for 0.05BCN-0.95BSCF powders (blue line) using cubic perovskite structure (Pm-3m). Grey line represents the difference between calculated and measured data, with the black tick marks showing the allowed reflections.

A slightly higher BCN (10%) containing BSCF resulted in a slightly asymmetric peak shape with every perovskite peak after careful examination of the XRD pattern. However, no extra reflection was observed even after a high resolution synchrotron experiment. One possible explanation could be the formation of phases with very close reflection positions, such as a second SP phase with very small difference in lattice parameters giving overlapping reflections, which is also agree with what X'pert Highscore suggested by using phase search/match

function as described in Section 2.2.7. Two different models were tested by Pawley fitting to the PXRD pattern, (i), a single phase cubic perovskite with the same space group as the parent BSCF material, and (2), two cubic perovskites with the same space group and very similar lattice parameters. Two cubic perovskites model with very close lattice parameters fitted the peaks better than the one cubic perovskite model (fitting with the reflection corresponding to (0 11) Miller indices by two different structure models shown in Figure 3.7(a) and (b)) which is confirmed by the superior agreement factors R_{wp} and χ^2 (Table 3.3).

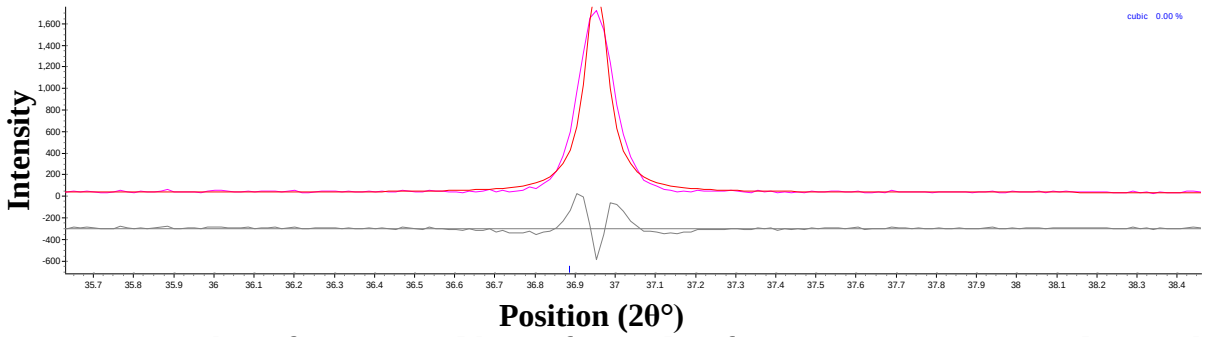

Fig 3.7(a). Pawley refinement (red line) of XRD data for 0.1BCN-0.9BSCF powders (pink line) using one cubic perovskite structure model (Pm-3m). Grey line represents the difference between calculated and measured data, with the black tick marks showing the allowed reflections.

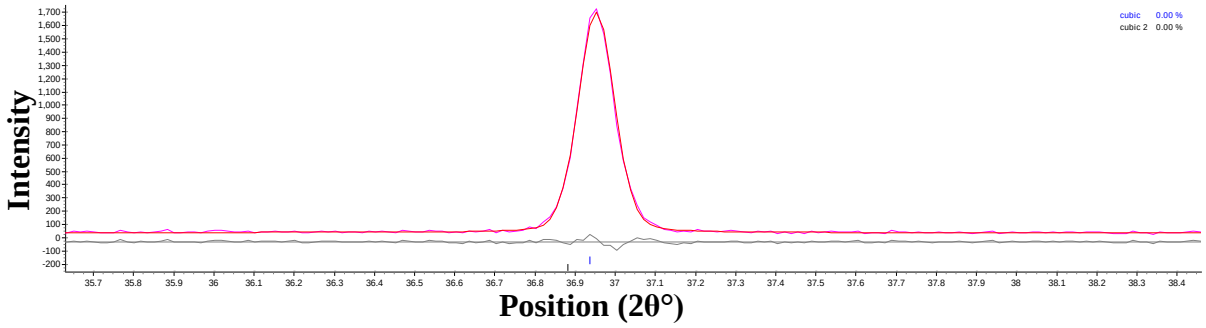

Fig 3.7(b). Pawley refinement (red line) of XRD data for 0.1BCN-0.9BSCF powders (pink line) using two cubic perovskites structure model (both Pm-3m). Grey line represents the difference between calculated and measured data, with the black tick marks showing the allowed reflections.

Adding 50% of $Ba_3CoNb_2O_9$ (BCN) into BSCF made the XRD of the material produce an extra peak overlapping with every single perovskite peak as shown in Figure 3.5 compared with un-doped BSCF. This could be the splitting of the peaks which could be an indication of the formation of lower symmetry structures, due to distortion of the ideal cubic unit cell. Other

possible explanations for the splitting of the reflections could be the formation of phases with very close reflection positions, such as a second SP phase with very small difference in lattice parameters giving overlapping reflections. A two cubic perovskite structure model was used to fit the observed data based on two reasons: (1) there are no other reflections other than perovskite peaks; (2) there are extra peaks accompany every perovskite peak; and (3) the structure of 10%BCN doped composition was fitted well by two cubic perovskites. The fitting curve and resulting agreement factors are shown in Figure 3.8 and Table 3.3 respectively, indicating good fitting with the two-cubic-perovskite model.

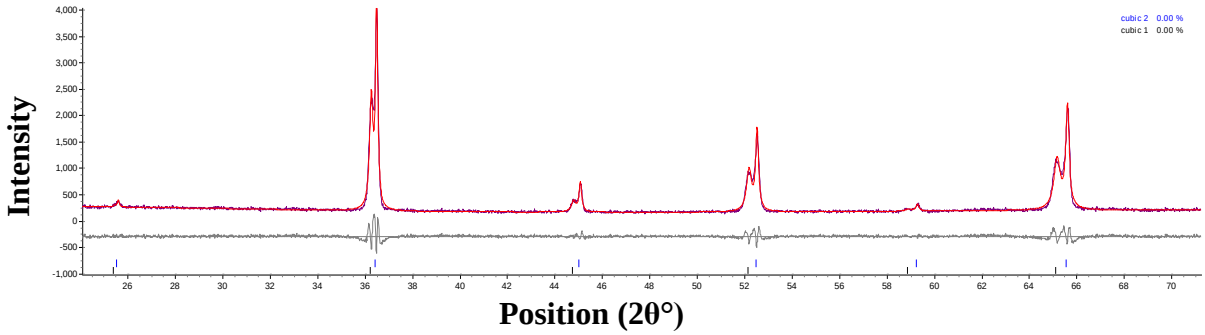

Fig 3.8. Pawley refinement (red line) of XRD data (2θ=20°-70°) for 0.5BCN-0.5BSCF powders (purple line) using two cubic perovskite model (Pm-3m). Grey line represents the difference between calculated and measured data, with the black tick marks showing the allowed reflections.

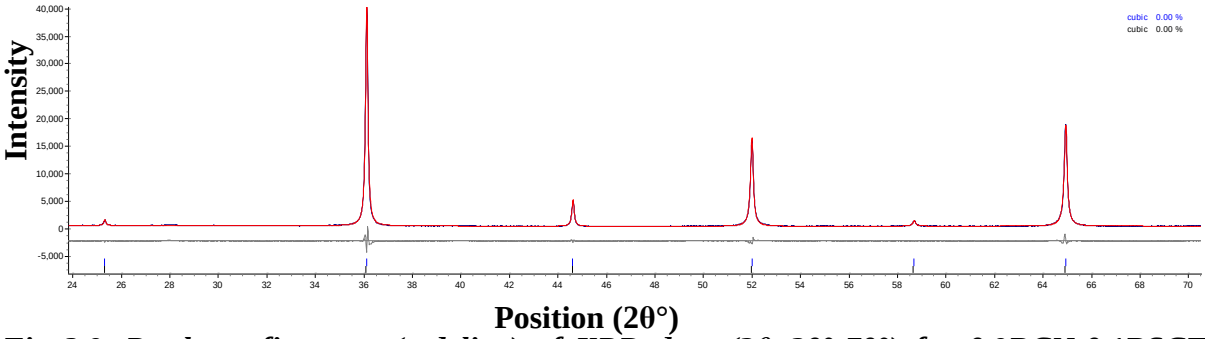

Fig 3.9. Pawley refinement (red line) of XRD data (2θ=20°-70°) for 0.9BCN-0.1BSCF powders (blue line) using cubic perovskite model (Pm-3m). Grey line represents the difference between calculated and measured data, with the black tick marks showing the allowed reflections.

A careful examination of 90%BCN doped composition again revealed no extra reflections throughout the 2θ angle scanned suggesting the formation of an isostructural compound with the un-doped single perovskite (SP) material. The shift in reflection positions to higher 2θ angles suggested the biggest increase of lattice parameter as confirmed by Pawley fitting shown

in Table 3.3 and Figure 3.9. A linear expansion of the lattice parameter was observed with increasing amount of $Ba_3CoNb_2O_9$ in the material.

Table 3.3. The refined lattice parameters and fitting statistics for Pawley fits of four different BCN-BSCF materials.

Materials reference	Structure model	Space group	R_{wp}/%	R_{exp}/%	χ^2	Lattice parameters a (Å)
0.05BCN-0.95BSCF	Cubic perovskite	*Pm-3m*	4.24	3.330	1.268	a=4.01899(4)
0.1BCN-0.9BSCF	Cubic perovskite	*Pm-3m*	8.157	3.974	2.053	a=4.03077(9)
	Cubic perovskite ×2	Pm-3m	5.465	3.967	1.378	a1=4.03043(6)
						a2=4.04485(44)
0.5BCN-0.5BSCF	Cubic perovskite ×2	*Pm-3m*	9.071	6.048	1.5	a1=4.04775(13)
						a2=4.07176(16)
0.9BCN-0.1BSCF	Cubic perovskite	*Pm-3m*	5.374	3.358	1.600	a=4.08192(4)

3.3.2. LCT-BSCF

The XRD patterns of the four different La_2CoTiO_6 (LCT) doped BSCF compositions are shown in Figures 3.10 to 3.14 respectively. As with 0.05BCN-0.95BSCF, 5%LCT doped BSCF (0.05LCT-0.95BSCF) afford a cubic perovskite phase crystallising in *Pm-3m*, as demonstrated by the Pawley fit, isostructural to the parent BSCF. The shift of the peaks to the higher 2θ angle indicated a decrease of the lattice parameter, with the refined value of 3.95891(1)Å for the 0.05LCT-0.95BSCF.

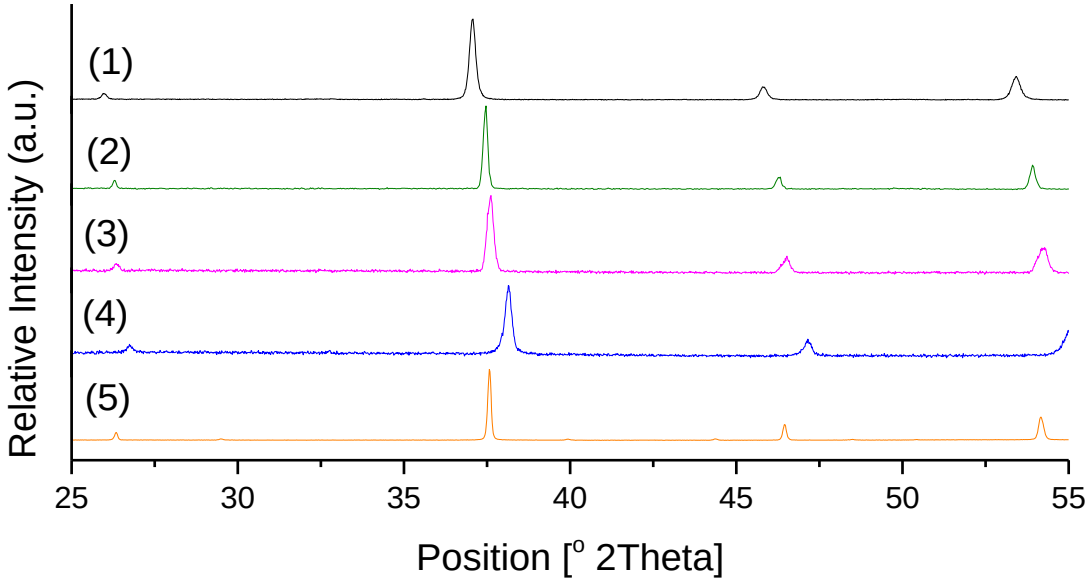

Fig 3.10. ***Laboratory PXRD patterns showing (1), BSCF; (2), 0.05LCT-0.95BSCF; (3), 0.1LCT-0.9BSCF; (4), 0.5LCT-0.5BSCF and (5), 0.9LCT-0.1BSCF doped compositions. To examine the main peak more clearly, only 2θ=25°-55° are shown here.***

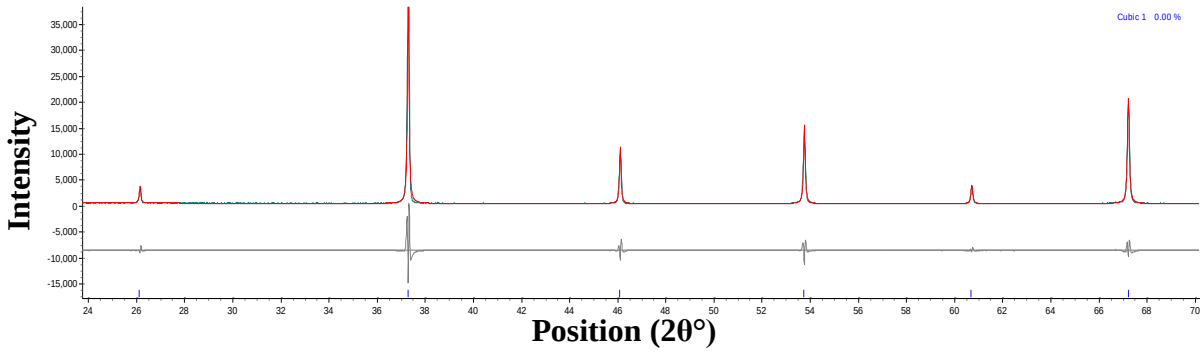

Fig 3.11. Pawley refinement (red line) of XRD data (2θ=20°-70°) for 0.05LCT-0.95BSCF powders (green line) using cubic perovskite model (Pm-3m). Grey line represents the difference between calculated and measured data, with the black tick marks showing the allowed reflections.

10%LCT (0.1LCT-0.9BSCF) doped composition showed slight peak broadening compared with 0.05LCT-0.95BSCF (Figure 3.10), which could also be the presence of a second cubic perovskite as in the case of 0.1BCN-0.9BSCF. Two structure models (1) One cubic perovskite and (2) two cubic perovskites were both tried to fit the PXRD data of this material with their fitting curves and quality of fitting shown in Figure 3.12 and Table 3.4. One cubic perovskite seems to be the preferred structure model based on two observations from fitting: (a) one cubic

perovskite fits well in terms of both peak intensity and shape (Figure 3.12(a)); (b) showings the fitting of Pawley fitting didn't manage to fit the second perovskite into the peak (Figure 3.12(b)). Moreover, the quality of fitting is very similar for both structure models (Table 3.4).

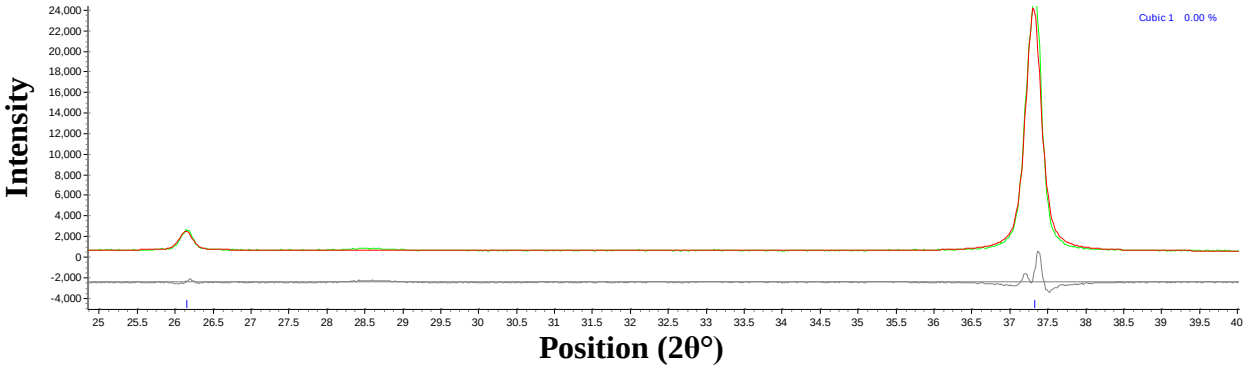

Fig 3.12(a). Pawley refinement (red line) of XRD data for 0.1LCT-0.9BSCF powders (green line) using one cubic perovskite model (Pm-3m). Grey line represents the difference between calculated and measured data, with the black tick marks showing the allowed reflections.

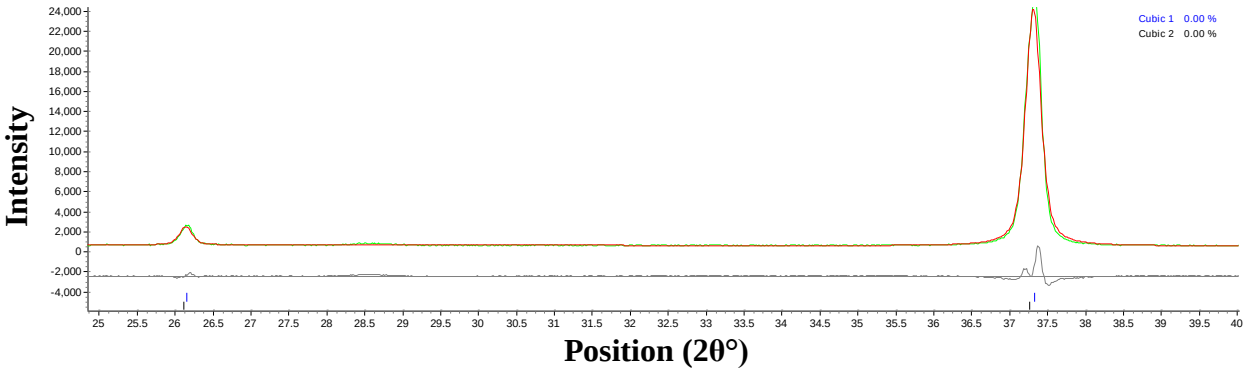

Fig 3.12(b). Pawley refinement (red line) of XRD data for 0.1LCT-0.9BSCF powders (green line) using two cubic perovskites model (Pm-3m). Grey line represents the difference between calculated and measured data, with the black tick marks showing the allowed reflections.

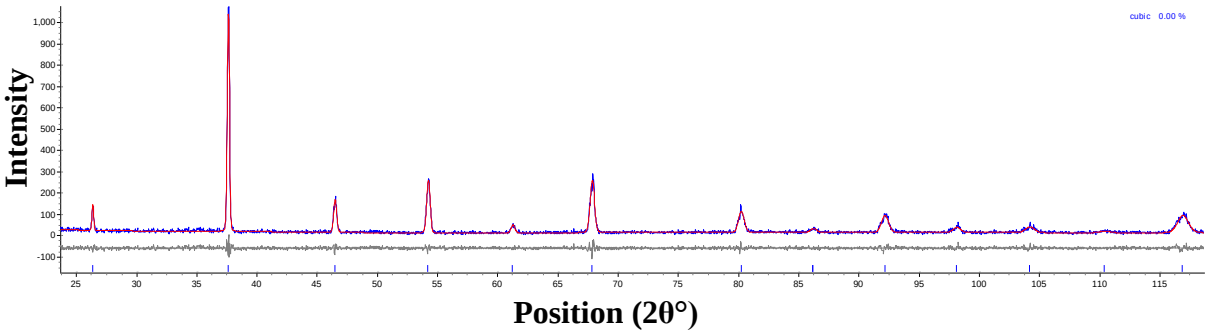

Fig 3.12(c). Pawley refinement (red line) of XRD data for 0.1LCT-0.9BSCF powders (blue line) using one cubic perovskite model (Pm-3m). Grey line represents the difference between calculated and measured data, with the black tick marks showing the allowed reflections.

When introducing more LCT, reaching 50%LCT (0.5LCT-0.5BSCF), peak broadening and asymmetry is even more obvious (Figure 3.10(4)). The XRD pattern was first indexed using X'pert Highscore search/match function, which suggested three possible structure solutions, (1). Two cubic perovskite structure (*Pm-3m*) with very similar lattice parameters, (2). A rhombohedral phase (*R-3c*) and (3). A tetragonal phase (*P4/mmm*). These three models together with the single cubic perovskite model were all tested by Pawley fitting and the resulting fits to the PXRD patterns are shown in Figure 3.13. The fitting curve of the main perovskite peak, (0 1 1) peak, and quality of Pawley fits obtained for 0.5LCT-0.5BSCF using the four different structural models are shown in *Table 3.4*. Two cubic perovskite structure model is slightly preferred than other three in terms of the fitting of peak shape (Figure 3.13(b)) and quality of fitting (Table 3.4).

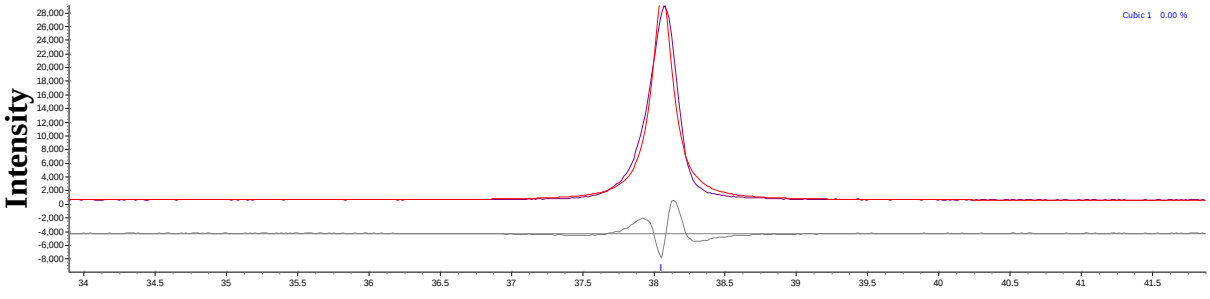

Fig 3.13(a). Pawley refinement (red line) of XRD data for 0.5LCT-0.5BSCF powders (purple line) using one cubic perovskite structural model (Pm-3m). Grey line represents the difference between calculated and measured data, with the black tick marks showing the allowed reflections.

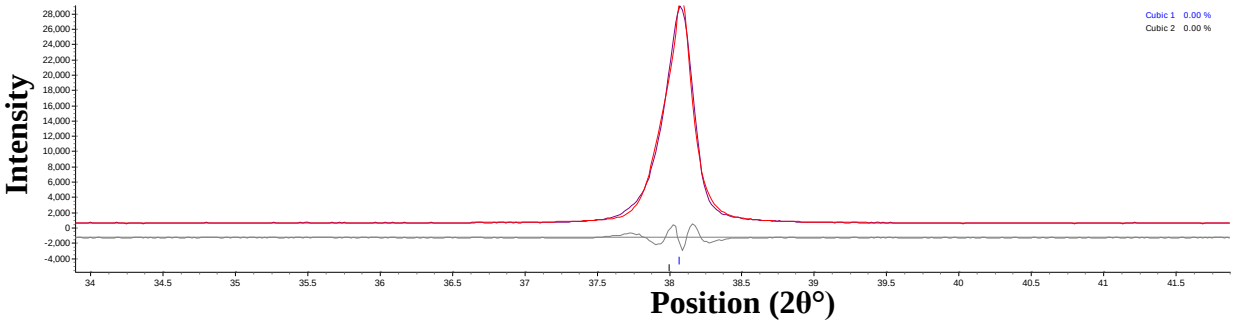

Fig 3.13(b). Pawley refinement (red line) of XRD data for 0.5LCT-0.5BSCF powders (purple line) using two cubic perovskites model (both Pm-3m). Grey line represents the difference between calculated and measured data, with the black tick marks showing the allowed reflections.

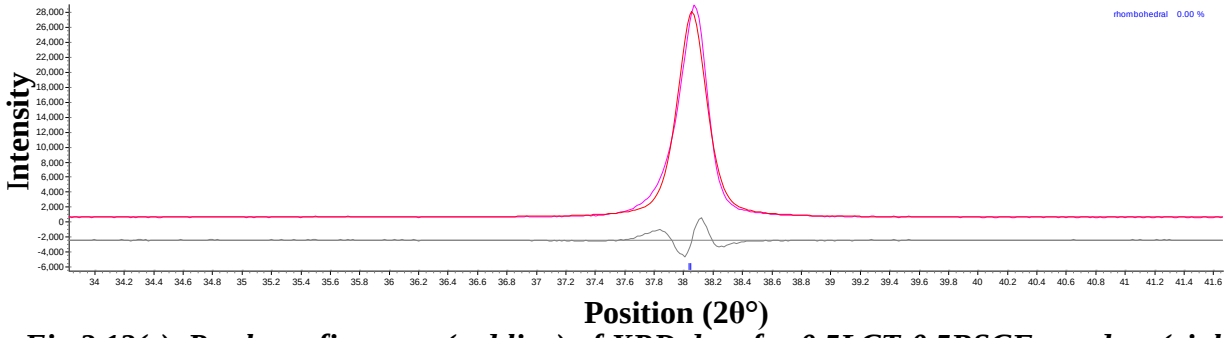

Fig 3.13(c). Pawley refinement (red line) of XRD data for 0.5LCT-0.5BSCF powders (pink line) using rhombohedral model (R-3c). Grey line represents the difference between calculated and measured data, with the black tick marks showing the allowed reflections.

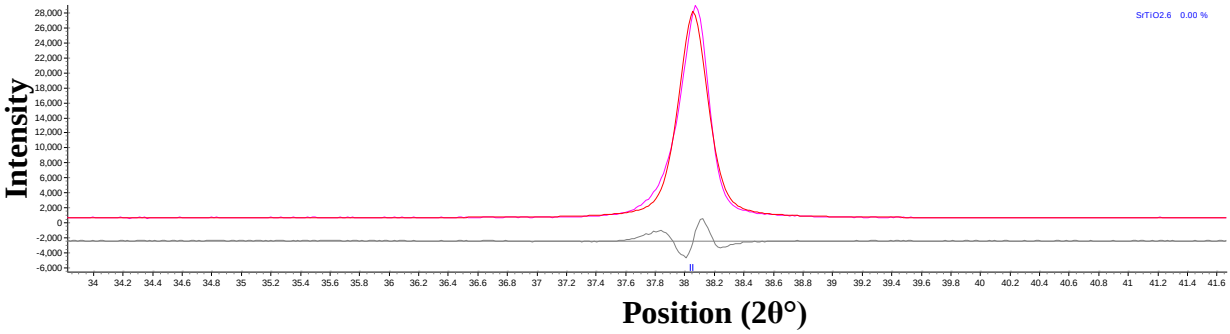

Fig 3.13(d). Pawley refinement (red line) of XRD data for 0.5LCT-0.5BSCF powders (pink line) using tetragonal model (P4/mmm). Grey line represents the difference between calculated and measured data, with the black tick marks showing the allowed reflections.

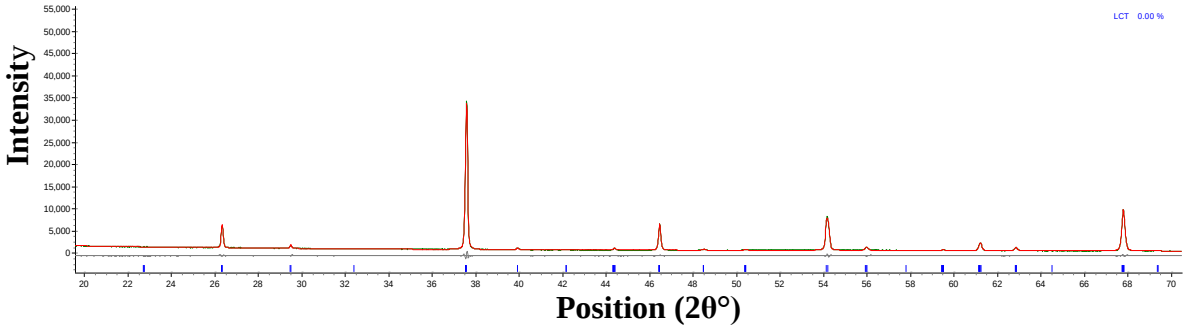

Fig 3.14. Pawley refinement (red line) of XRD data for 0.9LCT-0.1BSCF powders (blue line)using a monoclinic structural model ($P2_1/n$). Grey line represents the difference between calculated and measured data, with the black tick marks showing the allowed reflections.

When adding 90%La_2CoTiO_6 (LCT) into BSCF (0.9LCT-0.1BSCF), compared with un-doped BSCF, there are clearly additional reflection appeared in 0.9LCT-0.1BSCF at 2θ=29° and 40° (Figure 3.14). It is then reasonable to assume that the structure of this LCT-rich material possesses the same structure as the end member composition (LCT), which crystallises in a monoclinic symmetry $P2_1/n$. Both the fitting and the agreement factor indicated good agreement between this material and the structural model ($P2_1/n$).

Table 3.4. The refined lattice parameters and fitting qualities for Pawley fits of four different BSCF-BCN materials.

Material composition	**Structure model**	**Space group**	**R_{wp}/%**	**R_{exp}/%**	**χ^2**	**Lattice information (Å)**
0.05LCT-0.95BSCF	Cubic Perovskite	*Pm-3m*	10.672	3.819	2.794	a=b=c=3.95891(1)
0.1LCT-0.9BSCF	Cubic perovskite	*Pm-3m*	7.506	3.501	2.144	a=b=c=3.95202(4)
	Cubic perovskite ×2	*Pm-3m*	7.345	3.495	2.102	a1=b1=c1=3.93810(11)
						a2=b2=c2=3.95259(3)
0.5LCT-0.5BSCF	Cubic	*Pm-3m*	9.116	3.232	2.821	a=b=c=3.88047(6)
	Cubic perovskite ×2	*Pm-3m*	5.286	3.227	1.638	a1=b1=c1=3.87864(9)
						a2=b=c2=3.88553(24)
	Rhombohedral	*R-3c*	7.010	3.225	2.174	a=b=5.48928(105) c=13.44096(510)
	Tetragonal	*P4/mmm*	6.995	3.228	2.167	a=b=3.88179(31) c=3.87844(60)
0.9LCT-0.1BSCF	Monoclinic	$P2_1/n$	4.085	3.266	1.251	a=5.56182(52) b=5.56096(47) c=7.85366(21) β=90.03900(249)°

3.4. Long Term Stability and Compatibility

3.4.1. Long Term Stability and Compatibility of BSCF

The three long term stability tests (as described in Section 3.2.2.1) for commercial BSCF, 0.05BCN-0.95BSCF, 0.1BCN-0.9BSCF, 0.5BCN-0.5BSCF and 0.9BCN-0.1BSCF are shown and compared in Figure 3.15 to Figure 3.23. For each figure, plot (a) in black shows the as-made cathode materials, whilst plots (b), (c) and (d) corresponds to them after the stability tests. A comparison of their phases and the change of the lattice parameters before and after the stability tests were shown in Tables 3.5 to 3.7. In each figure, peaks corresponding to SDC are marked by *.

As shown in Figure 3.15(a), BSCF underwent serious decomposition after all three tests. The partial decomposition of the cubic to lower symmetry perovskite phases is evidenced by the broadening of the cubic peak and the addition of the extra peaks at 2θ=32°. Feldoff et al[4] have performed an investigation to the decomposition of BSCF.[4] Two different heating temperatures (700°C and 800°C) were used and slightly different decomposition products were formed. The Pawley fitting of the XRD, as shown in Figure 3.15(b) showed that the material after annealing at 750°C contained several products and was successfully fitted with four materials with their compositions and structures shown in Table 3.5. This is in good agreements with Feldhoff and other researchers. [20,62-66]

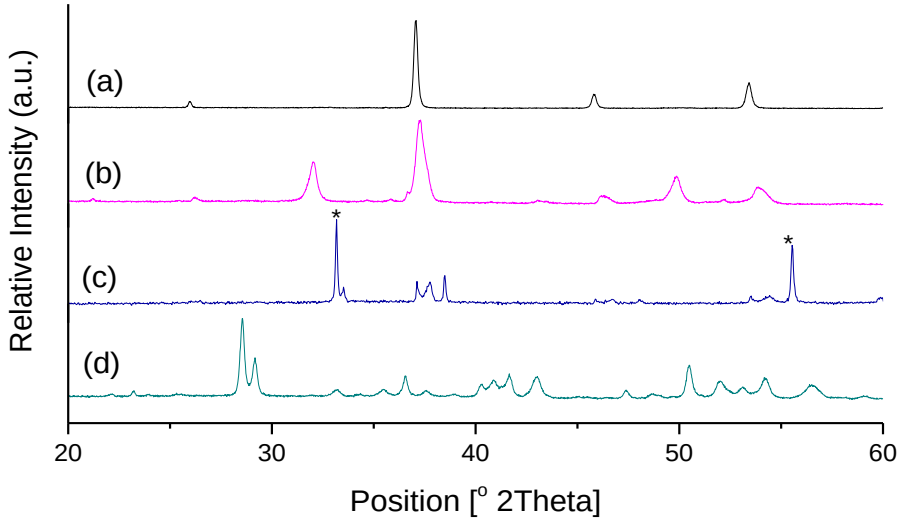

Fig 3.15(a). XRD of BSCF (a) before and (b). after thermal stability test at 750°C for 5 days in air, (c) after compatibility tests with SDC and (d) after CO_2 tolerance tests.

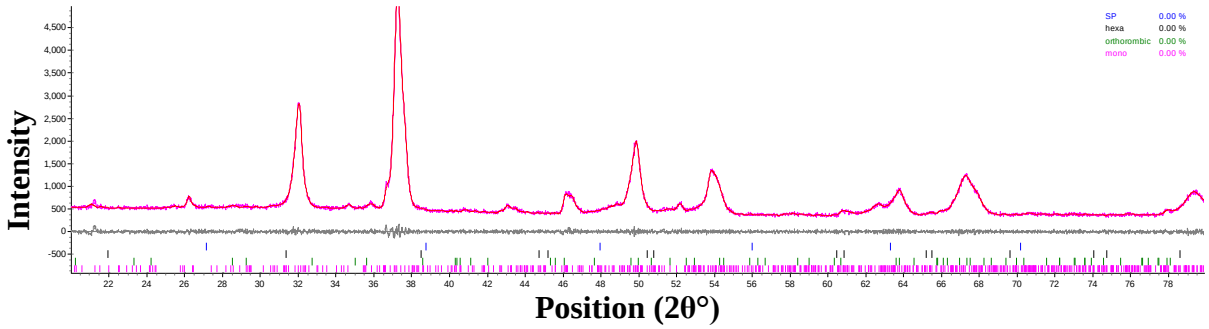

Fig 3.15(b). Pawley refinement (red line) of XRD data for commercial BSCF (pink line) after thermal stability test at 750ºC. Grey line represents the difference between calculated and measured data, with the black tick marks showing the allowed reflections. The XRD pattern was fitted by four structures as shown in Table 3.5.

The decomposition products for the SDC compatibility test and the CO_2 tolerance tests are mostly identified using X'pert Highscore search/match function and assessed by Pawley fitting the structural models with the XRD pattern (Figure 3.15(b), (c)). As summarised in Table 3.5, in both cases, commercial BSCF decomposed into multiple phases. In general, the three stability tests indicated that BSCF is very unstable under both the processing and operating conditions.

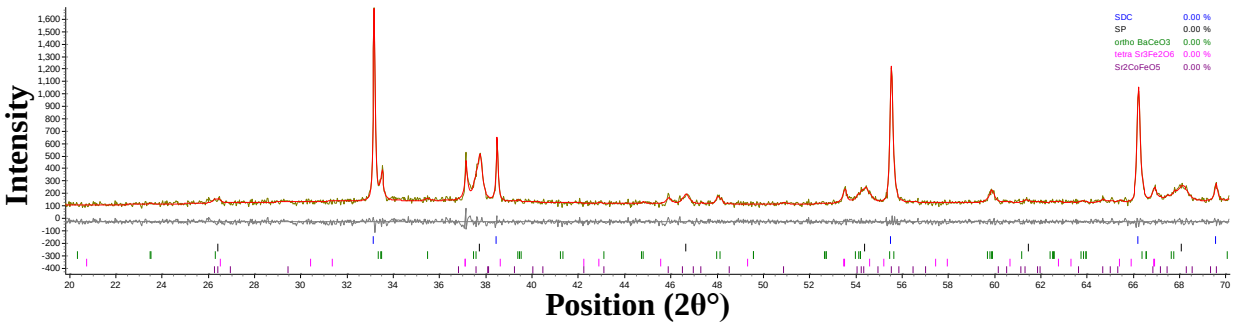

Fig 3.15(c). Pawley refinement (red line) of XRD data for commercial BSCF(blue line) after compatibility test with SDC at 950ºC. Grey line represents the difference between calculated and measured data, with the black tick marks showing the allowed reflections. The XRD pattern was fitted by five structures as shown in Table 3.5.

Table 3.5. Summary of the phases, and structures information of BSCF after three stability tests.

After thermal stability test		
Product after test	**Structure**	**space group ref.**
$(Ba_{0.5}Sr_{0.5})CO_3$	Orthorhombic (*Pmcn*)	De Villiers,[63] Kiseleva et al[64]
$(Ba_{0.25}Sr_{0.75})(Co_{0.6}Fe_{0.4})O_{3-\delta}$	Cubic (*Pm-3m*)	McIntosh et al[20]
$(Ba_{0.6-x}Sr_{0.4+x})(Co1_y\text{-}Fe_y)O_{3-\delta}$	Monoclinic (*P2/m*)	Feldhoff [62]
$(Ba_{0.75}Sr_{0.25})CoO_{3-\delta}$	Hexagonal (*P63/mmc*)	Gushee et al.[65] Taguchi et al[66]
After SDC compatibility test		
$BaCeO_3$	Orthorhombic (*Pbnm*)	
$Sr_3Fe_2O_6$	Tetragonal (*I4/mmm*)	
Sr_2CoFeO_5	Orthorhombic (*Ibmm*)	
$SrCoO_{2.29}$	Cubic (*Pm-3m*)	
SDC	Cubic (*Fm3m*)	
After CO_2 tolerance test		
$(Ba_{0.5}Sr_{0.5})CO_3$	Orthorhombic (*Pmcn*)	
Co_3O_4	Cubic (*Fd3m*)	
$BaCo_{1.88}Fe_{16.12}O_{27}$	Hexagonal (*P63/mmc*)	
$SrCO_3$	Orthorhombic (*Pnma*)	
SrO_2	Tetragonal (*I4/mmm*)	

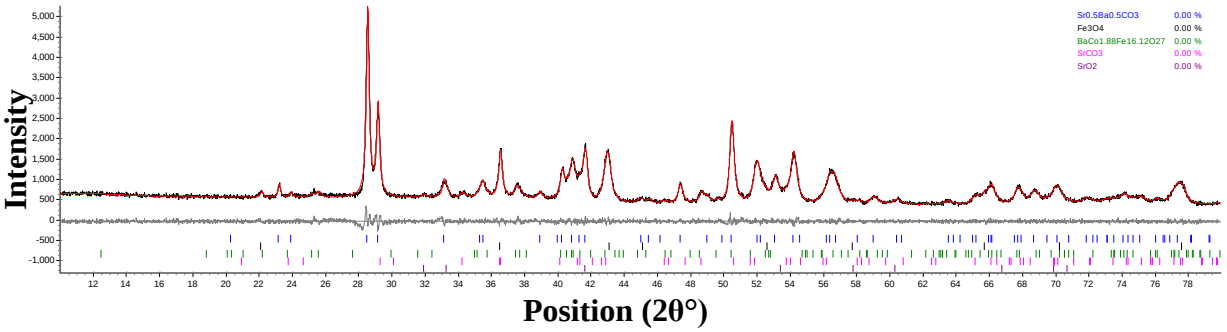

Fig 3.15(d). Pawley refinement (red line) of XRD data for commercial BSCF(black line) after compatibility test with CO_2. Grey line represents the difference between calculated and measured data, with the black tick marks showing the allowed reflections. The XRD pattern was fitted by five structures as shown in Table 3.5.

3.4.2. Long term stability and compatibility of BCN-BSCF

For 0.05BCN-0.95BSCF, there were minor new reflections, not related to the cubic perovskite phase, according to Figure 3.16(d) after annealing in 1%CO_2 atmosphere. The new reflections at 2θ=28°~30° were also identified as $Ba_{0.5}Sr_{0.5}CO_3$, as in the case of BSCF, but with significantly decreased peak intensity. Therefore the major phase present remained the cubic perovskite can indicated obviously by the intensity of the main perovskite. When combined with SDC at 950°C (Figure 3.16(c)), a new tetragonal phase appeared indicating reaction between electrolyte and 5%BCN doped cathode composition.

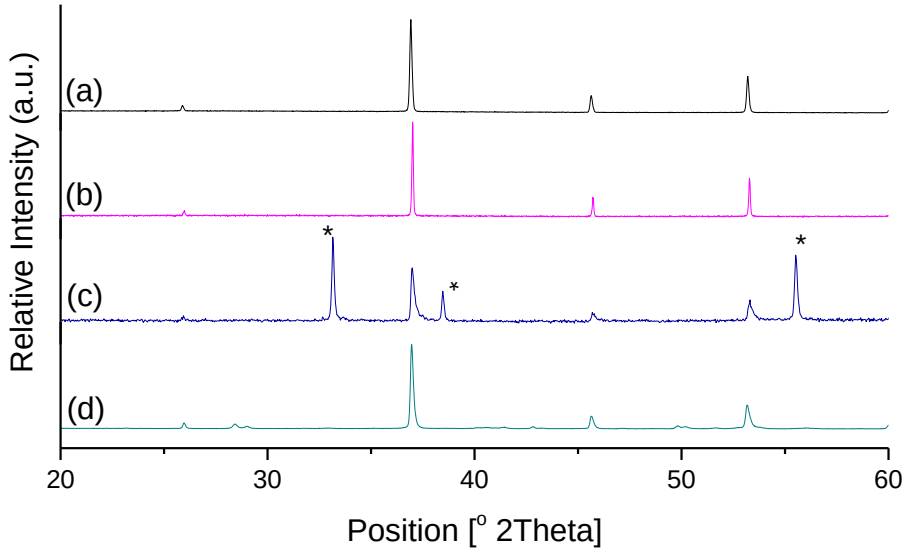

Fig 3.16, XRD of 0.05BCN-0.95BSCF (a) before and (b). after thermal stability test at 750°C for 5 days in air, (c) after compatibility tests with SDC and (d) after CO_2 tolerance tests.

Table 3.6(a). Summary of the phases, structures and lattice parameters (from Pawley fitting) of 0.05BCN-0.95BSCF after three stability tests.

After thermal stability test		
Product	**Structure**	**Lattice parameters(Å)**
Cubic	*Pm-3m*	a=b=c= 3.99735(8)
After SDC compatibility test		
Cubic	*Pm-3m*	a=b=c= 3.99383(21)
$Sr(Fe_{0.5}Nb_{0.5})O_3$	*P4mm*	a=b=3.98041(216) c=3.98846(342)
SDC	*Fm3m*	a=b=c=5.43538(23)
After CO_2 tolerance test		
Cubic	*Pm-3m*	a=b=c= 4.00736(16)
$Ba_{0.5}Sr_{0.5}CO_3$	*Pmcn*	a=5.28705(417) b=8.46939(242) c=6.39809(768)

0.1BCN-0.9BSCF cathode composition is stable with SDC after test at 950°C while extra peaks appeared after the other two stability tests with very low intensity peaks at 2θ~ 33° and 28°. The extra phases are hexagonal for the thermal stability test and $Ba_{0.5}Sr_{0.5}CO_3$ for the CO_2 tolerance test.

Table 3.6(b). Summary of the phases, structures and lattice parameters (from Pawley fitting) of 0.1BCN-0.9BSCF after three stability tests.

After thermal stability test		
Product	**Structure**	**Lattice parameters(Å)**
Cubic1	*Pm-3m*	a1=b1=c1= 4.00611(10)
Cubic 2	*Pm-3m*	a2=b2=c2=4.05599(133)
Hexagonal	*P63/mmc*	a=b=5.67664(221), c=13.27482(972)
After SDC compatibility test		
Cubic1	*Pm-3m*	a1=b1=c1=3.99956(85)
Cubic 2	*Pm-3m*	a2=b2=c2=4.00537(18)
SDC	*Fm3m*	a=b=c=5.43411(21)
After CO_2 tolerance test		
Cubic 1	*Pm-3m*	a1=b1=c1= 4.02127(8)
Cubic 2	*Pm-3m*	a2=b2=c2=4.06236(68)
$Ba_{0.5}Sr_{0.5}CO_3$	*Pmcn*	a=5.29452(315) b=8.49544(583) c=6.39893(353)

The stability of 0.5BCN-0.5BSCF and 0.9BCN-0.1BSCF materials after stability test were characterised by PXRD and it was observed that there was no new phase formation, as seen in Figures 3.18 and 3.19. However, in both materials, there was a shrinkage of the lattice parameters for the material after stability tests compared with the as made powders.

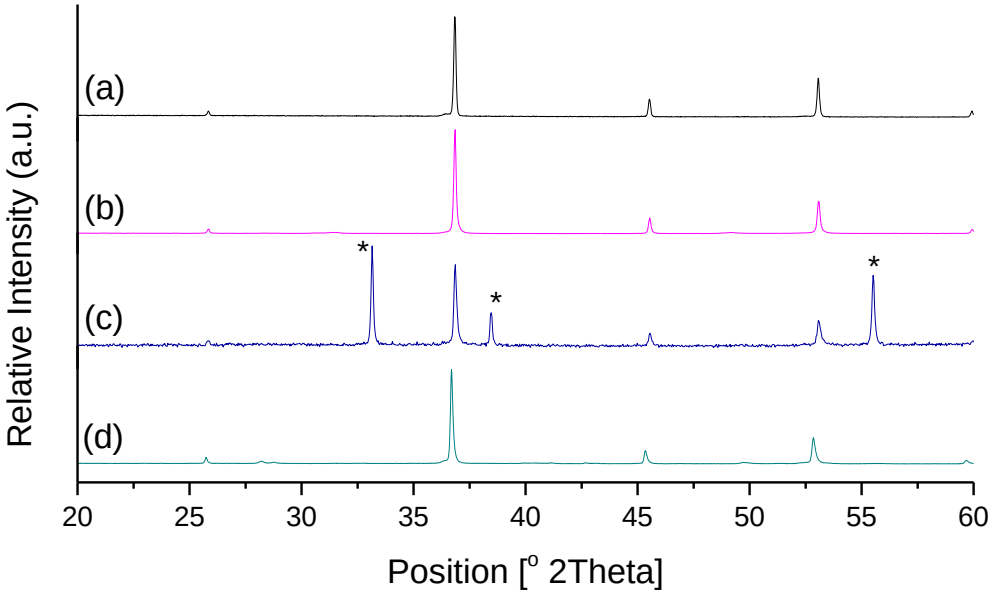

Fig 3.17, XRD of 0.1BCN-0.9BSCF (a) before and (b). after thermal stability test at 750°C for 5 days in air, (c) after compatibility tests with SDC and (d) after CO_2 tolerance tests.

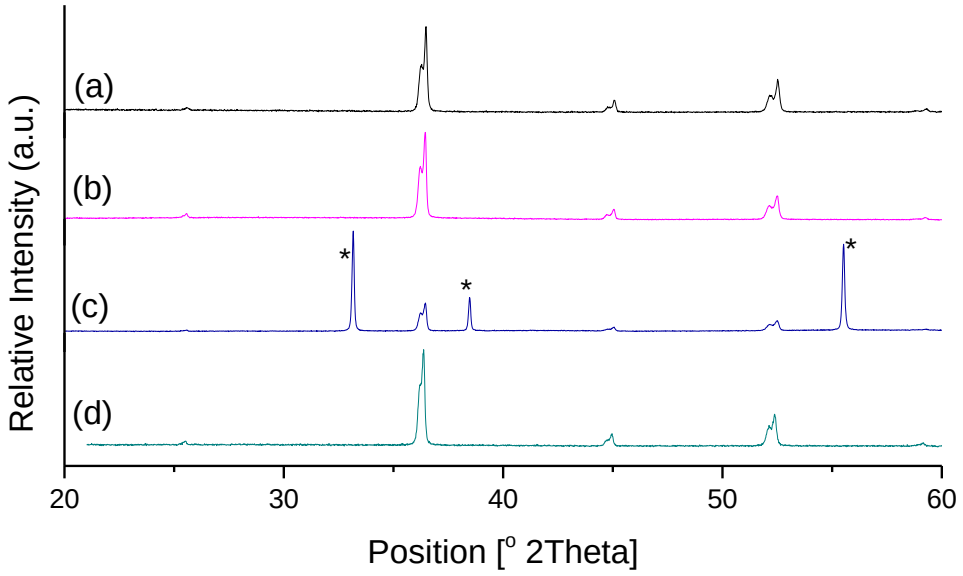

Fig 3.18, XRD of 0.5BCN-0.5BSCF (a) before and (b). after thermal stability test at 750°C for 5 days in air, (c) after compatibility tests with SDC and (d) after CO_2 tolerance tests.

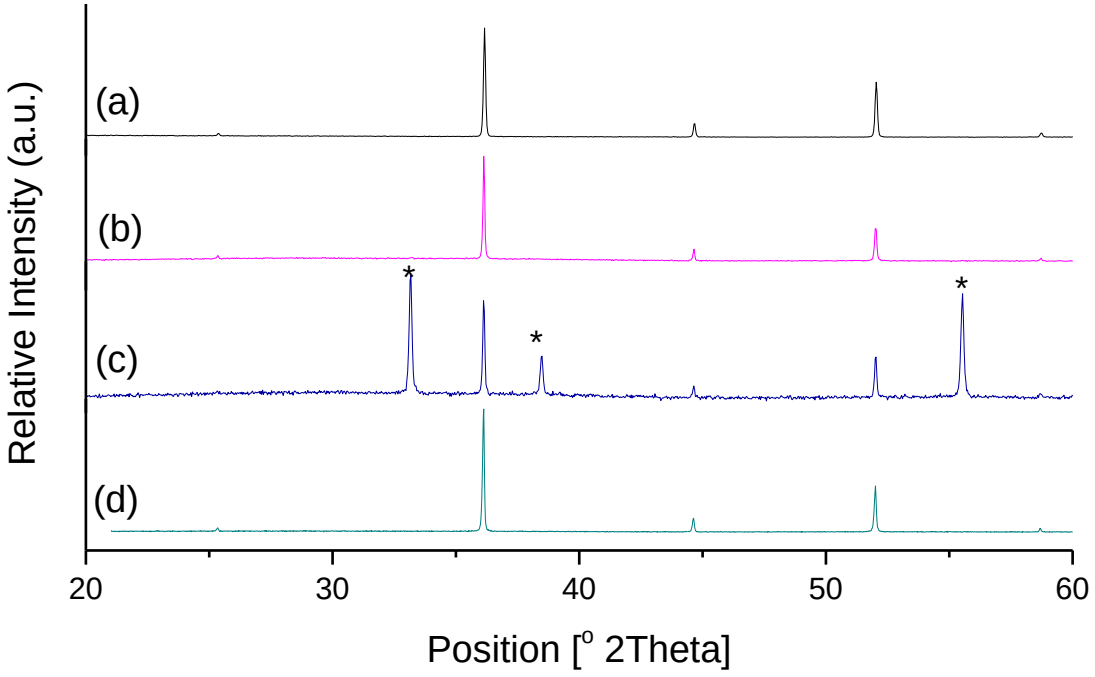

Fig 3.19, XRD of 0.9BCN-0.1BSCF (a) before and (b). after thermal stability test at 750°C for 5 days in air, (c) after compatibility tests with SDC and (d) after CO_2 tolerance tests.

Table 3.6(c). Summary of the products and their structure, lattice parameters from Pawley fitting of the three stability test of 0.5BCN-0.5BSCF and 0.9BCN-0.1BSCF compositions.

	0.5BCN-0.5BSCF	**0.9BCN-0.1BSCF**
Powders after thermal stability		
Structure	Cubic perovskite	Cubic perovskite
Lattice parameters	a1=b1=c1=4.04762(14) Å a2=b2=c2=4.07128(16) Å	a=b=c=4.08176(14)Å
Powder after SDC compatibility		
Structure	Cubic perovskite	Cubic perovskite
Lattice parameters	a1=b1=c1=4.04879(21) Å a2=b2=c3=4.07125(35) Å	a=b=c=4.08149(17)Å
Powder after CO2 tolerance tests		
Structure	Cubic perovskite	Cubic perovskite
Lattice parameters	a1=b1==c1=4.05253(36) Å a2=b2=c2=4.07069(37) Å	a=b=c=4.08116(10)Å

3.4.3. Long term stability and compatibility of LCT-BSCF

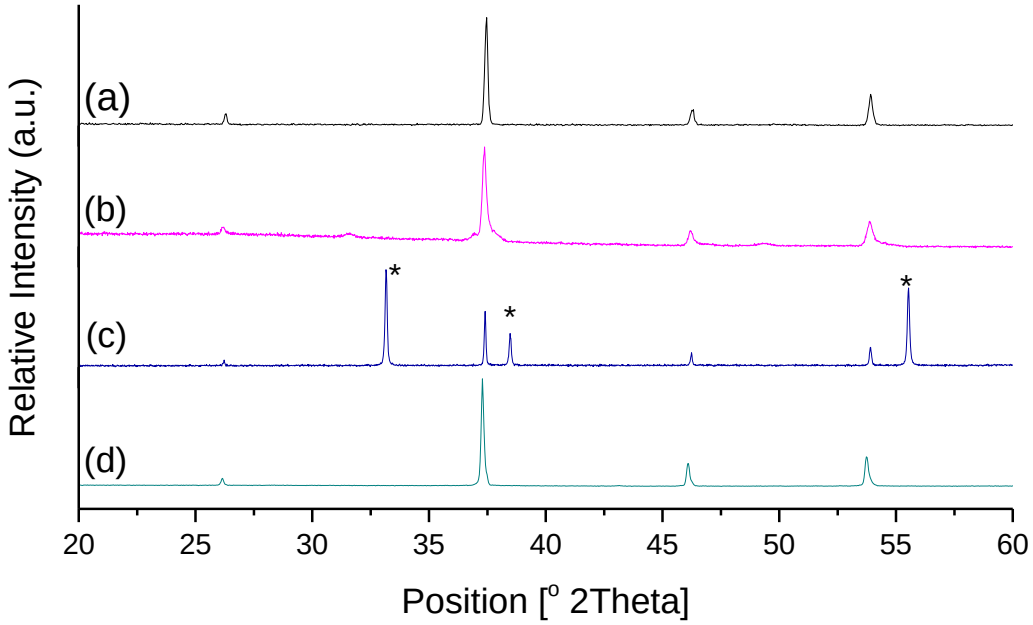

Fig 3.20, XRD of 0.05LCT-0.95BSCF (a) before and (b). after thermal stability test at 750°C for 5 days in air, (c) after compatibility tests with SDC and (d) after CO_2 tolerance tests.

The long term stability of 4 different LCT-BSCF compositions are shown and compared in Figure 3.20 to 3.23 respectively and the comparison of their lattice parameters are shown in Table 3.7(a)-(c). Plot (a) in black shows the as made LCT-BSCF material, whilst plots (b), (c) and (d) corresponds to them after the stability tests.

Extra peaks appeared for 0.05LCT-0.95BSCF material after annealing in static air for 5 days after carefully examining the XRD pattern. Using Pawley fitting, the extra peaks were fitted to a tetragonal phase by X'pert Highscore. However, no other phases appeared with the SDC compatibility test and CO_2 tolerance test for the cathode material containing 5%LCT.

0.1LCT-0.9BSCF materials however is stable after both the thermal stability test and SDC compatibility test, while it undergoes some decomposition after CO_2 tolerance test as shown in Figure 3.21(d). Fitting of the XRD pattern showed that the decomposition products are the main cubic perovskite together with three other components, they being: barium/strontium carbonates ($Ba_{0.5}Sr_{0.5}CO_3$), $(La_{0.4}Sr_{0.6})FeO_3$ and Co_3O_4.

Table 3.7(a). Summary of the products and their structure, lattice parameters from Pawley fitting of the three stability test of 0.05LCT-0.95BSCF doped composition.

After thermal stability test		
Product	**Structure**	**Lattice parameters(Å)**
Cubic	*Pm-3m*	a=b=c= 3.91901(38)
Tetragonal	*P4/mmm*	a=b=3.86881(1368), c=40.63024(2362)
After SDC compatibility test		
Cubic	*Pm-3m*	a=b=c=3.94855(7))
SDC	*Fm3m*	a=b=c=5.44378(74)
After CO_2 tolerance test		
Cubic 1	*Pm-3m*	a=b=c= 3.96068(3)

Table 3.7(b). Summary of the products and their structure, lattice parameters from Pawley fitting of the three stability test of 0.1LCT-0.9BSCF doped composition.

After thermal stability test		
Product	**Structure**	**Lattice parameters(Å)**
Cubic	*Pm-3m*	a=b=c= 3.91901(38)
After SDC compatibility test		
Cubic	*Pm-3m*	a=b=c=3.92425(24)
SDC	*Fm3m*	a=b=c=5.43438(29)
After CO_2 tolerance test		
Cubic 1	*Pm-3m*	a=b=c= 3.93907(30)
$(La_{0.4}Sr_{0.6})FeO_3$,	*R-3c*	a=b=5.52868(439) c=13.49174(1893)
$Ba_{0.5}Sr_{0.5}CO_3$	*Pmcn*	a=5.22257(78) b=8.68418(156) c=6.31770(141)
Co_3O_4	*Fd3m*	a=b=c=8.07531(104)

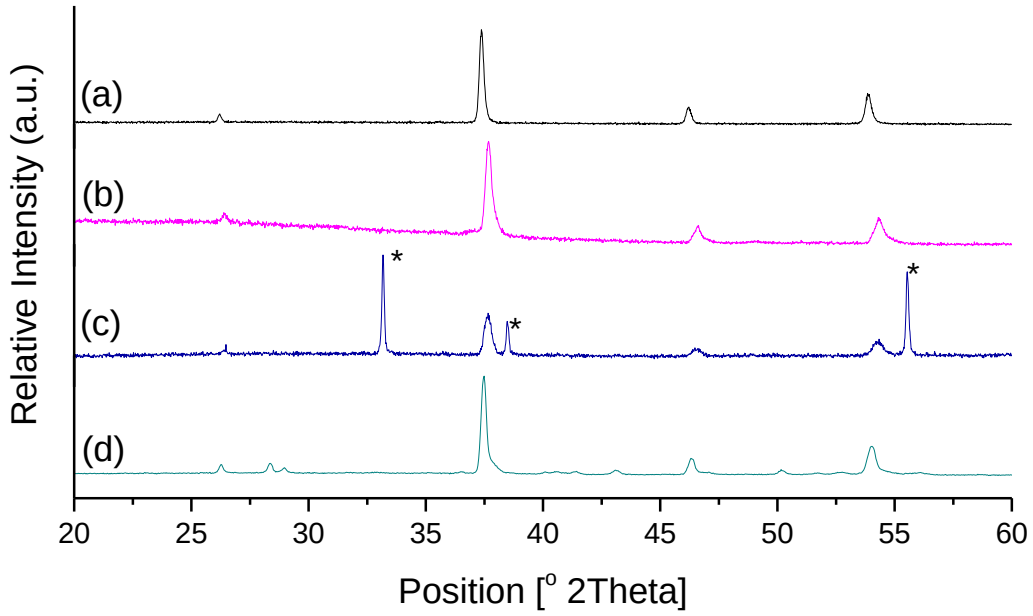

Fig 3.21, XRD of 0.1LCT-0.9BSCF (a) before and (b). after thermal stability test at 750°C for 5 days in air, (c) after compatibility tests with SDC and (d) after CO_2 tolerance tests.

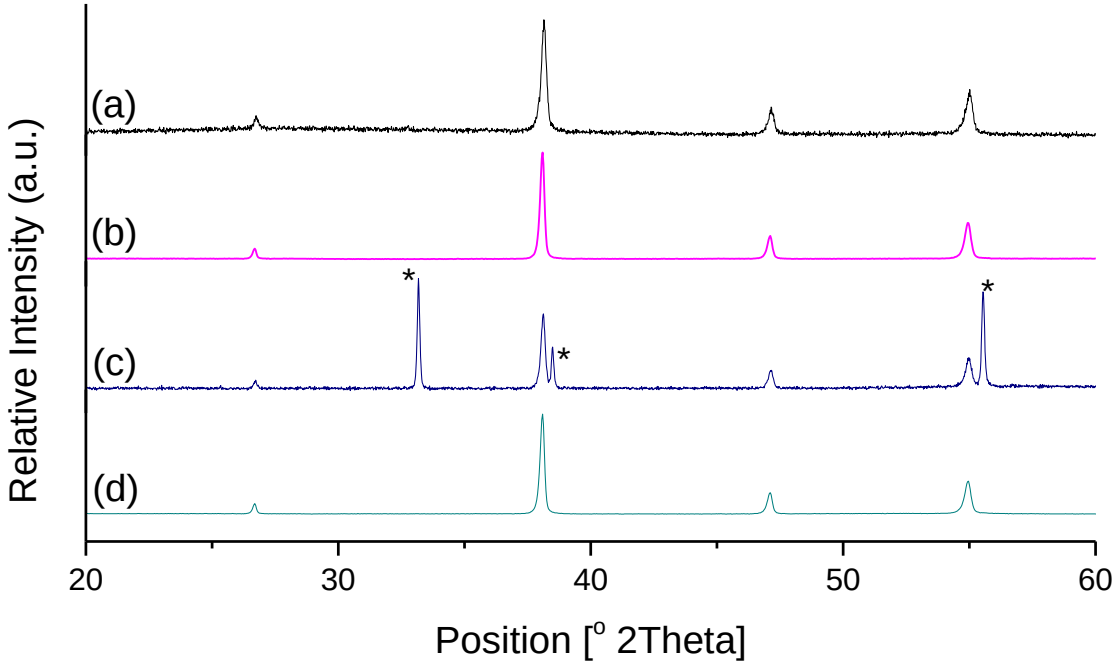

Fig 3.22, XRD of 0.5LCT-0.5BSCF (a) before and (b). after thermal stability test at 750°C for 5 days in air, (c) after compatibility tests with SDC and (d) after CO_2 tolerance tests.

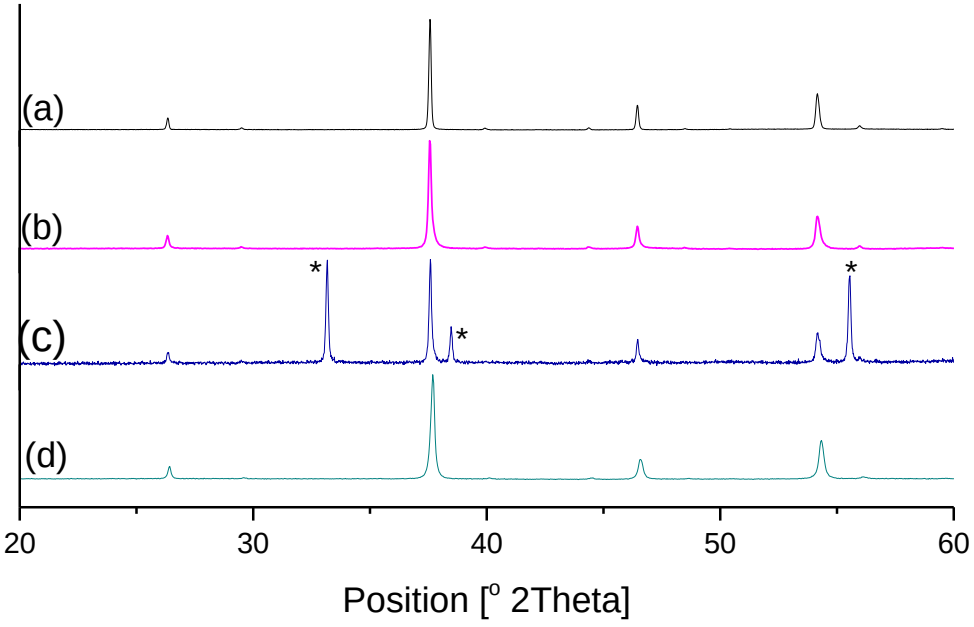

Fig 3.23, XRD of 0.9LCT-0.1BSCF (a) before and (b). after thermal stability test at 750°C for 5 days in air, (c) after compatibility tests with SDC and (d) after CO_2 tolerance tests.

Table 3.7. Summary of the products and their structure, lattice parameters from Pawley fitting of the three stability test of four LCT doped compositions

Reference	**0.5LCT-0.5BSCF**	**0.9LCT-0.1BSCF**
Powders after thermal stability		
Structure	Cubic perovskite	Orthorhombic
Lattice parameters	a1=b1=c1=3.87771(15) Å	a=5.55827(52)Å b=5.56197(59)Å c=7.84669(61)Å
	a2=b2=c2=3.88473(56) Å	
Powder after SDC compatibility		
Structure	Cubic perovskite	Orthorhombic
Lattice parameters	a1=b1=c1=3.88896(80) Å	a=5.56188(142)Å b=5.55925(141)Å c=7.84956(74)Å
	a2=b2=c2=3.88107(74) Å	
Powder after CO2 tolerance tests		
Structure	Cubic perovskite	Orthorhombic
Lattice parameters	a1=b1=c1=3.8981(16) Å	a=5.53918(29)Å b=5.55575(29)Å c=7.83307(48)Å
	a2=b2=c2=3.89174(74) Å	

For both 50% and 90%LCT-BSCF compositions, no new reflections were observed within the PXRD patterns, suggesting no new phase formation after these stability tests. Lattice parameters, as shown in Table 3.7 also remained mostly constant with only small deviations.

3.5. Electrical and electrochemical Properties

3.5.1. Electrical Conductivity

Electronic conductivity is an important property for a cathode to display, as it is required for the transport of electrons to the cathode surface in order to reduce O_2 into $2O^{2-}$. DC conductivities of the synthesised cathode materials were measured in order to obtain its electronic conductivity.

In the following discussion, the ionic contribution to the total conductivity is neglected because in the case of BSCF, the ionic conductivity estimated by extracting the value from oxygen permeation measurements[67] of 0.53-1.17 $S.cm^{-1}$, which are one to two orders of magnitudes below values for the electrical conductivity at corresponding temperatures. The electrical conductivity of the as made BCN-BSCF and LCT-BSCSF compositions was measured over the temperature range 500°C-700°C and are shown in Figure 3.24 with those of BSCF presented for comparison. As shown in the figure, the BCN doped cathode materials had low electronic conductivity compared to the undoped parent material, BSCF. At 650°C, sample containing only 5%BCN (0.05BCN-0.95BSCF) has a conductivity of 19.51$S.cm^{-1}$, which is less than half of that of BSCF. However, doping 5%LCT into BSCF (0.05LCT-0.95BSCF) produced very high conductivity, even higher than those of BSCF during the same temperature range. In both cases, when the doping material (BCN and LCT) reached 10%, a significant decrease of conductivity followed and decreases significantly on even increasing BCN and LCT composition.

Table 3.8. Electronic conductivity (S.cm^{-1}) in temperature range 500-700°C for BCN and LCT doped cathode materials.

Materials Reference	σ(500°C)	σ (550°C)	σ (600°C)	σ (650°C)	σ(700°C)
BSCF	47.87	46.31	45.52	44.88	44.83
0.05BCN-0.95BSCF	27.54	26.14	18.92	19.51	20.26
0.1BCN-0.9BSCF	9.76	10.05	11.09	11.86	12.58
0.5BCN-0.5BSCF	2.85	3.24	4.12	4.98	5.02
0.9BCN-0.1BSCF	0.013	0.024	0.032	0.051	0.07
0.05LCT-0.95BSCF	85.4	75.2	68.8	63.95	64.27
0.1LCT-0.9BSCF	7.33	8.82	10.78	13.77	14.6
0.5LCT-0.5BSCF	0.38	0.77	1.14	1.74	2.37
0.9LCT-0.1BSCF	0.03	0.043	0.066	0.09	0.13

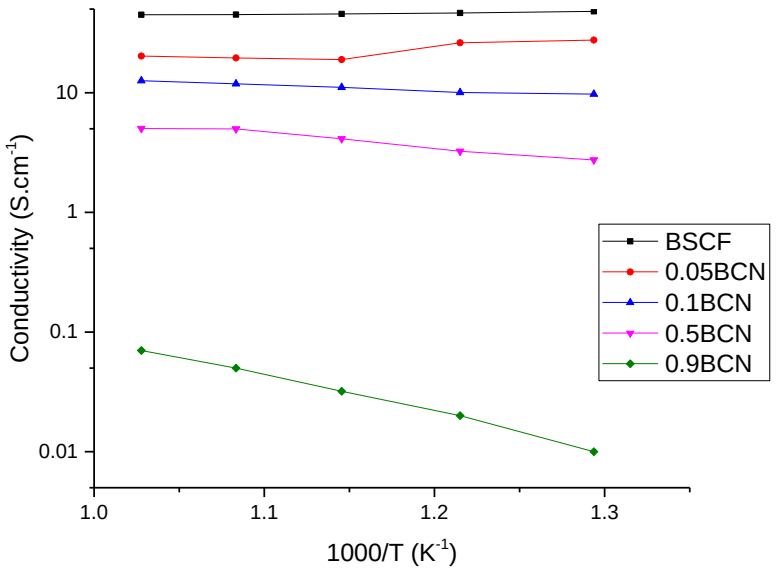

Fig 3.24(a). Electronic conductivity of the BSCF and BCN-BSCF cathode materials.

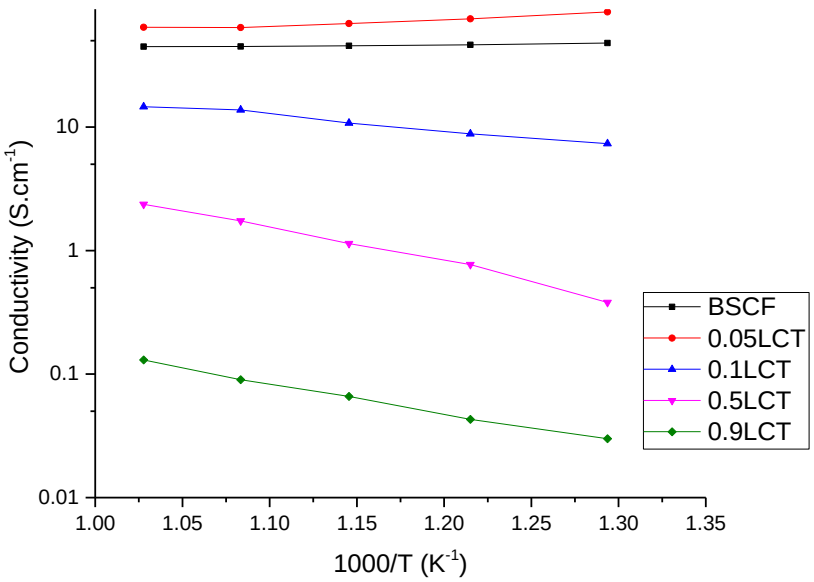

Fig 3.24(b). Electronic conductivity of the BSCF and LCT-BSCF cathode materials.

3.5.2. Thermogravimetric Analysis (TGA)

Thermogravimetric analysis (TGA) was performed for $Ba_3CoNb_2O_9$(BCN) and La_2CoTiO_6 (LCT) doped compositions, heating from room temperature to 750°C in a flowing air atmosphere at a heating and cooling rate of 5°C/min and repeated for three times for each sample as described previously in Section 3.2.2.4. The results of these TGA experiments are shown and analysed in this section.

In all the figures, the first cycle was not taken into account, as moisture removals can lead to artifacts. After the initial heat up, the TGA curves showed good reproducibility as the powder was thermally cycled, indicating that the powder was able to equilibrate with its surroundings (gaining or losing oxygen) on the time scale of the measurement. The data plotted in this section are from the third cycle.

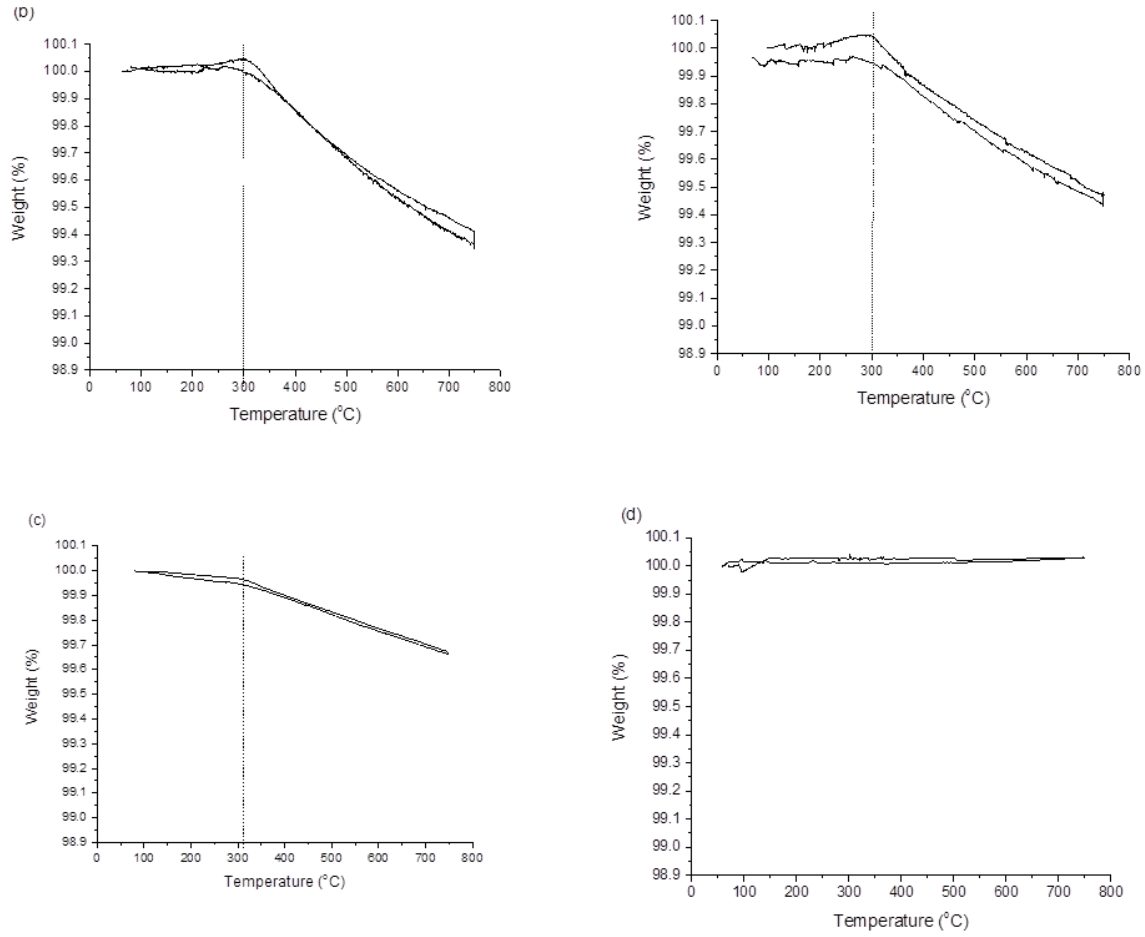

Figure 3.25: Thermogravimetric analysis (TGA) data for (a). 0.05BCN-0.95BSCF, (b), 0.1BCN-0.9BSCF, (c), 0.5BCN-0.5BSCF and (d), 0.9BCN-0.1BSCF showing the weight loss (weight%) upon heating up to 750°C and cooling back to room temperature.

TGA results showing how the weight change during heating for four BCN doped compositions are shown in Figures 3.25. For the lower BCN (5%~10%) containing compositions, there were a slight mass gain (0.05%) upon initial heating up to around 300°C. Where temperature reached 300°C, a steady mass loss happened up to the highest measuring temperature of ~750°C. The weight then started to regain for the cooling stage, stopped at a value similar to the original weight (~100%). There is a small hysteresis for most of the compositions tested during cooling, compared to heating, which is expected due to the slower kinetics involved in oxygen gain. 0.5BCNB-0.5BSCF composition had a slight weight loss up to 300°C, followed by a bigger weight loss by heating up the highest temperature and a weight re-gain when cooling back again. 0.9BCN-0.1BSCF showed very different behaviour than the other three components, which showed almost no weight loss during heating and cooling cycle.

A distinguished difference of the pattern was observed between the lower LCT doping (5~10%) compositions and higher LCT doping (50% and 90%) compositions (Figures 3.26). For the lower LCT doping compositions, the weight is fairly stable up to around 320°C, and followed by a continues weight loss from that point up to the highest measuring temperature. The behaviour of these two materials during heating and cooling are then very similar as the lower BCN containing compositions. Compared with the higher LCT doping compositions, lower LCT compositions showed more significant weight loss and it decreased with increasing doping level. The two higher LCT doped compositions, however, started to lose weight all the way upon heating up to the highest heating temperature. Again, the weight started to regain when cooling, reaching 100% of the original weight when temperature back to room temperature.

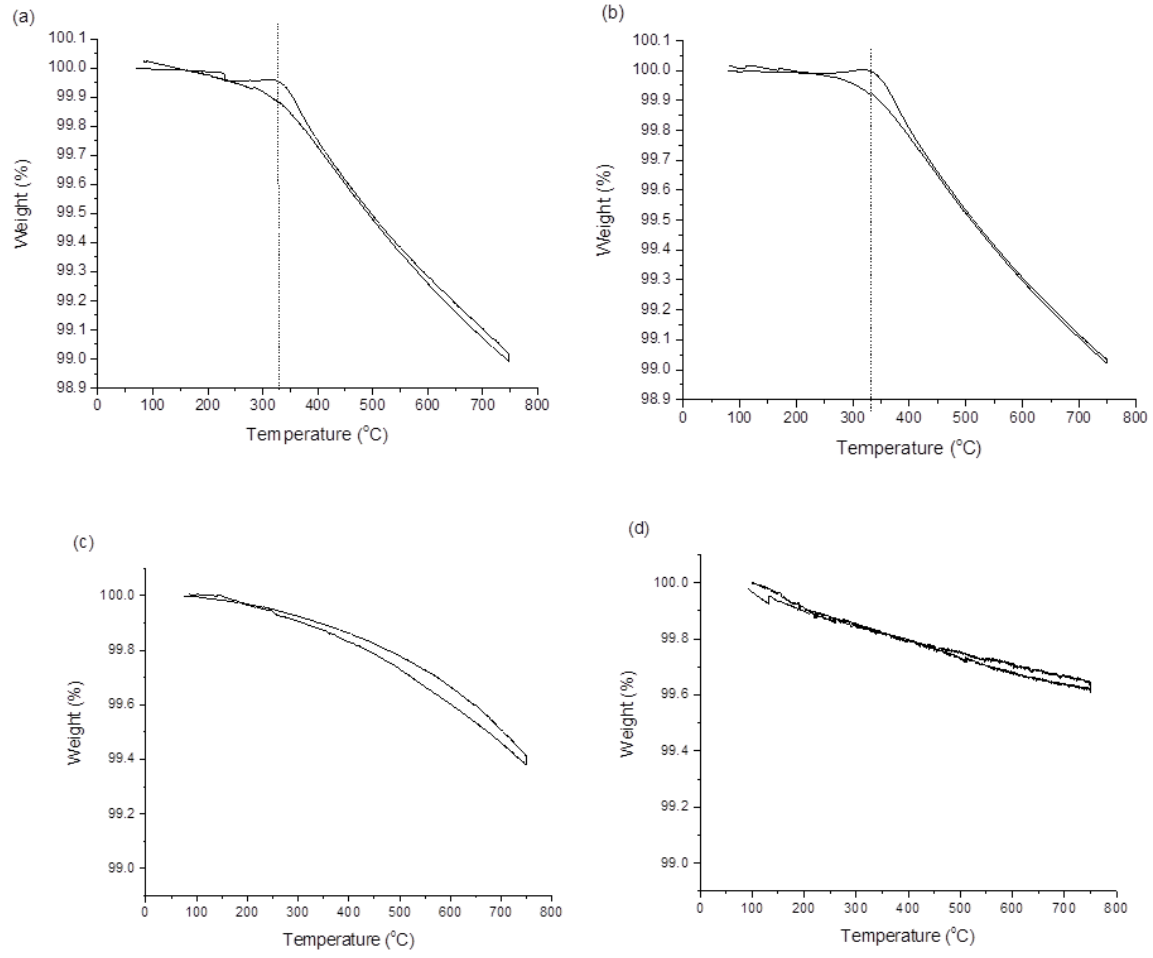

Figure 3.26: Thermogravimetric analysis (TGA) data for (a). 0.05LCT-0.95BSCF, (b). 0.1LCT-0.9BSCF, (c), 0.5LCT-0.5BSCF and (d), 0.9LCT-0.1BSCF showing the weight loss (weight%) upon heating up to 750°C and cooling back to room temperature.

The relative weight change as a function of temperature in air corresponds to the concentration of mobile oxygen species in the crystal lattices. Upon heating, the sample loses oxygen while the valent-alterable transition metals (M: Co, Fe) are reduced. The holes created by the reduction of the transition metals are balanced by the lattice reaction by increasing the number of oxygen vacancies (V_0'') into the lattice, as the sample loses oxygen during the heating process [10,11] (*Equation 3.2*).

$$O_o^x + 2h^{\cdot} \leftrightarrow {}^1/_2\, O_2(g) + V_o^{\cdot\cdot} \qquad \text{Equation 3.2.}$$

Where O_o^x is the lattice oxygen and $V_o^{\cdot\cdot}$refers to the oxygen vacancies with an effective charge of +2q. The oxygen losses calculated decreased significantly with higher BCN doped samples. This demonstrates that on increasing the doping content the number of oxygen vacancies is significantly reduced compared to the undoped BSCF and the lower doped materials, as charge balance requires an increase in the oxygen content to compensate for increased charge on the B-site. However, in the case of LCT doped materials, the oxygen losses calculated for the lower doping level is higher than the un-doped BSCF and this value also decreased with increasing LCT doping composition.

Table 3.9. Thermogravimetric analysis (TGA) data for BCN and LCT doped BSCF compositions, showing the weight loss corresponding to the oxygen loss from the lattice, upon heating at 750° for 30 minutes.

Materials Reference	Weight loss(%)	Change in oxygen stoichiometry
0.05BCN-0.95BSCF	0.71	0.088
0.1BCN-0.9BSCF	0.64	0.08
0.5BCN-0.5BSCF	0.17	0.021
0.9BCN-0.1BSCF	0	~0
0.05LCT-0.95BSCF	1.15	0.143
0.1LCT-0.9BSCF	1.125	0.140
0.5LCT-0.5BSCF	0.745	0.093
0.9LCT-0.1BSCF	0.463	0.058

3.5.3. Electrochemical Performance

The cathode performance of the BCN-BSCF and LCT-BSCF materials was investigated by measuring the AC impedance of symmetrical cells fabricated on SDC electrolyte substrates, as detailed in Section 3.2.2.5. AC impedance measurements were recorded over the temperature range of 500°C to 700°C in static air. The symmetrical cell was held for 90 minutes at each temperature to allow thermal equilibration and measurements were made using ZPlot v.2.9b (Scribner Assocaites) every 50°C. The ASR of the cathodes were calculated by fitting the data using ZView2.[61] The measurements were repeated for all the compositions for validating the reproducibility and the ones corresponding to the lowest values are plotted here.

Although the electronic conductivity of the BCN and LCT doped BSCF materials is relatively low, (conductivity of at least 100 $S.cm^{-1}$ are required for use as cathodes in IT-SOFC), it is not necessarily the defining property for a cathode. The chosen parent material, BSCF, is a prime example of a cathode with relatively low electronic conductivity but having an extremely low AC impedance of all the potential cathode materials. The cathode performance of the BCN-BSCF and LCT-BSCF samples was consequently measured by AC impedance and the results are shown in Table 3.10.

According to the literature, BSCF itself displays a range of ASR values from 0.13 to 2.1 $\Omega.cm^2$ at 600°C, depending on processing conditions and electrolytes. The ASR values of lower doped BSCF compositions (up to ~10% doping of BCN and LCT) are comparable with the lower ASR of BSCF at this temperature and also falls below 0.15 $\Omega.cm^2$ at the temperature range 600°C~700°C, a target suggested by Steele[68] for each of the three main components of a fuel cell, the cathode, anode and electrolyte. It could therefore be suggested that the potential operating temperature of a cathode produced from the above materials would be at this temperature range.

Table 3.10. Summary of information obtained from the electrochemical measurements of BCN and LCT doped compositions, showing the area specific resistance (ASR) at the temperature range (500°C-700°C).

ASR of BSCF-BCN and BSCF-LCT over the temperature range of 500°C-700°C ($\Omega.cm^2$)					
Materials reference	700°C	650°C	600°C	550°C	500°C
BSCF	0.04	0.10	0.22	0.37	0.99
0.05BCN-0.95BSCF	0.017	0.04	0.11	0.34	1.1
0.1BCN-0.9BSCF	0.018	0.05	0.12	0.33	0.99
0.5BCN-0.5BSCF	0.56	1.9	7.4	28.8	121.3
0.9BCN-0.1BSCF	2.37	5.74	23.14	147.9	237.1
0.05LCT-0.95BSCF	0.024	0.067	0.16	0.47	1.3
0.1LCT-0.9BSCF	0.0165	0.048	0.12	0.35	0.97
0.5LCT-0.5BSCF	0.77	1.8	4.9	15.5	57
0.9LCT-0.1BSCF	3.12	8.97	59.16	198.3	317.8

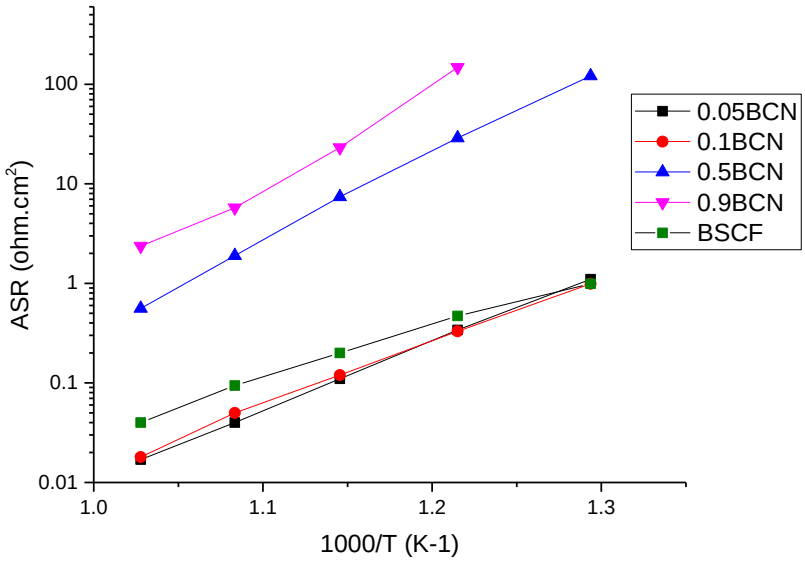

Figure 3.27. Arrhenius plots of ASR against temperature at the temperature range 500°C-700°C for 4 BCN-BSCF compositions.

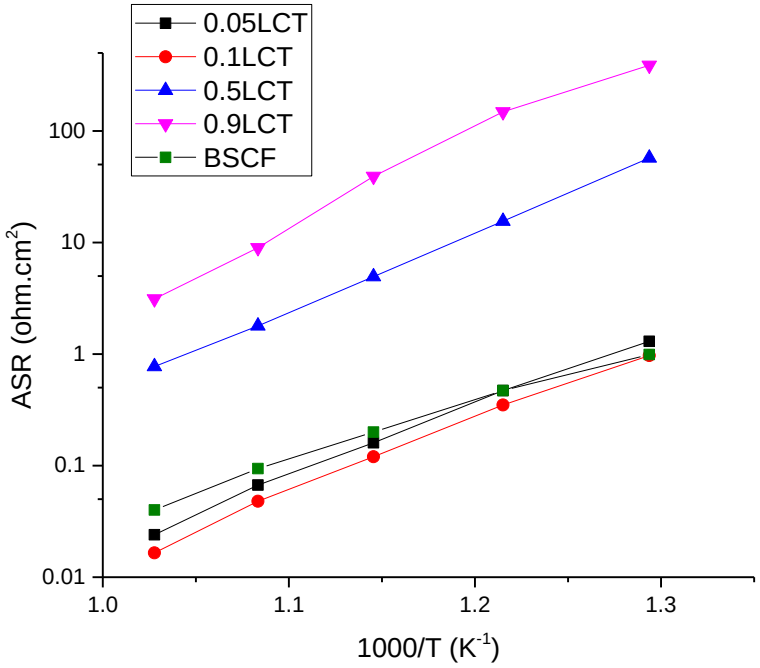

Figure 3.28. Arrhenius plots of ASR against temperature at the temperature range 500°C-700°C for 4 LCT-BSCF compositions.

In addition to excellent electrochemical performance, long-term stability of the conduction properties, especially at intermediate temperatures, is another important factor to consider for the practical application of a new candidate cathode material. A set of initial stability screening tests to examine the long term performance of BSCF and selected BCN-BSCF, LCT-BSCF cathode materials. An operating temperature of 650°C was chosen as the operating temperature in this series of experiments by looking at Table 3.10 as those materials showed very good ASR at this temperature and at the same time, an operating temperature as low as possible is desired. The comparison of the degradation in ASR for all the compositions at 650°C over 72 hours period is shown in Figure 3.29 and the changing rate of them are calculated as shown in Table 3.11 with the values for the commercial BSCF presented for comparison as well. Please note, the commercial BSCF symmetric cell was made using the same protocol as the rest of the cells in this work (Section 3.2.2.5).

Although the cathode material containing 10%$Ba_3CoNb_2O_9$ (BCN) (0.1BCN-0.9BSCF) exhibited the highest starting and end ASRs, it also has the lowest changing rate, $2.85\times10^{-6}\Omega.cm^2.min^{-1}$, even lower than that of the commercial BSCF. Apart from the absolute value of

ASR, this degradation rate is very important information for the evaluation of cathode materials for SOFC applications.

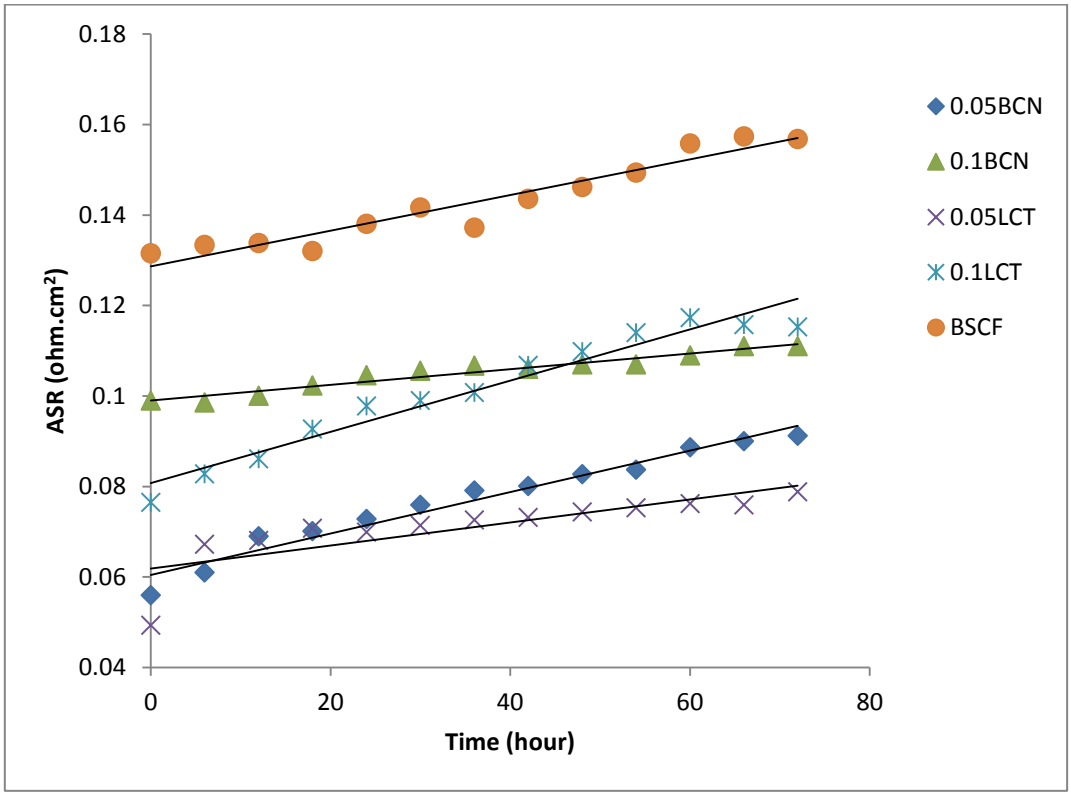

Fig 3.29. ASR at 650°C in static air for 72hours for four BCN and LCT doped compositions

Table 3.11. Information showing the starting ASR, end ASR and changing rate of commercial BSCF and 4 selected doped BSCF composition measured at 650°C in static air for 72hours.

Material reference	Starting ASR ($\Omega.cm^2$)	End ASR ($\Omega.cm^2$)	Changing rate ($\mu\Omega.cm^2.min^{-1}$)
0.05BCN-0.95BSCF	0.056	0.09	8.1
0.1BCN-0.9BSCF	0.099	0.111	2.85
0.05LCT-0.95BSCF	0.0493	0.0759	6.72
0.1LCT-0.9BSCF	0.0765	0.1158	9.92
BSCF	0.13	0.157	4.79

3.5.4. Post Impedance analysis

The microstructure and phase of the cathode material after ASR-ageing test were accessed by SEM on the selected cathode material, 0.1BCN-0.9BSCF, as it provided the best stability.

Cathode microstructure was examined using a Hitachi S-4800 field-emission scanning electron microscope (Oxford Instruments). Figure 3.30 shows SEM images taken at the surface of the cathode that was printed to create a symmetrical cell (before any kind of measurement was taken) with different magnifications. The surface appears to show a good amount of porosity, which should aid the diffusion of O_2 onto the surface of the cathode.

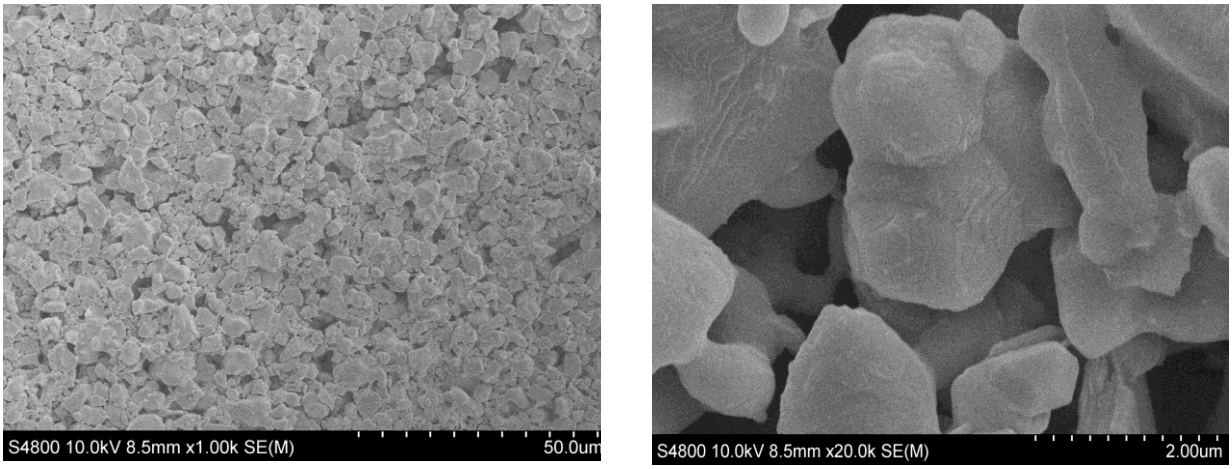

Fig 3.30(a) and (b). SEM on the cathode surface of the symmetric cells after printing

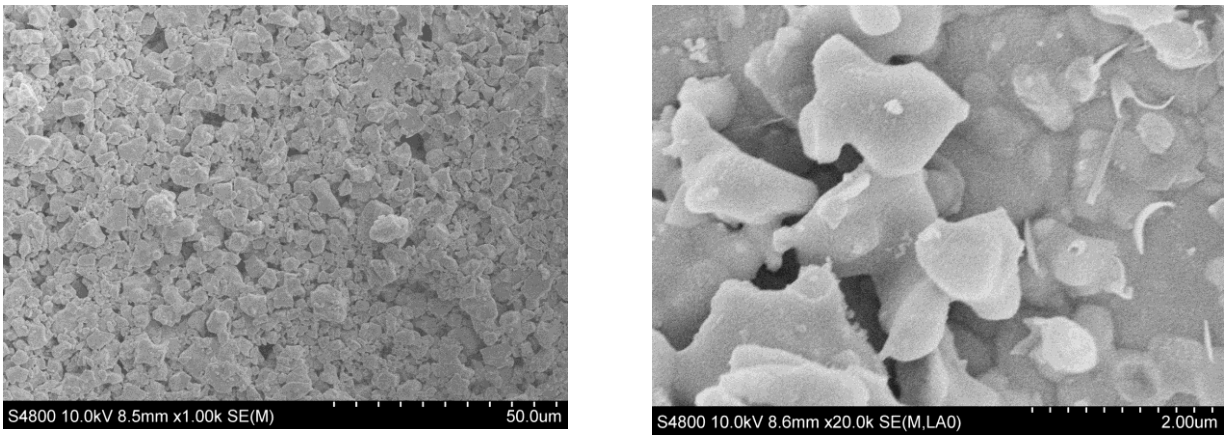

Fig 3.31(a) and (b). SEM on the cathode surface of the symmetric cells after impedance-ageing test at 650°C for 72hours.

Figure 3.31 shows SEM images taken at the surface of the cathode of the symmetric cell after ASR-ageing experiment has been performed. Therefore, this material has been heated at 650°C

for 72hours in static air. in general, the cathode material retained the good porosity after the measurements although a slight pore size shrinkage/closed pores is observed, caused by grain coarsening of the material during heating.

Figure 3.32 shows the room temperature PXRD of 0.1BCN-0.9BSCF cell after impedance-VT measurements and after impedance-ageing test. The PXRD pattern of the cathode material after ASR measurement was taken was in general well fitted by the original structural model for 0.1BCN-0.9BSCF material: a two cubic perovskite model with both symmetry of Pm-3m with gold, which could come from the gold paste and gold gauze as introduced in Section 3.2.2.5. The change of the lattice parameters of 0.1BCN-0.9BSCF was summarised and was compared to the as synthesised material in Table 3.12. Although no obvious sign of extra peak, the lattice parameters of both cubic perovksite phases changed significantly, indicating lattice expansion/shrinkage.

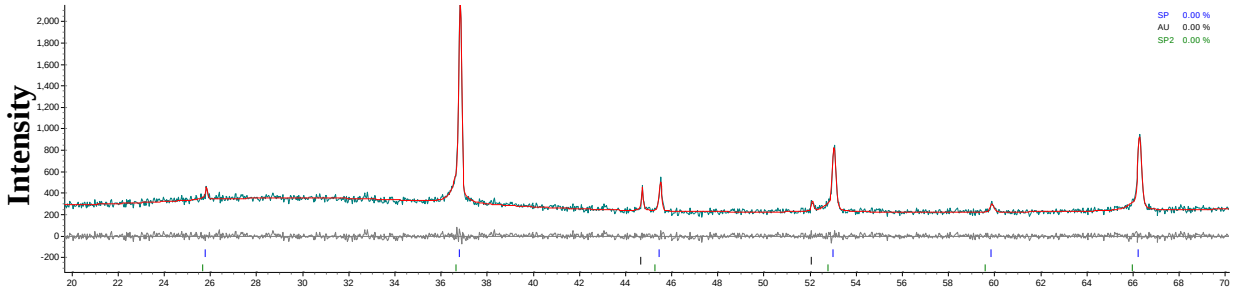

Fig 3.32(a). Pawley refinement (red line) of XRD data (2θ=20°-70°) for 0.1BCN-0.9BSCF cathode material (green line). Grey line represents the difference between calculated and measured data, with the black tick marks showing the allowed reflections. The pattern was fitted with three phases: two cubic perovskite structures (both Pm-3m) and gold.

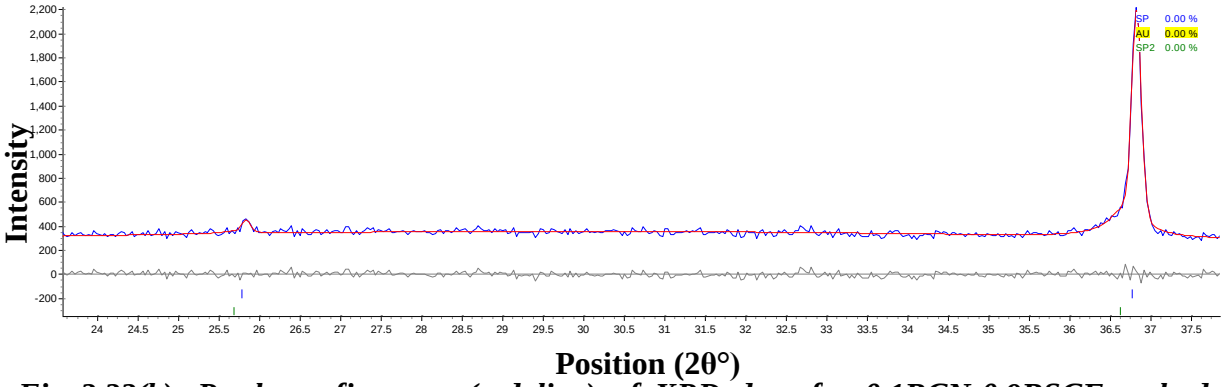

Fig 3.32(b). Pawley refinement (red line) of XRD data for 0.1BCN-0.9BSCF cathode material (blue line). The pattern was fitted with three phases: two cubic perovskite structures (both Pm-3m) and gold. 2θ= 24°-38° range showed no obvious appearance of any extra phases.

Table 3.12. Structure and lattice parameters (from Pawley fitting) of 0.1BCN-0.9BSCF as synthesised cathode materials and cathode material after impedance measurements.

Material	Structure	Lattice parameters
As made powder	Cubic perovskite ×2	a1=4.03043(6)
		a1=4.03043(6)
Cathode after impedance measurements	Cubic perovskite ×2	a1=4.01018(23)
		a2=4.07681(26)

3.6. Discussion

This chapter focused on the synthesis and preliminary experiments to investigate the structure and properties of two cathode materials based on BSCF. A triple perovskite, BCN and a double perovskite, LCT, were added as the doping component to BSCF and four different doping compositions, from 5% to 90%, were used in both materials. Their properties were tested to access their potential to be used as IT-SOFC.

When adding BCN and LCT into BSCF, we expected to find the formation of an endotaxial nanocomposite structure as in the case of BSCFMo, as in this material, the formation of the double perovskite phase provided the much-needed improved phase stability. Despite the layered perovskite structure of BCN and LCT, no strong evidence of layered structure was found in this study, by examining both laboratory PXRD and high resolution synchrotron data. As a general rule when the oxidation states of B and B' cations differ by less than two a disordered arrangement is observed whereas, a difference greater than two nearly always produces an ordered arrangement. When the difference in oxidation states is exactly two, disordered, partially ordered, or fully ordered arrangements can result, depending on differences in size and/ or bonding preference of the B and B' cations.[9, 16, 17]

An average oxidation state of 3.4 for (Co, Fe) can be calculated from data of oxygen nonstoichiometry of BSCF powder slowly cooled to room temperature,[69] whilst data from X-ray photoelectron spectroscopy entirely discard the presence of Co^{2+}.[70] Based on these observations, the difference between the oxidation state between the B-site cation (if we take Co, Fe as B) and B'-site cation (Nb and Ti) is not large enough to favour the formation of the layer structure in general.

Adding of 5% of BCN (0.05BCN-0.95BSCF) has resulted in the formation of a solid solution that is isostructural with the parent materials with a increased lattice parameter, which is well expected in view of (1) the partial substitution of Ba (1.61Å) for the smaller-sized Sr (1.44Å) cations, and (2) the larger ionic radius of Nb^{5+}, 0.64 Å (in 6-fold coordination) relative to that of Co^{3+}, 0.61 Å and 0.545 Å, in high and low-spin configuration, respectively, or Co^{4+}, 0.53 Å in high-spin configuration. Therefore, with more Ba replacing Sr in A-site and Nb replacing Co in B-site, the lattice parameter had a linear expansion throughout the whole series.

On the other side, for LCT-BSCF materials, the lattice parameters decrease slightly with increasing LCT doping level. Because the ionic radius of Ti^{4+} (0.605Å) was larger than that of $Co^{3+/4+}$ cations, the reason for the decrease of the lattice parameter of the LCT doped material

can only be caused by the substitution of La^{3+} (1.36Å), which has smaller radius than Ba^{2+} and Sr^{2+}. It then resulted in a decreased average radius of A-site (r_A). A decrease of the mean distances A–O, A–Fe is observed with decreasing (r_A).[71] The continuous decrease of r_A with even increasing amount of LCT caused the lattice parameters to decrease even more. The transfer of the cubic perovskite to monoclinic structure of 0.9LCT-0.1BSCF is possibly related to the change of the tolerance factor, t (described in Equation 1.4), where t decreases continuously with $r_A$kept decreasing whilst r_B kept increasing.

The effect of doping BCN and LCT on the stability of the cathode material is very substantial even by adding only 5% of the doping component. The improvement of adding Nb and Ti on the stability of the BSCF-based material has also been investigated and shown by other researchers.[72-75]

The driving force for the decomposition of the cubic BSCF is believed to be the Co preference for the low-spin configuration in the Co^{3+} (d^6) oxidation state, which is favoured at temperatures below 900°C due to oxidation of Co^{2+} (d^7) present in the BSCF cubic structure.

The good stability of the BCN/LCT doped materials, especially BCN-BSCF composition, is a promising property as many other cathodes containing alkaline-earth elements have been reported to have a low tolerance for CO_2, particularly those that contain Ba, decomposing into carbonates in its presence.[76] This then leads to the requirement of CO_2 removal from air before it reaches the cathode, reducing the viability and flexibility of the fuel cell.

The mechanism of Nb/Ti stabilisation effect for cubic perovskite, against transformation to hexagonal and other structures, can be understood by the distinctness between cubic and hexagonal perovskite structures. It is well known that the BO_6 octahedra, which are the skeleton of the cubic structure, are corner shared in cubic perovskite. However, the BO_6 octahedra are face-shared in the hexagonal structure; therefore the distance between the B-site cations in hexagonal structure is shorter than that in cubic perovskite. Donor substitution of Nb/Ti for Co/Fe will increase the average valance of B-site cations, and thus raise the electrostatic repulsion and destabilize the hexagonal structure. Consequently, the material will prefer to take the cubic structure with longer distance between B-site cations.

Other researchers have also studied the stability improvement of Nb doped material in terms of the binding energy.[77] Binding energy is the energy required to disassemble a whole system into separate parts.[78] The binding energy E_B is given by the following expression:

$$E_B = \sum E_{Atom\ (k)} n_{(k)} - E_{Total}$$ Equation 3.3.

Where E_{Total} is the total energy of the crystal lattice, $E_{Atom(k)}$ is the total enegy of isolated atom K in vacuum, and $n_{(k)}$ is the number of atom k.[79] Here, the binding energy is referred to describe the chemical stability of perovskite materials. It is stated that the greater the binding energy is, the more stable and possibly existence the corresponding phase is. Fig. 3.33 shows the binding energies in $BaBO_3$ (B = Co, Fe, Nb) estimated by first-principles calculations via the software of VASP, which is based on the density-functional theory (DFT). High valence Nb ions will increase the binding energy of $BaBO_3$-based materials. Therefore, Nb is shown to be good choices of all the present elements to improve the stability of $BaBO_3$-based materials.

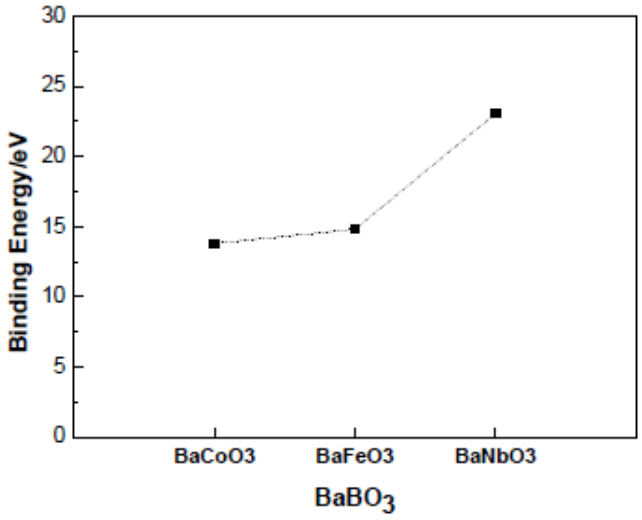

Fig 3.33. Calculated binding energy of $BaBO_3$ (B-Co, Fe, Nb) obtained with DFT calculations. [79]

The linear relationship between log (σ) versus reciprocal temperature (1000/T) is observed for all the compositions tested. Both the temperature dependence of the electrical conductivity of undoped parent material BSCF and 0.05LCT doped composition displayed a p-type mixed conductors with its electrical conductivity decreased with increasing temperature in the temperature range tested (500°C-700°C) (Equation 3.2). The relative high amount of lattice oxygen released at elevated temperature, as shown in TGA results, of these two materials leads to the partial annihilation of electronic holes, and thus results in the decreases of the electronic conductivity.

The conductivity of the perovskite mixed conductors is caused by the co-presence of electrons and oxygen vacancies exhibiting simultaneously electronic and ionic conductivities. Because the electronic conductivity is always at least one order of magnitude higher than the ionic

conductivity, the measured total conductivity can be mainly referred to the electronic conductivity.

The electronic conductivity is determined by the concentration of charge carriers (mainly electron holes) and their mobility. Upon heating the transition metals are reduced followed by creation of holes and can be described by equation 3.4 and 3.5, according to the Kroger-Vink notation.

$$Co_{Co}^{x} \leftrightarrow Co_{Co}^{'} + h^{\cdot} \qquad \text{Equation 3.4.}$$

$$Fe_{Fe}^{\times} \leftrightarrow Fe_{Fe}^{\times} + h^{\cdot} \qquad \text{Equation 3.5.}$$

Where $M_M^{'}$ (M: Co or Fe) refers to $M^{(x-1)}$ localised on M^x site, M_M^x stands for M^x and $h^{\cdot}$ for holes.

In the case of BSCF, data of thermopower and oxygen nonstoichiometry confirm p-type small polaron hopping between (Co, Fe)$^{4+}$ to (Co, Fe)$^{3+}$ cations upon heating to 900°C.[80, 81] Substitution of elements with stable valence states for the aliovalent cations decrease the total conductivity were reported in many oxide compounds, e.g. $Ba_{0.5}Sr_{0.5}Zn_{0.2}Fe_{0.8}O_{3-\delta}$ (Zn for Fe) Therefore, the donor doping of Nb and Ti at B-site may result in the partial reduction of (Co, Fe)$^{4+}$ to (Co, Fe)$^{3+}$ and hence decrease the concentration of the electronic holes as charge compensation. The increase in ionic radius due to the reduction of (Co, Fe)$^{4+}$ to (Co, Fe)$^{3+}$ will increase the (Co, Fe)–B–(Co, Fe) bond length, which may inhibit polaron transport and then make the conduction of electronic holes more difficult through the bulk. Nb/Ti with fixed valance state does not contribute to the electronic conductivity. All the above mentioned reasons can account for the decrease of the electrical conductivity with Nb/Ti doping dose at B-site.

Despite the low electrical conductivity of BCN-BSCF and LCT-BSCF cathode material, the ASR results showed that lower doping levels in the BCN and LCT doped cathode materials exhibited comparable or improved area specific resistance(ASR) with the un-doped BSCF, prepared in an identical way. According to the literature, BSCF itself displays a range of ASR values from 0.03 to 10 Ω.cm^2 at 650^{o}C, depending on processing conditions and electrolytes.[31, 82, 83] The 5% and 10% BCN/LCT doped cathode material achieved ASRs well below 0.15 Ω.cm^2 at 650°C, showing its potential to operate at such a low operational temperature for IT-SOFC.

The good electrochemical properties of BSCF are reported to result from high oxygen ionic conductivity, originated by the high oxygen non-stoichiometry and concentration of oxygen vacancies, which can also be used to explain the low ASR of 0.05LCT doped composition, as indicated by the high oxygen loss content and the conductivity.

As discussed in Section 1.4, the actual reaction in SOFC cathode is quite complex and comprises a number of element steps. These steps can include: (1), diffusion of oxygen molecules to the cathode, (2), adsorption to the surface and/or bulk of the cathode, (3), dissociation of molecular to atomic species, (4), oxygen exchange redox reaction between the adsorbed oxygen and the cathode material producing oxygen ions, and (5), the incorporation of oxide ions into vacancies in the crystal lattice of the cathode, and (6), the produced oxygen ions transported to and across the cathode-electrolyte interface and finally incorporated into the crystal structure of the electrolyte. It would be hard to comment now how the incorporation of BCN and LCT can affect the reaction mechanism of the doped BSCF cathode material without further investigations. It could only be assumed that adding small amount of the doping component retain, or even improve the activity of oxygen reduction reaction (ORR) in the cathode or accelerate the materials transport inside the cathode or across the cathode/electrolyte interface.

The long-term stability of ASR of the doped cathode materials is another promising property of this material as shown in Figure 3.29; with 0.1BCN-0.9BSCF material exhibited the lowest changing rate of ASR across the time range. PXRD of this particular material after the long-term measurement didn't show formation of extra phases, indicating again the improved stability of this material. From the XRD pattern shown, one could imagine that even if extra phases were formed, the amount of them would be very small so that they almost could be neglected for the time scale tested. SEM showed that the particles tend to coarsen with the temperature and time and caused the pores to close. Considering no obvious solid reactions observed inside the cathode material, the main reason for the performance degradation could then be the morphological change of the cathode particles, due to limited diffusion, bigger particles and decreased number of active sites for ORR compared to the cathode material before measurement.

Chapter 4 Conclusion and Future Work

4.1. Conclusion

The work presented in this thesis focused on the synthesis of a range of BSCF-BCN and BSCF-LCT compositions, with various BCN and LCT contents, followed by structural characterisation and evaluation as cathode materials for intermediate temperature (600°C-800°C) solid oxide fuel cells (IT-SOFCs).

All in all, the outcome of this thesis can be summarised as follows:

- When doping different amount of $Ba_3CoNb_2O_9$ (BCN) and La_2CoTiO_6 (LCT) into BSCF to form new cathode material, three materials (0.05BCN-0.95BSCF, 0.05LCT-0.95BSCF, 0.1LCT-0.9BSCF) formed solid solution of cubic perovskite (*Pm-3m*) , that is isostructural to the parent BSCF materials.
- 0.1BCN-0.9BSCF, 0.5BCN-0.5BSCF and 0.5LCT-0.5BSCF all afford two cubic perovskites (both *Pm-3m*).
- The doping of BCN and LCT considerably increased the stability of the material as evidenced by three stability tests. The more the doping component, the more stable the material.
- Apart from the 0.05LCT-0.95BSCF, all the other doped materials exhibited lower oxygen nonstoichiometry and total conductivity. However, low BCN and LCT doped compositions exhibited comparable ASRs with those of BSCF during the temperature range 500°C-700°C, which is a very promising property to be used as IT-SOFC material.
- The long term ASR measurement of 0.1BCN-0.9BSCF showed to be quite promising, with a lower starting and ending ASR, and a lower changing rate than those of BSCF for the temperature and time period tested (650°C for 72 hours).

4.2. Future Work

The materials with lower doping levels of BCN and LCT studied in this thesis displayed potential to be utilised as cathodes for IT-SOFCs due to their good cathode performance, along with great stability at operating and fabrication conditions. Due to the good performance, it would be interesting to further investigation these materials. A few ideas would be as follows:

- Using different synthesis methods (other than the solid state synthesis used in this thesis), such as sol-gel.
- Experiments showed that doping level of 10%BCN produced material with best electrochemical performance. Increasing doping level above 10% diminished the electrochemical performance while increased the stability of the material. Therefore, investigation can be carried out in order to find out the optimum doping level (around 10% doping level).
- Further modification to the cathode materials could be pursued in order to improve performance, such as through optimising modification of the cathode microstructure through processing conditions, or with a porous electrolyte layer at the cathode-electrolyte interface.

Appendix

Apart from the BSCF-BCN and BSCF-LCT cathode materials described in the main body of this thesis, I have also synthesised other cathode materials and have had some preliminary ASR measurements done to these materials. The structures and ASRs of these materials are shown below in this Appendix. These materials are based on three parent materials, these are (1). $Ba_{0.5}Sr_{0.5}Co_{0.8}Fe_{0.2}O_{3-\delta}$ (BSCF), (2). $La_{0.5}Sr_{0.5}Co_{0.2}Fe_{0.8}O_{3-\delta}$ (LSCF), and (3). $Bi_{0.15}Sr_{0.85}Co_{0.8}Fe_{0.2}O_{3-\delta}$ (BiSCF). BSCF and LSCF cathode materials has already been introduced previously in Chapter 1. BiSCF material has recently been investigated due to its very high conductivity.[84]

In this Appendix, the materials synthesised are divided into three groups: 1). BSCF based, (2). LSCF based, and (3). BiSCF based.

In order to make the table easier to read, the single cubic perovskite structure will be written as SP and the double perovskite structure will be written as DP in the tables.

1. **$Ba_{0.5}Sr_{0.5}Co_{0.8}Fe_{0.2}O_{3-\delta}$(BSCF) based materials**

   1.1.W doped BSCF (BSCFW)

Table 1.1(a): Composition and structure of BSCFW materials

	Materials composition					Structure information
	Ba	**Sr**	**Co**	**Fe**	**W**	
BSCF	0.5	0.5	0.8	0.2	0	SP *(Pm-3m)*
BSCFW00625			0.75	0.1875	0.0625	SP(*Pm-3m*) + DP(*Fm-3m*)
BSCFW015			0.68	0.17	0.15	
BSCFW025			0.6	0.15	0.25	
BSCFW03			0.56	0.14	0.3	
BSCFW03125			0.55	0.1375	0.3125	
BSCFW0375			0.5	0.125	0.375	
BSCFW045			0.44	0.11	0.45	
BSCFW05			0.4	0.1	0.5	SP(*Pm-3m*) + DP(*Fm-3m*) + $BaWO_4$ ($I4_1/a$)

Table 1.1(b): Impedance information of BSCFW materials

ASR ($\Omega.cm^2$) of BSCFW at different temperatures between temperature range of 550°C-750°C. Electrolyte: SDC					
	550°C	**600°C**	**650°C**	**700°C**	**750°C**
BSCF	0.55	0.31	0.16	0.089	0.062
BSCFW00625	4.57	1.63	0.63	0.24	0.1
BSCFW015	7.62	2.58	0.96	0.37	0.15
BSCFW025	4.52	1.66	0.77	0.269	0.098
BSCFW03	2.002	0.673	0.245	0.096	0.042
BSCFW03125	1.953	0.636	0.227	0.089	0.036
BSCFW0375	4.99	1.64	0.60	0.22	0.091
BSCFW045	12.5	3.31	0.96	0.32	0.12

1.2.Re doped BSCF (BSCF-Re)

Table 1.2(a): Composition and structure information of synthesised BSCF-Re materials

	Materials Composition					**Structure information**
	Ba	**Sr**	**Co**	**Fe**	**Re**	
5%Re-BSCF	0.5	0.5	0.665	0.285	0.05	SP (*Pm-3m*)
10%Re-BSCF			0.63	0.27	0.1	
15%Re-BSCF			0.595	0.255	0.15	
20%Re-BSCF			0.56	0.24	0.2	
25%Re-BSCF			0.525	0.225	0.25	
30%Re-BSCF			0.49	0.21	0.3	SP (*Pm-3m*) +DP (*Fm-3m*)
34%Re-BSCF			0.462	0.198	0.34	
38%Re-BSCF			0.434	0.186	0.38	SP (*Pm-3m*) + DP (*Fm-3m*) + $Ba_4CoRe_2O_{12}$ (*R-3m*)

Table 1.3(b): Area Specific Resistance (ASR) of synthesised BSCF-Re materials during the temperature range 550°C-750°C.

ASR ($\Omega.cm^2$) of BSCF-Re materials over the temperature range of 550°C -750°C. Electrolyte: SDC					
	550°C	**600°C**	**650°C**	**700°C**	**750°C**
5%Re-BSCF	Sym cell failed due to delamination				
10%Re-BSCF					
15%Re-BSCF					
20%Re-BSCF	31	13.3	5.59	2.18	1.31
25%Re-BSCF	57	21.1	6.3	2.2	1.28
30%Re-BSCF	97	29.4	7.9	2.4	1.16
34%Re-BSCF	126	31	8.1	2.5	1.13
38%Re-BSCF	168	37.4	9.1	2.4	1.04

2. $La_{0.5}Sr_{0.5}Co_{0.2}Fe_{0.8}O_{3-\delta}$(LSCF)-based materials

2.1. $La_{0.5}Sr_{0.5}Co_{0.2}Fe_{0.8}O_{3-\delta}$ -La_2CoTiO_6 (LSCF-LCT)

Table 2.1(a): Materials composition and structure information of LSCF-LCT materials

	Materials Composition					**Structure information**
	La	**Sr**	**Co**	**Fe**	**Ti**	
10%LCT-LSCF	0.55	0.45	0.23	0.72	0.05	Rhombohedral (*R-3c*)
30%LCT-LSCF	0.65	0.35	0.29	0.56	0.15	
50%LCT-LSCF	0.75	0.25	0.35	0.4	0.25	
70%LCT-LSCF	0.85	0.15	0.41	0.24	0.35	
90%LCT-LSCF	0.95	0.05	0.47	0.08	0.45	Orthorhombic (*Pbnm*)

Table 2.1(b). Area Specific Resistance (ASR) of synthesised LSCF-LCT materials during the temperature range 550°C-750°C.

ASR ($\Omega.cm^2$) of selected LSCF-LCT materials over the temperature range of 550°C-750°C. Electrolyte: SDC					
	550°C	**600°C**	**650°C**	**700°C**	**750°C**
90%LSCF-LCT	29	7.12	2.1	0.74	0.13
70%LSCF-LCT	78	17	4.4	1.3	0.41
50%LSCF-LCT	157	27	7.2	1.97	0.78
30%LSCF-LCT	235	50	12	3.6	1.4
10%LSCF-LCT	329	88	25	8.1	3

2.2.$La_{0.5}Sr_{0.5}Co_{0.2}Fe_{0.8}O_{3-\delta}$ -$LaSrCoNbO_6$/$LaSrCoTaO_6$ (LSCF-LSCNb/Ta)

Table 2.2(a): Materials composition and structure information of LSCF-LSCNb/Ta materials

	Materials Composition					**Structure information**
	La	**Sr**	**Co**	**Fe**	**Nb/Ta**	
10%LSCNb-LSCF	0.5	0.5	0.23	0.72	0.05	Rhombohedral (*R-3c*)
10%LSCTa-LSCF						
40%LSCNb-LSCF			0.32	0.48	0.2	
40%LSCTa-LSCF						
90%LSCNb-LSCF			0.47	0.08	0.45	SP (*Pm-3m*) +DP (*Fm-3m*)
90%LSCTa-LSCF						

Table 2.2(b). Area Specific Resistance (ASR) of synthesised LSCF-LSCNb/Ta materials during the temperature range 550°C-750°C.

ASR ($\Omega.cm^2$) of LSCF-LSCNb/Ta materials over the temperature range of 550°C-750°C. Electrolyte: SDC					
	550°C	600°C	650°C	700°C	750°C
10%LSCNb-LSCF	10.4	2.7	0.86	0.33	0.15
10%LSCTa-LSCF	11.2	2.6	0.87	0.41	0.18
40%LSCNb-LSCF	78	17.4	4.3	1.3	0.43
40%LSCTa-LSCF	102	24	5.5	1.6	0.55
90%LSCNb-LSCF	Too big	143	54	16.8	5.8
90%LSCTa-LSCF	to measure	167	53	14.4	4.3

3. $Bi_{0.15}Sr_{0.85}Co_{0.8}Fe_{0.2}O_{3-\delta}$(BiSCF)-based materials

Table 3(a): Materials composition and structure information of various doped BiSCF materials

	Materials Composition					Structure information
	Bi	**Sr**	**Co**	**Fe**	**Doping elements**	
BiSCF	0.15	0.85	0.8	0.2		SP (*Pm-3m*) +CoO (*Fm-3m*)
5%Mo-BiSCF			0.76	0.19	0.05	SP (*Pm-3m*) + CoO(*Fm-3m*)
10%Mo-BiSCF			0.72	0.18	0.1	SP (*Pm-3m*) + tetragonal (*P4/mmm*) + CoO
5%W-BiSCF			0.76	0.19	0.05	SP (*Pm-3m*) + tetragonal (*I4/m*) + CoO (*Fm-3m*)
10%W-BiSCF			0.72	0.18	0.1	SP (*Pm-3m*) + tetragonal (*I4/m*) + CoO(*Fm-3m*)
5%Nb-BiSCF			0.76	0.19	0.05	SP(*Pm-3m*) + Sr_2FeO_4 (*I4/mmm*)
5%Zr-BiSCF			0.76	0.19	0.05	SP (*Pm-3m*) + $SrZrO_3$(*Pbnm*) + CoO (*Fm-3m*)

Table 3(b). Area Specific Resistance (ASR) of synthesised BiSCF and its various doped materials during the temperature range 550°C-750°C.

ASR ($\Omega.cm^2$) of selected BiSCF and its doped materials over the temperature range of 550°C-750°C. Electrolyte: LSGM					
	550°C	**600°C**	**650°C**	**700°C**	**750°C**
BiSCF	0.87	0.31	0.099	0.05	0.034
Mo0.1-BiSCF	2.4	0.8	0.29	0.15	0.06
W0.05-BiSCF	0.86	0.28	0.12	0.058	0.033
W0.1-BiSCF	0.97	0.2	0.11	0.053	0.028
Nb0.05-BiSCF	3.14	0.89	0.25	0.13	0.08
Zr0.05-BiSCF	2.17	0.69	0.18	0.11	0.068
Commercial BSCF	0.5	0.095	0.041	0.024	0.017

Reference

1. A. Boudghene Stambouli, E.T., *Solid Oxide Fuel Cells (SOFCs): A Review of An Environmentally Clean and Efficient Source of Energy. .* Renewable and Sustainable Energy Reviews, 2002. **6**: p. 433-455.
2. *Climate of 2001; Annual Review.* National Oceanic and Atmospheric Administration. , 2001.
3. *Survey of Energy Resources.* World Energy Council (WEC), 1998.
4. *United State Department of Energy Review 2001.*
5. Lashtabeg, A. and S.J. Skinner, *Solid Oxide Fuel Cells: A Challenge for Materials Chemists?* Journal of Materials Chemistry, 2006. **16**(31): p. 3161.
6. Jacobson, A.J., *Materials for Solid Oxide Fuel Cells.* Chemistry of Materials, 2010. **22**(3): p. 660-674.
7. Zhou, W., R. Ran, and Z. Shao, *Progress in Understanding and Development of $Ba_{0.5}Sr_{0.5}Co_{0.8}Fe_{0.2}O_{3-\delta}$-Based Cathodes for Intermediate-Temperature Solid-Oxide Fuel Cells: A Review.* Journal of Power Sources, 2009. **192**(2): p. 231-246.
8. Brian C. H. Steele, A.H., *Materials for Fuel Cell Technologies.* Nature, 2001. **414**(345-352).
9. P. Woodward, R.-D.H., and A. W. Sleight, *Order-disorder in $A_2M^{3+}M^{5+}O_6$ Perovskites.* J. Mater. Res.,, 1994. **9**(8): p. 2118-2127.
10. Brandon, N.P., S. Skinner, and B.C.H. Steele, *Recentadvances Inmaterials For Fuel Cells.* Annual Review of Materials Research, 2003. **33**(1): p. 183-213.
11. Sun, C., R. Hui, and J. Roller, *Cathode Materials for Solid Oxide Fuel Cells: A Review.* Journal of Solid State Electrochemistry, 2009. **14**(7): p. 1125-1144.
12. Orera, A. and P.R. Slater, *New Chemical Systems for Solid Oxide Fuel Cells.* Chemistry of Materials, 2010. **22**(3): p. 675-690.
13. Ishihara, T., *Structure and Properties of Perovskite Oxides.* 2009: p. 1-16.
14. A.S. Bhalla, R.G.a.R.R., *The Perovskite Structure – A Review of Its Role in Ceramic Science and Technology.* Material Research Innovations, 2000. **4**(1): p. 3-26.
15. King, G. and P.M. Woodward, *Cation Ordering in Perovskites.* Journal of Materials Chemistry, 2010. **20**(28): p. 5785.
16. P. W. Barnes, M.W.L., P. M. Woodward, *"Structure Determination in $A_2M^{3+}M^{5+}O_6$ and $A_2M^{2+}M^{6+}O_6$ Ordered Perovskites: Octahedral Tilting and Pseudosymmetry".* Acta Cryst. B, 2006. **62**: p. 384-396.
17. M.T.Anderson, K.B.G., G.A.Taylor and K.R.Poeppelmeier, *B-cation Arrangements in Double Perovskites.* Prog. Solid Satet Chem., 1993. **22**: p. 197-233.
18. Skinner, S.J., Lagunna-Bercero, M. A., , *Advanced Inorganic Materials for Solid Oxide Fuel Cells.* . Energy Materials, ed. W. D. W. Bruce, R.I., O'Hare, D. 2011: John Wiley & Sons.

19. Jiang, S.P., *A Comparison of O_2 Reduction Reactions on Porous (La, Sr)MnO_3 and (La. Sr)(Co, Fe)O_3 Electrode. .* Solid State Ionics 2002. **146**(1-2): p. 1-22.

20. McIntosh, S.V., J. F.; Haije, W. G.; Blank, D. H. A.; Bouwmeester, and H.J.M. C, CHem. Mater., 2006. **18**: p. 2187.

21. *2.2. Cathodes on Oxygen-Ion-Conducting Electrolytes*, in *Materials for High-Temperature Fuel Cells*, Y.Y. San Ping Jiang, Editor, Wiley-VCH. p. 57.

22. Li, S., et al., *Electrical and Thermal Properties of $(Ba_{0.5}Sr_{0.5})_{1-x}Sm_xCo_{0.8}Fe_{0.2}O_{3-\delta}$ Perovskite Oxides.* Solid State Ionics, 2007. **178**(5-6): p. 417-422.

23. Li, S., et al., *Electrochemical Performance of $(Ba_{0.5}Sr_{0.5})_{0.9}Sm_{0.1}Co_{0.8}Fe_{0.2}O_{3-\delta}$ As An Intermediate Temperature Solid Oxide Fuel Cell Cathode.* Journal of Power Sources, 2007. **165**(1): p. 97-101.

24. Li, S., *Thermal, Electrical, and Eectrochemical Properties of Nd-doped $Ba_{0.5}Sr_{0.5}Co_{0.8}Fe_{0.2}O_{3-\delta}$ as a Cathode Material for SOFC.* Solid State Ionics, 2008. **178**(35-36): p. 1853-1858.

25. Li, S., et al., *Thermal, electrical, and electrochemical properties of Lanthanum-doped Ba0.5Sr0.5 Co0.8Fe0.2O3–δ.* Journal of Physics and Chemistry of Solids, 2007. **68**(9): p. 1707-1712.

26. Zhao, H., et al., *Structural and Electrochemical Studies of $Ba_{0.6}Sr_{0.4}Co_{1-y}Ti_yO_{3-\delta}$ As A New Cathode Material for IT-SOFCs.* Journal of Power Sources, 2009. **186**(2): p. 305-310.

27. K. Huang, H.Y.L., J.B. Goodenough, *Sr- and Ni-Doped $LaCoO_3$ and $LaFeO_3$ Perovskites: New Cathode Materials for Solid - Oxide Fuel Cells.* J. Electrochem. Soc, 1998. **145**: p. 3220-3227.

28. Deng, Z.Q., Claridge, J.B., Rosseinsky, M.J., , *B Cation Ordered Double Perovskite $Ba_2CoMo_{0.5}Nb_{0.5}O_{6-\delta}$ As a Potential SOFC Cathode.* Chemistry of Materials 2009. **21**: p. 5154-5162.

29. *Molybdenum Chemistry & Uses* International Molybdenum Association (IMOA) 2012; Available from: http://www.imoz.info/index.php.

30. M. Musa Saad H.-E., M.A.K.A., A. El-Taher, *First-principles Study of Structural, Electronic and Magnetic Properties of Double Perovskite Oxides Ba_2CoMO_6 (M=Mo and W).* Materials Science in Semiconductor Processing, 2015. **34**: p. 281-290.

31. Antoine Demont, R.S., Maria A. Tsiamtsouri, Simon Romani, Philip A. Chater, Hongjun Niu, Carlos Martí-Gastaldo, Zhongling Xu, Zengqiang Deng, Yohann Bréard, Michael F. Thomas, John B. Claridge, and Matthew J. Rosseinsky, *Single Sublattice Endotaxial Phase Separation Driven by Charge Frustration in a Complex Oxide.* J. Am. Chem. Soc, 2013. **27**(135): p. 10114-10123.

32. V. Tinga, Y.L., L. Noréna, R.L. Withersa, D.J. Goossensa, M. Jamesb, C. Ferrarisc, *A Structure, Conductivity and Dielectric Properties Investigation of $A_3CoNb_2O_9$ ($A=Ca^{2+}$, Sr^{2+}, Ba^{2+}) Triple Perovskites.* Journal of Solid State Chemistry, 2004. **177**(12): p. 4428-4442.

33. P. M. Mallinson, J.B.C., M. J. Rosseinsky, R. M. Ibberson, J. P. Wright, A. N. Fitch, T. Price and D. M. Iddles, *Cation Ordering/disordering kinetics in $Ba_3CoNb_2O_9$: An In Stu Study Using Synchrotron X-ray Powder Diffraction.* Applied Physics Letters 2007. **91**(22): p. 222901.

34. Kazuya Yokota, N.K., and Hidekazu Tanaka, *Magnetic Phase Dagram of the S=12 Triangular-Lattice Heisenberg Antiferromagnet $Ba_3CoNb_2O_9$.* Phys. Rev. B, 2014. **90**: p. 014403.

35. Shannon, R.D., *Revised Effective Ionic Radii and Systematic Studies of Interatomic Distances in Halides and Chalcogenides.* Acta Cryst. A 1976. **32**: p. 751-767.

36. D. Bahadur, O.M.P., *Electron Transport and Magnetic Properties of $La_{1-x}Sr_xCo_{1-y}Ti_yO_3$ (x = 0a or x = yb), .* Journal of Solid State Chemistry, 1983. **46**(2): p. 197-203.

37. S. Shafeie, J.G., S.Ya. Istomin, L. Karvonen, S.A. Chen, T.H. Chen, J.M. Chen, A. Weidenkaff, M. Karppinen, T. Sirtl, G. Svensson, *Phase Formation, Crystal Structures and Magnetic Properties of Perovskite-Type Phases in the System $La_2Co_{1+z}(Mg_xTi_{1-x})_{1-z}O_6$.* Journal of Solid State Chemistry, 2011. **184**(1): p. 177–190.

38. Segal, D., *Chemical Synthesis of Advanced Ceramic Materials*.

39. *http://www.ch.ntu.edu.tw/~sfcheng/HTML/material95/Solid_synthesis.pdf*.

40. Pecharsky, P.Y.Z.V.K., *Fundamentals of Powder Diffraction and Structural Characterisation of Materials*, 2008, Springer.

41. West, A.R., *Basic Solid State Chemistry, 2nd edition.* , 1996, John Wiley & Sons.

42. College, B. *Generation of X-rays*. Advanced Certificate in Powder Diffraction on the Web,1997-2006; Available from: http://pd.chem.ucl.ac.uk/pdnn/inst1/xrays.htm.

43. College, B. *Neutron Sources and Methods.* . Advanced Certificate in Powder Diffraction on the Web, 1997-2006; Available from: http://pd.chem.ucl.ac.uk/pdnn/inst3/neutronx.htm.

44. Pynn, R., *Neutron Scattering-A Primer.* Los Alamos Science 1990. **19**.

45. Bacon, G.E., in *Neutron Diffraction*1979, Clarendon Press: Oxford.

46. *HRPD instrument*. 2012; Available from: http://www.isis.stfc.ac.uk/instruments/hrpd/.

47. Takeda, Y., Kanno, R., Noda, M., Tomida, Y., Yamamoto, O, *Cathodic Polarisation Phenomena of Perovskite Oxide Electrodes with Stabilised Zirconia.* Journal of the Electrochemical Society, 1987. **134**(11): p. 2656-2661.

48. College, B. *Instrumentation II: Synchrotron Sources and Methods*. Advanced Certificate in Powder Diffraction on the Web, 1997-2006; Available from: http://pd.chem.ucl.ac.uk/pdnn/inst2/synindex.htm.

49. Thompson, S.P., Parker, J. E., Potter, J., Hill, T. P.,Birt, A., Cobb, T. M., Yuan, F., Tang, C. C., *Beamline I11 at Diamond: A New Instrument for High Resolution Powder Diffraction.* Review of Scientific Instruments, 2009. **80**(7): p. 075107.

50. .

51. Rietveld, H.M., *A Profile Refinement method for nuclear and magnetic structures.* Journal of Applied Crystallography, 1969. **2**: p. 65-71.

52. Coelho, A.A. *TOPAS Academic: General Profile and Structure Analysis Software for Powder Diffraction Data* 2010.

53. Schwartzenbach, D., Abrahams, S.C., Flack, H D., Prince, E., Wilson, A.J.C. *Statistical Descriptors in Crystallography, Uncertainty of Measurement.* 1996; Available from: http://ww1.iucr.org/comm/cnom/statdes/uncert.html.

54. Schwartzenbach, D., Abrahams, S.C., Flack, H D., Prince, E., and Wilson, A.J.C, *Statistical Descriptors in Crystallography.* Acta Crystallographica Section A: Foundations of Crystallography, 1995. **51**: p. 565-569.

55. Le Bail, A., Duroy, H., and Fourquet, J. L, *Ab Initio Structure Determination of $LiSbWO_6$ by X-ray Powder Diffraction.* Materials Research Bulletin, 1988. **23**: p. 447-452.

56. Pawley, G.S., *Unit-cell Refinement from Powder Diffraction Scans.* Journal of Applied Crystallography, 1981. **14**: p. 357-361.

57. D.K.Schroder, *Semiconductor Material and Device Characterisation*, 2006, Jon Wiley & Sons.

58. *Princeton Applied Research, Application Note AC-1: Basics of Electrochemical Impedance Spectroscopy.* . Available from: http://www.princetonappliedresearch.com/download.asbx?AttributeFileId=8406b254-b6d4-4341-9f48-87a04ce7ee3d.

59. *Impedance Spectroscopy: Emphasising Solid Materials and Systems*, ed. J.R. MacDonald1987: John Wiley & Sons.

60. Barsoukov, J.R.M.a.E., *History,*. Vol. 1. 2005.

61. http://www.scribner.com/software/scribner-associates-software-downloads/160-zplot-and-zview-for-windows-software-downloads.

62. Mirko Arnold, T.M.G., Julia Martynczuk and Armin Feldhoff, *Correlation of the Formation and the Decomposition Process of the BSCF Perovskite at Intermediate Temperatures.* Chem. Mater, 2008. **20**(18): p. 5851-5858.

63. De Villiers, J.P.R., Am. Miner, 1971. **56**: p. 758.

64. Kiseleva, L.A.K., A. R.; Martynov, K. V.; Ogorodova, L. P.; and J.K. Kabalov, Phys. Chem. Miner., 1994. **21**: p. 392.

65. Gushee, B.E.K., L.; Ward, R. , J. Amer. Chem. Soc, 1957. **79**(5601).

66. Taguchi, H.T., Y.; Kanamaru, F.; Shimada, M.; Koizumi, M., Acta Crystallogr., Sect. B, 1977. **33**: p. 1299.

67. H.Lu, Y.C., W.S.Yang, Solid State Ionics, 2006. **177**: p. 595.

68. S.Adler, J.L.a.B.S., Journal of the Electrochemical Society, 1996. **143**: p. 3554-3564.

69. Pingying Zeng, Z.C., Wei Zhou, Hongxia Gu, Zongping Shao, Shaomin Liu, *Re-evaluation of $Ba_{0.5}Sr_{0.5}Co_{0.8}Fe_{0.2}O_{3-\delta}$ Perovskite as Oxygen Semi-permeable Membrane.* Journal of Membrane Science, 2007. **291**(1-2): p. 148-156.

70. Bangwu Liu, Y.Z., Lidan Tang, *X-ray Photoelectron Spectroscopic Studies of $Ba_{0.5}Sr_{0.5}Co_{0.8}Fe_{0.2}O_{3-\delta}$ Cathode for Solid Oxide Fuel Cells.* International Journal of Hydrogen Energy, 2009. **34**(1): p. 435-439.

71. A. Ecijaa, , K. Vidala, A. Larrañagaa, A. Martínez-Amestia, L. Ortega-San-Martínb, M.I. Arriortuaa, , *Characterization of $Ln_{0.5}M_{0.5}FeO_{3-\delta}$ (Ln = La, Nd, Sm; M = Ba, Sr) Perovskites as SOFC Cathodes.* Solid State Ionics, 2011. **201**(1): p. 35-41.

72. Fang Wang, T.N., Keiji Yashiro, Junichiro Mizusaki, Koji Amezawa, *Effect of Nb Doping on the Chemical Stability of BSCF-based Solid Solutions.* Solid State Ionics, 2014. **262**: p. 719-723.

73. S.M. Fang, C.-Y.Y., H.J.M. Bouwmeester, *Performance and Stability of Niobium-Substituted $Ba_{0.5}Sr_{0.5}Co_{0.8}Fe_{0.2}O_{3-\delta}$ Membranes.* Solid State ionics, 2011. **195**: p. 1-6.

74. Hailei Zhao, D.T., Xiuhua Zhang, Cuijuan Zhang, Xue Li, *Structural and Electrochemical Studies of $Ba_{0.6}Sr_{0.4}Co_{1-y}Ti_yO_{3-\delta}$ as A New Cathode Material for IT-SOFCs.* Journal of Power Sources, 2009. **186**: p. 305-310.

75. Zhi-Bin Yang, M.-F.H., Peiyu Zhu, Fei Zhao, Fanglin Chen, *$Ba_{1-x}Co_{0.9-y}Fe_yNb_{0.1}O_{3-\delta}$ (x = 0–0.15, y = 0–0.9) as Cathode Materials for Solid Oxide Fuel Cells.* International Journal of Hydrogen Energy, 2011. **36**: p. 9162-9168.

76. Mirko Arnold, Thorsten M. Gesing, Julia Martynczuk, and Armin Feldhoff, 2008.

77. Zhibin Yang, F.C., *Assessment of $Ba_{1-x}Co_{0.9-y}Fe_yNb_{0.1}O_{3-\delta}$ for High Temperature Electrochemical Devices.* Ceramic Engineering and Science Proceeedings 2013. **34**(4).

78. https://en.wikipedia.org/wiki/Binding_energy.

79. Yang Li, F.L., Ning Chen, Zhen-jia Hao, Kuo-chih Chou, *Structural Predictions Based on the Compositions of Cathodic Materials by First-Principles Calculations.* International Journal of Minerals, Metallurgy, and Materials, 2015. **22**(5): p. 524-529.

80. Steven McIntosh, J.F.V., Wim G. Haije, Dave H.A. Blank, Henny J.M. Bouwmeester, *Structure and Oxygen Stoichiometry of $SrCo_{0.8}Fe_{0.2}O_{3-\delta}$ and $Ba_{0.5}Sr_{0.5}Co_{0.8}Fe_{0.2}O_{3-\delta}$.* Solid State Ionics, 2006. **177**: p. 1737-1742.

81. Bouwmeester, S.M.., *Oxygen Stoichiometry and Chemical Expansion of $Ba_{0.5}Sr_{0.5}Co_{0.8}Fe_{0.2}O_{3-\delta}$ Measured by in Situ Neutron Diffraction.* Chem. Mater, 2006. **18**(8): p. 2178-2193.

82. Zongping Shao, S.M.H., *A High-Performance Cathode for the Next Generation of Solid-Oxide Fuel Cells.* Nature, 2004. **431**: p. 170-173.

83. Y. H. Lim, J.L., J. S. Yoon, C. E. Kim, and H. J. Hwang, *Electrochemical performance of $Ba_{0.5}Sr_{0.5}Co_xFe_{1-x}O_{3-\delta}$ (x=0.2–0.8) Cathode on a ScSZ Eectrolyte for Intermediate Temperature SOFCs.* Journal of Power Sources, 2007. **171**: p. 79-85.

84. Ming Li, H.G., John Druce, Helena Téllez, Tatsumi Ishihara, John A. Kilner, Hongjun Niu, Wen Xu, Michael J. Pitcher, John B. Claridge, and Matthew J.

Rosseinsky, *High Oxygen Ion and Electronic Conductivity in a Bi-containing Perovskite Oxide.* Advanced Materials.in progress.